

Geological Society of America Bulletin

Tectonic history of the Altyn Tagh fault system in northern Tibet inferred from Cenozoic sedimentation

A. Yin, P.E. Rumelhart, R. Butler, E. Cowgill, T.M. Harrison, D.A. Foster, R.V. Ingersoll, Zhang Qing, Zhou Xian-Qiang, Wang Xiao-Feng, A. Hanson and A. Raza

Geological Society of America Bulletin 2002;114, no. 10;1257-1295
doi: 10.1130/0016-7606(2002)114<1257:THOTAT>2.0.CO;2

Email alerting services

click www.gsapubs.org/cgi/alerts to receive free e-mail alerts when new articles cite this article

Subscribe

click www.gsapubs.org/subscriptions/ to subscribe to Geological Society of America Bulletin

Permission request

click <http://www.geosociety.org/pubs/copyrt.htm#gsa> to contact GSA

Copyright not claimed on content prepared wholly by U.S. government employees within scope of their employment. Individual scientists are hereby granted permission, without fees or further requests to GSA, to use a single figure, a single table, and/or a brief paragraph of text in subsequent works and to make unlimited copies of items in GSA's journals for noncommercial use in classrooms to further education and science. This file may not be posted to any Web site, but authors may post the abstracts only of their articles on their own or their organization's Web site providing the posting includes a reference to the article's full citation. GSA provides this and other forums for the presentation of diverse opinions and positions by scientists worldwide, regardless of their race, citizenship, gender, religion, or political viewpoint. Opinions presented in this publication do not reflect official positions of the Society.

Notes



Tectonic history of the Altyn Tagh fault system in northern Tibet inferred from Cenozoic sedimentation

A. Yin*

Department of Earth and Space Sciences and Institute of Geophysics and Planetary Physics, University of California, Los Angeles, California 90095, USA

P.E. Rumelhart†

Department of Earth and Space Sciences, University of California, Los Angeles, California 90095, USA

R. Butler

Department of Geosciences, University of Arizona, Tucson, Arizona 85721, USA

E. Cowgill§

Department of Earth and Space Sciences, University of California, Los Angeles, California 90095, USA

T.M. Harrison

Department of Earth and Space Sciences and Institute of Geophysics and Planetary Physics, University of California, Los Angeles, California 90095, USA

D.A. Foster

Department of Geological Sciences, University of Florida, Gainesville, Florida 32611, USA

R.V. Ingersoll

Department of Earth and Space Sciences, University of California, Los Angeles, California 90095, USA

Zhang Qing#

Zhou Xian-Qiang

Wang Xiao-Feng

Institute of Geomechanics, Chinese Academy of Geological Sciences, Beijing 100081, People's Republic of China

A. Hanson**

Department of Geological and Environmental Sciences, Stanford University, Stanford, California 94305, USA

A. Raza

School of Earth Sciences, University of Melbourne, Melbourne, Victoria, Australia

ABSTRACT

The active left-slip Altyn Tagh fault defines the northern edge of the Tibetan plateau. To determine its deformation history we conducted integrated research on Ce-

nozoic stratigraphic sections in the southern part of the Tarim Basin. Fission-track ages of detrital apatites, existing biostratigraphic data, and magnetostratigraphic analysis were used to establish chronostratigraphy, whereas composition of sandstone and coarse clastic sedimentary rocks was used to determine the unroofing history of the source region. Much of the detrital grains in our measured sections can be correlated with uplifted sides of major thrusts or transpressional faults, implying a temporal link between sedimentation and deformation. The results of our studies, together with existing stratigraphic data from the Qaidam Basin and the Hexi Corridor, suggest that crustal thickening in northern

Tibet began prior to 46 Ma for the western Kunlun Shan thrust belt, at ca. 49 Ma for the Qimen Tagh and North Qaidam thrust systems bounding the north and south margins of the Qaidam Basin, and prior to ca. 33 Ma for the Nan Shan thrust belt. These ages suggest that deformation front reached northern Tibet only $\sim 10 \pm 5$ m.y. after the initial collision of India with Asia at 65–55 Ma. Because the aforementioned thrust systems are either termination structures or branching faults of the Altyn Tagh left-slip system, the Altyn Tagh fault must have been active since ca. 49 Ma. The Altyn Tagh Range between the Tarim Basin and the Altyn Tagh fault has been a long-lived topographic high since at least the early Ol-

*E-mail: yin@ess.ucla.edu.

†Present address: Exxon Exploration Company, P.O. Box 4778, Houston, Texas 77210, USA.

§Present address: Division of Geological and Planetary Sciences, California Institute of Technology, Pasadena, California 91125, USA.

#Present address: Department of Geology and Geophysics, University of Minnesota, Minneapolis, Minnesota 55455, USA.

**Present address: Department of Geosciences, University of Nevada, Las Vegas, Nevada 89154, USA.

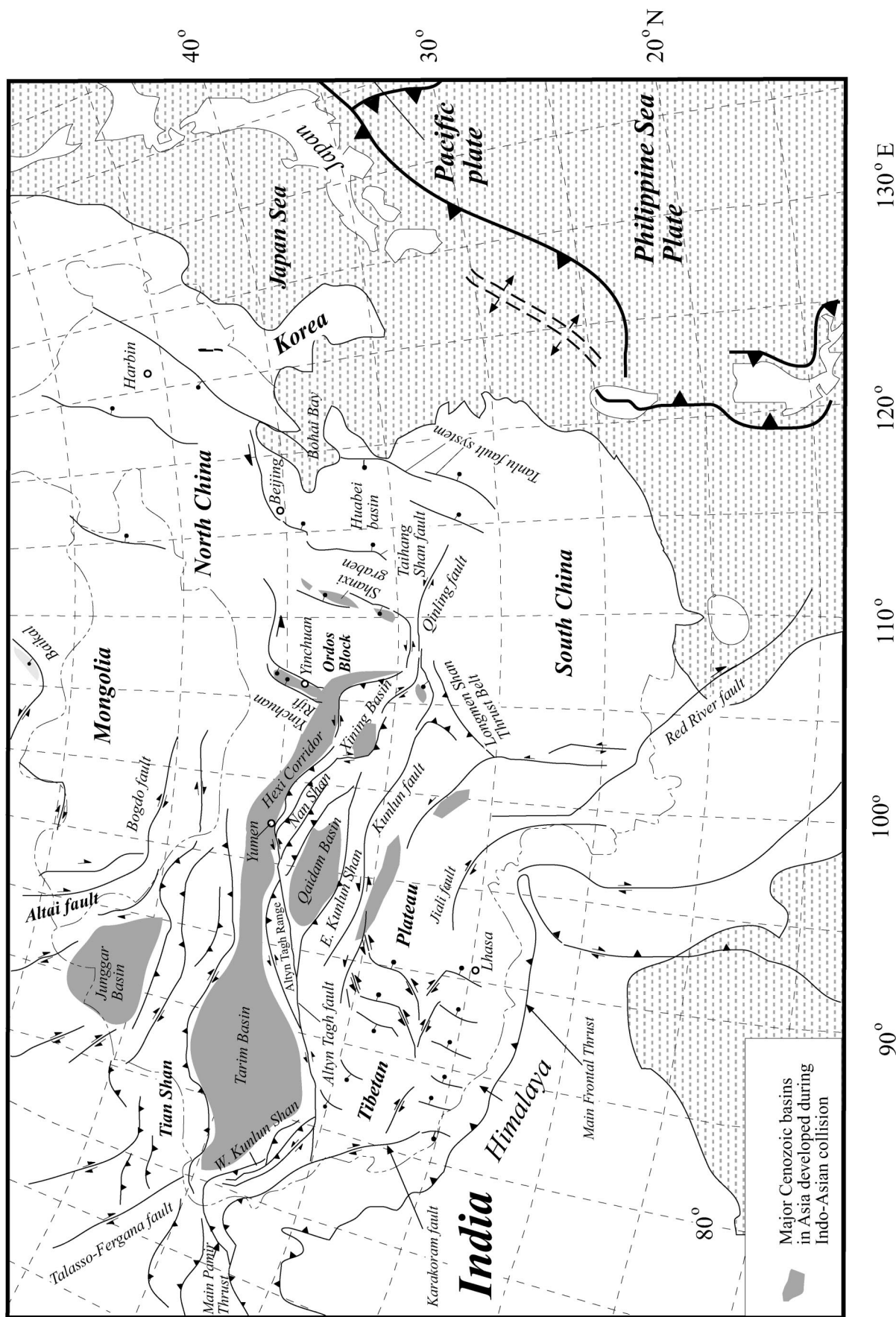


Figure 1. Cenozoic tectonic map of the Indo-Asian collision zone, modified after Yin et al. (1998) and Yin (2000). The left-slip Altn Tagh fault defines the northern edge of the Tibetan plateau and terminates at the Nan Shan thrust belt in the northeast and the western Kunlun thrust belt in the southwest. The Tarim Basin lies between the Tian Shan in the north and the Tibetan plateau in the south and receives sediments from both regions. The Qaidam Basin south of the Altn Tagh fault is bounded by the Altn Tagh Range, the eastern Kunlun Shan, and the Nan Shan. The fault east of Himalaya is unnamed.

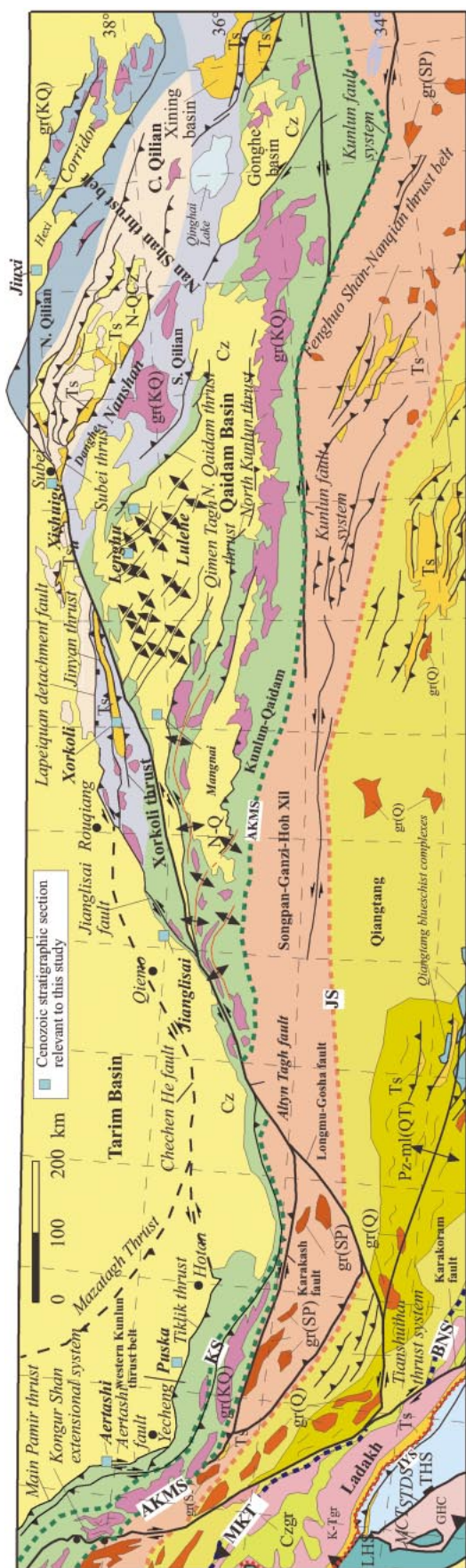


Figure 2. Simplified tectonic map of northern Tibet showing major tectonic terranes, sutures, and faults (after Yin and Harrison, 2000). Cenozoic stratigraphic sections (locations shown by turquoise blue squares) were measured by this study at Aertashi, Puskha, Jianguisai, and Xishuigou in the southern Tarim Basin. Other relevant stratigraphic sections are Mangnai, Lenghu, Lulehe, Xorkoli, and Jiuxi (Hexi Corridor). Map symbols: N-Q—Neogene–Quaternary sediments, Ts—Tertiary sedimentary rocks, THS—Tethyan Himalayan sequences (Proterozoic to Upper Cretaceous passive–continental–margin strata of northern India), GHC—Greater Himalayan Crystalline Complex, LHS—Lesser Himalayan metasedimentary series. Major plutonic rocks: Czgr—Cenozoic granites, K-Tgr—plutonic rocks belonging to the Gangdese batholith, Ladakh batholith, and Kohistan arc, gr(Q)—plutonic rocks in the Qiangtang terrane (mostly Jurassic–Cretaceous), gr(SP)—plutonic rocks in the Songpan–Ganzi–Hoh Xil terrane (mostly Late Triassic), gr(KQ)—Ordovician–Silurian and Permian–Triassic plutonic rocks in the Kunlun and Qilian terranes. Major sutures: IYS—Indus–Yalu suture, BNS—Bangong–Nujiang suture, JS—Jinsha suture, AKMS—Ayimaqin–Kunlun–Mutztagh suture, KS—Kudi suture, MCT—Main Central thrust, MKT—Main Karakoram thrust, STDS—South Tibet detachment system.

igocene or possibly late Eocene. This range has shed sediments into both the Tarim and Qaidam Basins while being offset by the Altyr Tagh fault. Its continuous motion has made the range act as a sliding door, which eventually closed the outlets of westward-flowing drainages in the Qaidam Basin. This process has caused large amounts of Oligocene–Miocene sediments to be trapped in the Qaidam Basin. The estimated total slip of 470 ± 70 km and the initiation age of 49 Ma yield an average slip rate along the Altyr Tagh fault of 9 ± 2 mm/yr, remarkably similar to the rates determined by GPS (Global Positioning System) surveys. This result implies that geologic deformation rates are steady state over millions of years during continental collision.

Keywords: Tibetan plateau, foreland basin, Tarim basin, thrust faults, strike-slip faults.

INTRODUCTION

When the Tibetan plateau was constructed remains a subject of debate. Although many consider it to have formed in the Cenozoic during Indo-Asian collision (e.g., Dewey and Burke, 1973; Allègre et al., 1984; England and Houseman, 1986; Dewey et al., 1988, 1989; Le Pichon et al., 1992), significant crustal shortening in the Mesozoic may have also contributed to the current elevation of the plateau (Murphy et al., 1997; Yin and Harrison, 2000; Hildebrand et al., 2001). The pre-Cenozoic topography may have in turn controlled subsequent Cenozoic deformation in Asia (Kong et al., 1997). With regard to the Cenozoic history, it remains unclear whether the plateau was uplifted either progressively northward (e.g., Tapponnier et al., 1990; Burchfiel and Royden, 1991; Meyer et al., 1998) or synchronously as a whole (e.g., Harrison et al., 1992; Molnar et al., 1993). This uncertainty has prevented us from understanding its dynamic cause (Zhao and Morgan, 1987; England and Houseman, 1989; Willett and Beaumont, 1994; F. Shen et al., 2001) and the possible link with climate change (e.g., Harrison et al., 1992, 1998; Molnar et al., 1993).

The poor constraints on the timing of Tibetan uplift may be attributed to our incomplete understanding of Cenozoic deformation history of northern Tibet. For example, Burchfiel et al. (1989) and Meyer et al. (1998) concluded that the Nan Shan thrust belt in northern Tibet has developed within the past few million years, whereas George et al. (2001) suggested that the thrust belt was already ac-

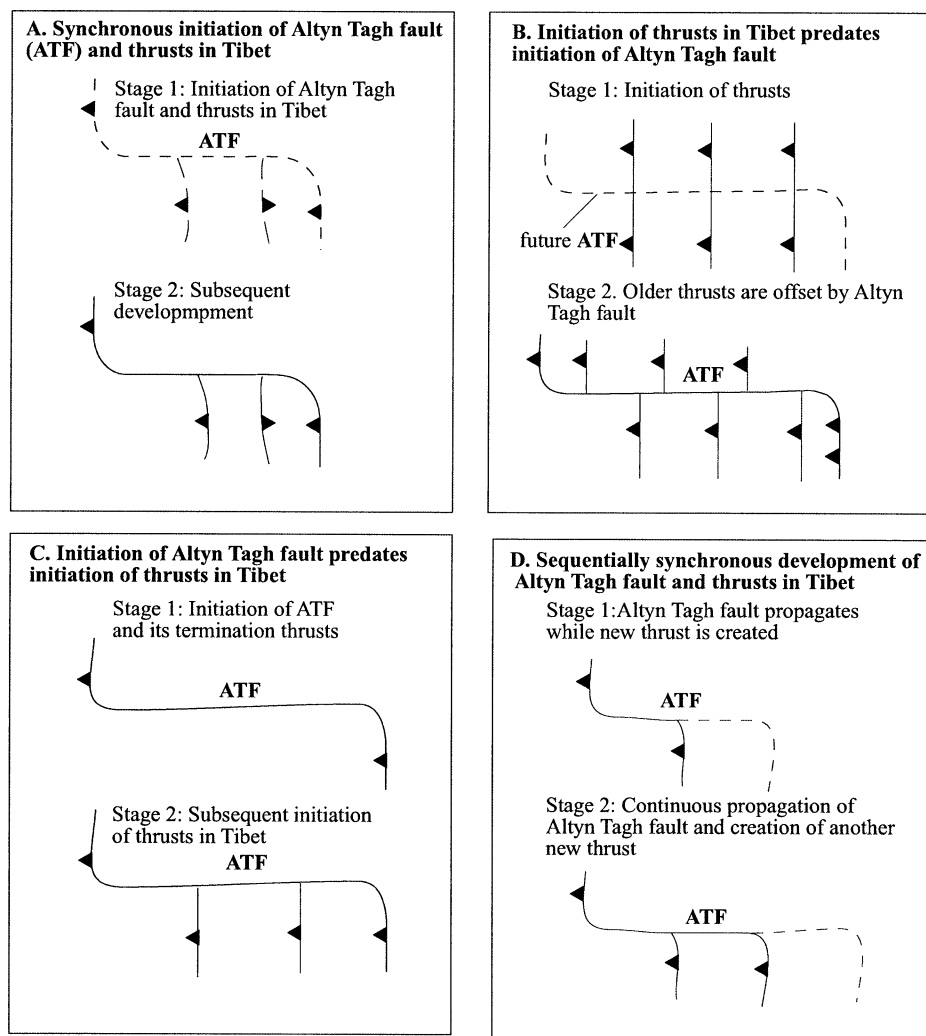


Figure 3. Geometric and temporal relationships between thrusting in Tibet and movement on the Altyn Tagh fault. (A) Coeval initiation of strike-slip and thrust faulting. (B) Thrusting initiated prior to strike-slip faulting. (C) Strike-slip faulting initiated prior to thrusting. (D) Propagation of strike-slip faulting associated with creation of new thrusts. The geologic relationship across the Altyn Tagh fault is most consistent with the kinematic history of D (see text for details).

tive at ca. 20 Ma. Because the southern Tarim Basin currently receives sediments from the Tibetan plateau, it is natural to use the basin's Cenozoic strata as a proxy to decipher the uplift history of northern Tibet. Also, because the Altyn Tagh fault system is the first-order structure defining the northern margin of the Tibetan plateau, it is possible that sedimentation in the southern Tarim Basin has been tied to the development of this large-scale (>1600 km long) intracontinental fault system. In this paper, we present evidence that links sedimentation in the southern Tarim Basin with deformation along the Altyn Tagh fault system during the Cenozoic growth of the Tibetan plateau. By combining this evidence with ex-

isting data from the Qaidam Basin and the Hexi Corridor, we are able to present a self-consistent tectonic model for the temporal evolution of the Altyn Tagh fault system and the uplift history of the northern Tibetan plateau.

REGIONAL GEOLOGIC FRAMEWORK

Altyn Tagh Fault System

The left-slip Altyn Tagh fault system is a major tectonic element in the Cenozoic Indo-Asian collision zone (Molnar and Tapponnier, 1975) (Fig. 1). Currently, the fault may accommodate as much as one-third of the over-

all convergence between India and Siberia (Avouac and Tapponnier, 1993). This fault has been regarded as either a crustal-scale transfer fault linking thrust belts (Burchfiel et al., 1989) or a lithospheric-scale strike-slip fault assisting eastward extrusion of Tibet (Wittlinger et al., 1998). Although most workers consider that the Altyn Tagh fault ends in the western Kunlun Shan and the Nan Shan (Burchfiel et al., 1989; Yin and Harrison, 2000), some workers have extrapolated the fault to northeast Asia (Jolivet et al., 1994; Worrall et al., 1996; Yue and Liou, 1999). At its southwest end, the Altyn Tagh fault splits into two branches (Fig. 2). The northern strand links with the left-slip Karakash fault and the western Kunlun thrust belt, whereas the southern strand links with the Longmu-Gozha fault that intersects with the right-slip Karakoram fault and bounds the south-directed Cenozoic Tianshuihai thrust system (Fig. 2; Cowgill, 2001). The left-slip Jianglisai fault (also known as the North Altyn Tagh fault) along the northern edge of the Altyn Tagh Range and the Chechen He fault in the southern Tarim Basin are parts of the Altyn Tagh fault system (Jia et al., 1991; Cowgill, 2001) (Figs. 1 and 2). In the southwest, the Chechen He fault links with the Tiklik thrust in the western Kunlun Shan and the Mazatagh thrust in the southwestern Tarim Basin (Kang, 1996). In the northeast, the Chechen He fault terminates near Rouqiang (Jia et al., 1991; Kang, 1996), where it may have merged with the Tertiary Jinyan and Xorkoli thrusts in the eastern Altyn Tagh Range (Yin et al., 1999) (Fig. 2).

The active Altyn Tagh fault has produced major earthquakes with magnitudes as large as $M_w = 7.8$ in the Holocene (Washburn et al., 2001). Its Quaternary slip rates have constituted an important constraint for deriving the velocity field of east Asia (Avouac and Tapponnier, 1993; Peltzer and Saucier, 1996; Kong and Bird, 1996). GPS (Global Positioning System) surveys suggest the Altyn Tagh fault to have moved at a rate of ~ 9 mm/yr in the past few years (Bendick et al., 2000; Chen et al., 2000; Z.K. Shen et al., 2001). Although a minimum Quaternary slip rate of ~ 4 mm/yr was determined along the eastern end of the fault (Meyer et al., 1996, 1998), a much higher Holocene slip rate of ~ 20 – 30 mm/yr was estimated along its central segment (Peltzer et al., 1989; Meriaux et al., 2000). These high rates were questioned for their incompatibility with the overall strain pattern in Asia (England and Molnar, 1998; Holt et al., 2000).

Tapponnier and Molnar (1977) first postulated displacement of several hundred kilo-

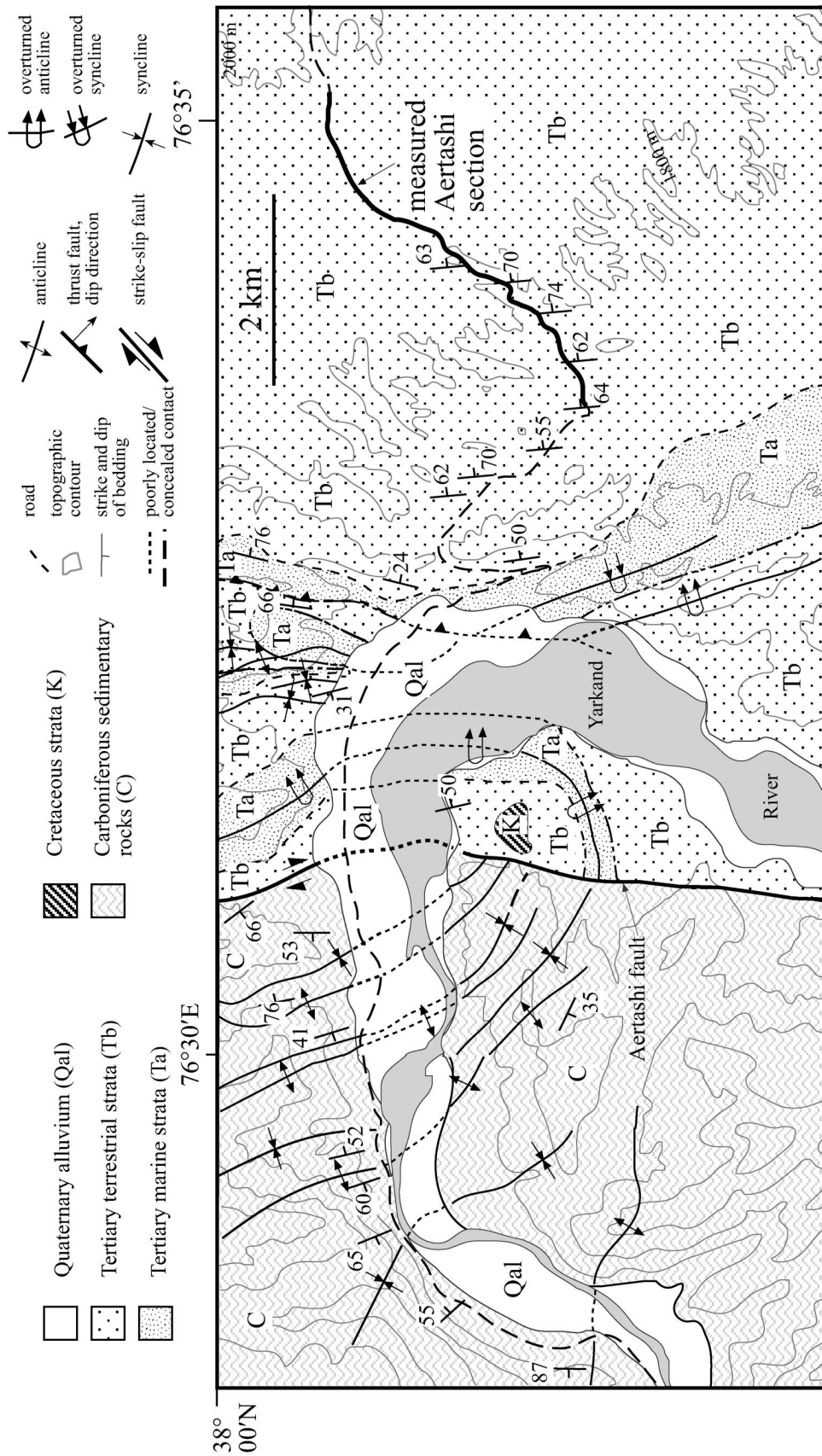


Figure 5. Simplified geologic map of the Aertashi area and location of the measured stratigraphic section. See map legend for explanation.

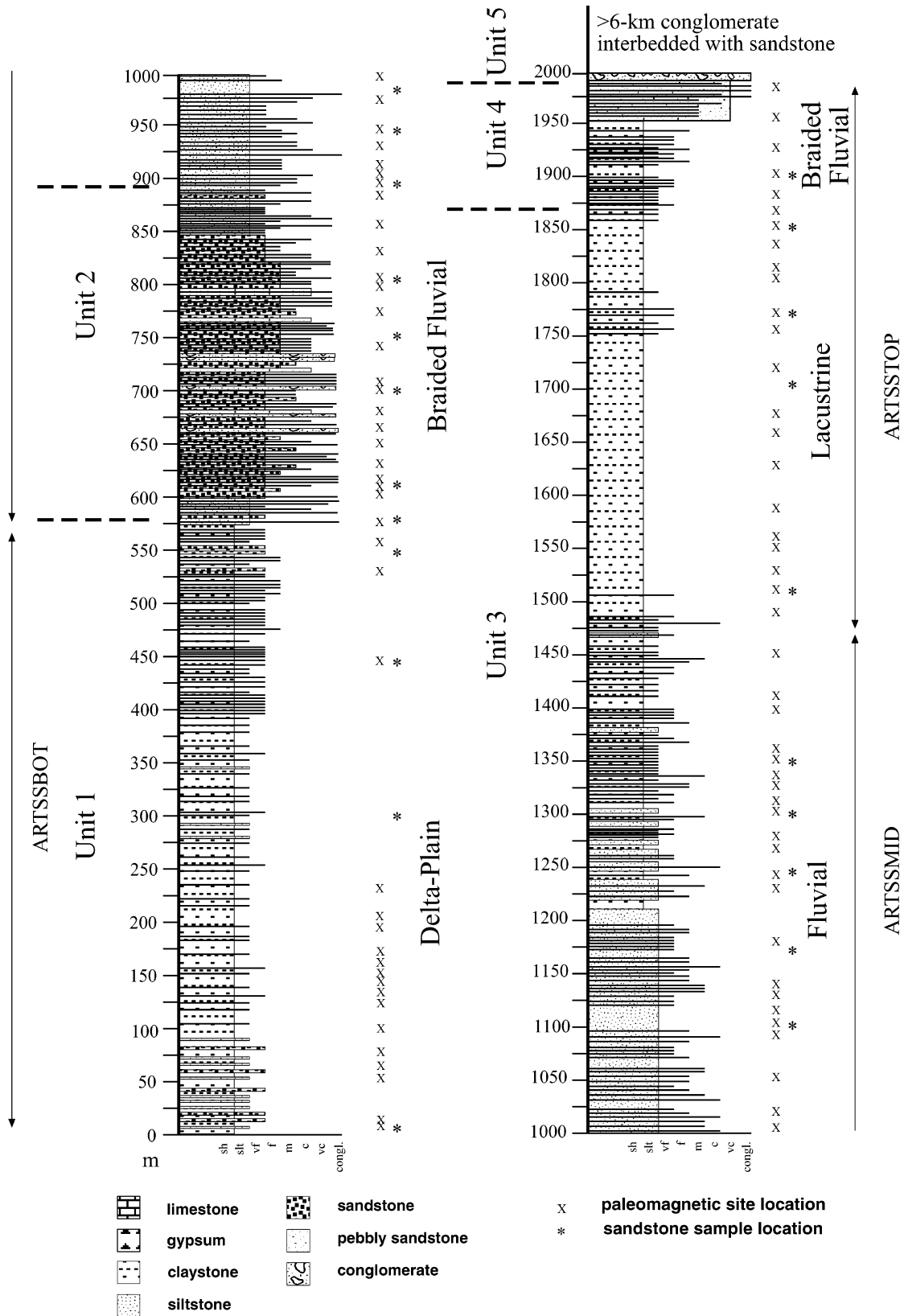


Figure 6. Measured lithostratigraphic section at Aertashi. Symbol “x” represents location of paleomagnetic samples, whereas “*” represents location of sandstone samples. The stratigraphic locations of three composite fission-track samples ARTSSSTOP, ARTSSMID, and ARTSSBOT are also shown. See legend and text for detailed description.

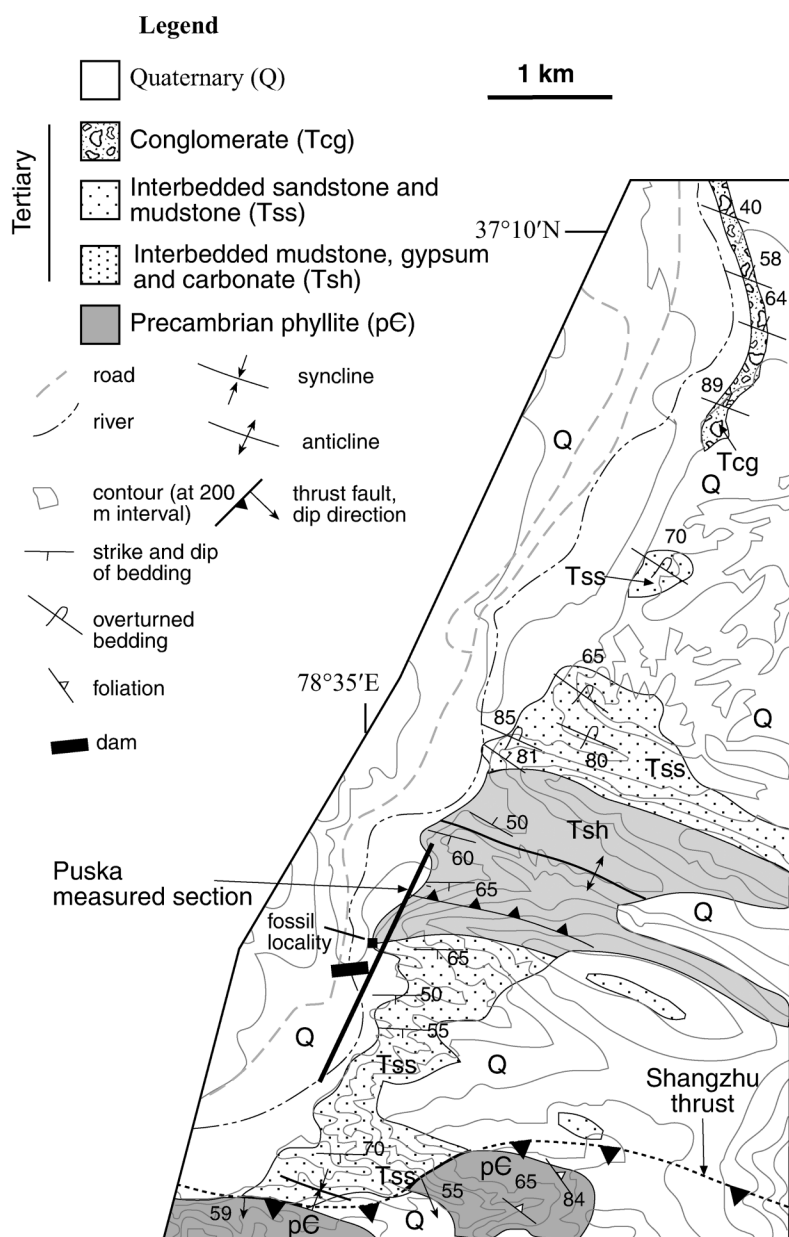


Figure 7. Simplified geologic map of the Puska section and location of the measured stratigraphic section. See map legend for explanation.

meters along the 1600-km-long Altyn Tagh fault during the Indo-Asian collision. However, other workers concluded the fault to have slipped only 70–120 km (Wang, 1997). In an early study, Pan (1984) suggested that the western Altyn Tagh fault has offset pre-Tertiary lithologic units for ~300–500 km left laterally (also see Peltzer and Tapponnier, 1988; Jiang et al., 1992; Cowgill, 2001). Along the central and eastern Altyn Tagh fault, correlation of sutures, Jurassic strata, and plutons has yielded highly inconsistent offset estimates, ranging from 400 km to 1200 km (CSBS, 1992; Sobel and Arnaud, 1999; Ritts and Biffi, 2000;

Sobel et al., 2001; Yue et al., 2001; Yang et al., 2001). Contrary to the general interpretation that the Altyn Tagh fault has been a left-slip system, Zhou and Graham (1996) inferred a phase of right-slip motion on the fault.

Wang (1997) concluded that movement on the easternmost Altyn Tagh fault was initiated after the middle Miocene (ca. 16 Ma). Meyer et al. (1998) and Métivier et al. (1998) inferred movement on the fault to have been initiated in the Miocene. Hanson (1999) showed that the western Qaidam Basin received sediments from the Altyn Tagh Range at least since Oligocene time, implying that the Altyn Tagh fault was

already in existence at this time. Li et al. (2000) suggested that the Altyn Tagh fault was active in the Triassic, whereas Delville et al. (2001) found left-slip ductile shear zones locally present along the Altyn Tagh fault to have developed between 160 and 140 Ma.

Relationship Between Altyn Tagh Fault and Cenozoic Thrusts in Tibet and Tarim Basin

The active Altyn Tagh fault terminates at the Nan Shan and western Kunlun thrust belts (Burchfiel et al., 1989) and is linked with several active thrusts bounding the Qaidam Basin (Fig. 2). This relationship suggests that motion on the Altyn Tagh fault is related to development of thrusts in northern Tibet (e.g., Yin and Nie, 1996). However, whether movements on the Altyn Tagh fault and the thrusts were initiated coevally has not been investigated. There are four possible temporal relationships. (1) Movement on the Altyn Tagh fault was initiated coevally with movement on the thrusts (Fig. 3A). In this case, thrusts do not correlate across the Altyn Tagh fault. (2) Movement on the Altyn Tagh fault postdates movement on the thrusts (Fig. 3B), which requires offset thrusts to be correlated across the Altyn Tagh fault. (3) Movement on the Altyn Tagh fault started prior to initiation of movement on thrusts (Fig. 3C). In this case, thrusts would have branched off from the main strike-slip fault at a later time. (4) Lengthening of the Altyn Tagh fault has been associated with progressive thrust formation (Fig. 3D). The four possible models can be tested because they predict distinctive geometric and age relationships between thrusts and the Altyn Tagh fault. The inactive Xorkoli and Jinyan thrusts in the eastern Altyn Tagh Range are truncated by the currently active eastern Altyn Tagh fault (Fig. 2; Yin and Harrison, 2000), which requires movement on the Altyn Tagh to have been initiated after the thrusts. However, this relationship is not valid for thrusts in the Qaidam Basin where no corresponding offset thrusts (i.e., the North Qaidam and Qimen Tagh thrusts) can be found across the Altyn Tagh fault. This latter relationship implies that movement on the Altyn Tagh fault was initiated synchronously with movement on thrusts bounding the Qaidam Basin. Such a synchronous relationship also requires the western Kunlun Shan thrust belt to be the western termination structure of the Altyn Tagh fault.

Cenozoic Basins Along the Altyn Tagh Fault System

Southern Tarim Basin

The Cenozoic southwest Tarim Basin consists of a marine sequence below (Aertashi,

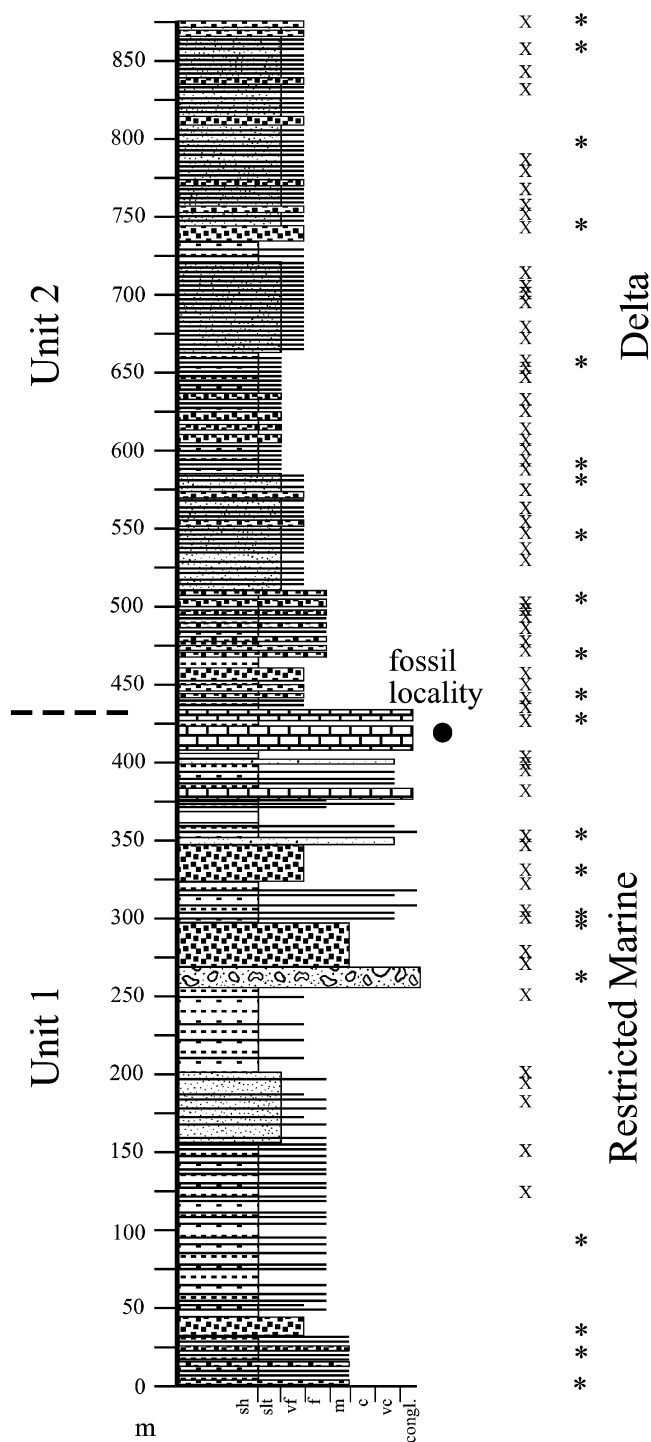


Figure 8. Lithostratigraphic section at Puska. All symbols are the same as those in Figure 6.

Qimugen, Kalatar, Wulagen, and Bashibulake Formations) and a continental sequence above (Wuqia Group and Artushi and Xiyu Formations) (Fig. 4). The two sequences are conformable in Aertashi (Yang et al., 1995; Lan and Wei, 1995) but unconformable elsewhere (e.g., Sobel, 1995). Between Qimogen and Ruoqiang in the south-central Tarim Basin, an elongate Ce-

nozoic basin (Qimogen depression of Li et al., 1996) lies between the Chechen He and Jianglisai faults (Li et al., 1996). In the southeastern Tarim Basin, Cenozoic strata crop out at the western end of the Nan Shan thrust belt (Xinjiang BGMR, 1993) (Figs. 2 and 4).

Huang and Chen (1981) and Li (1996) argued that the Tibetan plateau was uplifted in

the Pliocene as indicated by thick gravel deposition in the southern Tarim Basin. A recent magnetostratigraphic study by Zheng et al. (2000) in the southwestern Tarim Basin concurred with this opinion. Although the magnetostratigraphic data of Zheng et al. (2000) are of high quality, the lack of absolute age control in their section makes it difficult to evaluate the uniqueness of their proposed age correlation. In addition to the poor age constraints for the proposed Pliocene uplift for Tibet, it has also been noted that coarse-grained sedimentation at this period is a global phenomenon possibly related to the climatic condition instead of regional tectonics (Liu et al., 1996; Zhang et al., 2001).

Nan Shan

The Nan Shan and Hexi Corridor consist of scattered Tertiary continental deposits formally named as the Huoshaoguo, Baiyanghe and Shulehe Formations (Fig. 4) (Xu et al., 1989; Wang, 1997). Fossil contents and magnetostratigraphic analysis have led geologists to assign an Oligocene age to the Huoshaoguo Formation, a Miocene age to the Baiyanghe Formation, and a Pliocene age to the Shulehe Formation (Huang et al., 1993; Yang et al., 1994).

Altyr Tagh Range

The best-preserved Tertiary basin is located in the eastern Altyr Tagh Range between the Jinyan and Xorkoli thrusts (Fig. 2). It consists of a sequence of fluvial-lacustrine strata dated by fossils to be late Eocene and early Oligocene (Xinjiang BGMR, 1981) (Fig. 4). Both the basin and basin-bounding thrusts are truncated by the Altyr Tagh fault (Fig. 2).

Qaidam Basin

The oldest Tertiary unit in the Qaidam Basin is the middle to upper Eocene Lulehe Formation composed of conglomerate, sandstone, and mudstone (Fig. 4). This unit unconformably overlies a variety of lithologic units including Paleozoic granites, Proterozoic-Paleozoic metamorphic rocks, and Jurassic and Cretaceous sedimentary strata. This relationship has been taken as evidence for the initiation of Cenozoic sedimentary filling of the Qaidam Basin (Huo, 1990; Zhang, 1997). The Oligocene Lower Gancaigou Formation directly above the Lulehe Formation is dominated by fluvial and lacustrine sedimentary deposits that cover the entire Qaidam Basin. Because it receives sediments from all sides at this time, the basin is interpreted to have been internally drained since the beginning of the Oligocene (Huo, 1990).

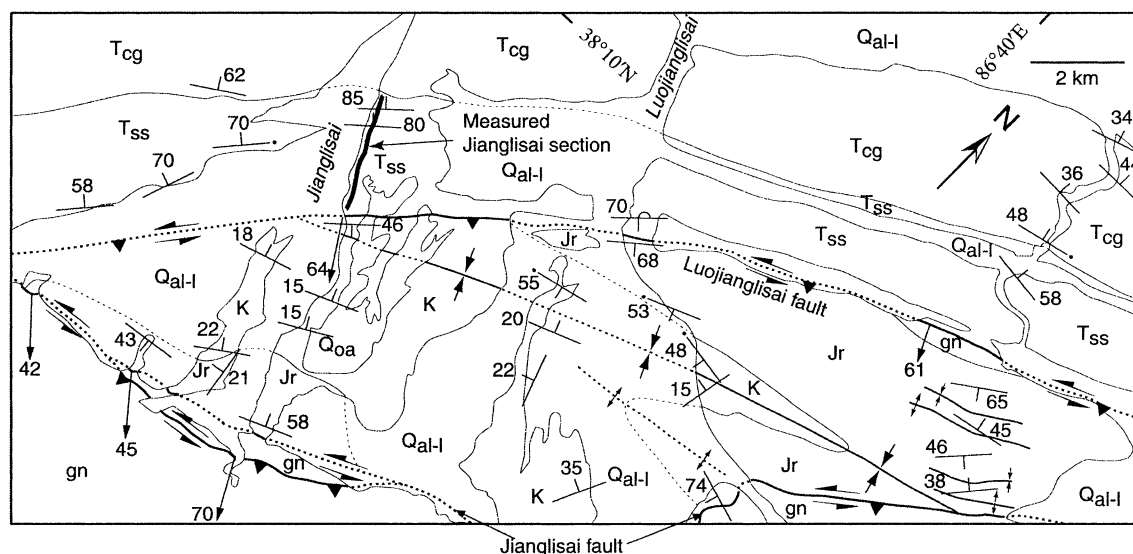


Figure 9. Simplified geologic map of the Jianglisai area and location of the measured stratigraphic section. Map symbols: Gn—Precambrian (?) gneisses; Jr—Jurassic sedimentary rocks; K—Cretaceous red beds; Tss—Tertiary sandstone unit; Tcg—Tertiary conglomerate unit; and Qal-I—Quaternary alluvial deposits. Stratigraphic section was measured within the Tss unit.

LITHOSTRATIGRAPHY IN SOUTHERN TARIM BASIN

Aertashi Section

This section is located along the Yarkand River (Figs. 2 and 5) where Cenozoic strata >9 km thick were deposited (Ye and Huang, 1990). Sobel (1999) studied the Jurassic to lower Tertiary strata in the same area. Our section begins ~200 m above the upper Eocene–lowermost Oligocene Bashibulake Formation and corresponds to the Oligocene–Miocene Kezilouyi, Anjuan, and Pakabulake Formations of the Wuqia Group and the lowest part of the Artushi Formation (Fig. 4).

The major structure in the area is the Aertashi fault, which is a segment of the Main Pamir thrust system (Fig. 1). This contact was considered to be depositional (Xinjiang BGMR, 1993; Liu, 1988) or a thrust (Sobel and Dumitru, 1997), but our field observations indicate it to be a right-slip fault. We divide the section into five units (Fig. 6). The basal part of unit 1 (0–80 m) consists of thin and laterally continuous sandstone, siltstone and claystone. The middle member of unit 1 (80–250 m) is dominated by claystone and siltstone, whereas its upper member (250–550 m) coarsens upward from claystone to medium-grained sandstone. Calcretes are locally developed within the upper member of unit 1. Unit 2 (~350 m) is medium-grained to pebbly sandstone interbedded with irregular stringers of cobble conglomerate. Unit 3 (~975 m) is

a fining-upward sequence composed of channelized medium- to coarse-grained sandstone interbedded with siltstone and claystone. Unit 4 (~120 m) is composed of medium- to coarse-grained sandstone interbedded with siltstone beds. A >6-km-thick, northward-dipping, cobble to boulder conglomerate unit lies above our measured section.

Determining whether the measured section was deposited continuously without significant hiatus is important because the section is used to establish magnetostratigraphic ages. In this regard the calcretes in the upper member of unit 1 deserve special attention. Calcretes are typically developed under arid to subhumid regions (Khadkikar et al., 2000). They may form during pedogenic processes typically associated with wedge-shaped vertical fissuring and fracturing due to soil movement and dewatering (Khadkikar et al., 1998). The time scale for pedogenic calcrete development is highly uncertain, but generally thought to be on the order of 20–30 k.y. (Milnes, 1992; Khadkikar et al., 2000). If calcretes observed in our measured section were products of pedogenic processes, it implies that tens or perhaps hundreds of thousands of years may be missing from the upper member of unit 1. Alternatively, calcretes can also form by groundwater circulation (Spötl and Wright, 1992) or by ponded water in channels (Arakel, 1986; Khadkikar et al., 1998). We favor these two alternative processes because we observe no vertical fissures filled by carbonates in the field.

Puska Section

This section is characterized by a sequence of fine-grained deposits (Fig. 7). Our measured section starts from the core of an anticline and ends near the Shangzhu thrust (Fig. 8), which is part of the Tiklik thrust system (Cowgill, 2001). We divide the Puska section into two units. Unit 1 (425 m) consists of medium-grained sandstone and a 15–20-m-thick fossiliferous carbonate zone. Unit 2 (450 m) consists of interbedded shale and medium- to fine-grained sandstone and laminated siltstone.

Jianglisai Section

The Jianglisai section north of the left-slip Jianglisai fault of Cowgill et al. (2000) consists of six units (Figs. 9 and 10). Unit 1 (~125 m) consists of sandstone interbedded with claystone and siltstone. Unit 2 (~200 m) is predominantly sandstone. Unit 3 (~125 m) and Unit 4 are composed of cobble conglomerate and coarse-grained sandstone interbedded with claystone. Unit 5 (~200 m) is mainly pebble-cobble conglomerate. Unit 6 (~350 m) consists primarily of matrix- and clast-supported conglomerate. The deposition of the coarsening-upward section at Jianglisai with northward paleocurrent direction may have been related to uplift of the Altyn Tagh Range. Because the base of the section is not exposed, the starting age of the Cenozoic sedimentation only provides the upper-age bound for the uplift of the Altyn Tagh Range.

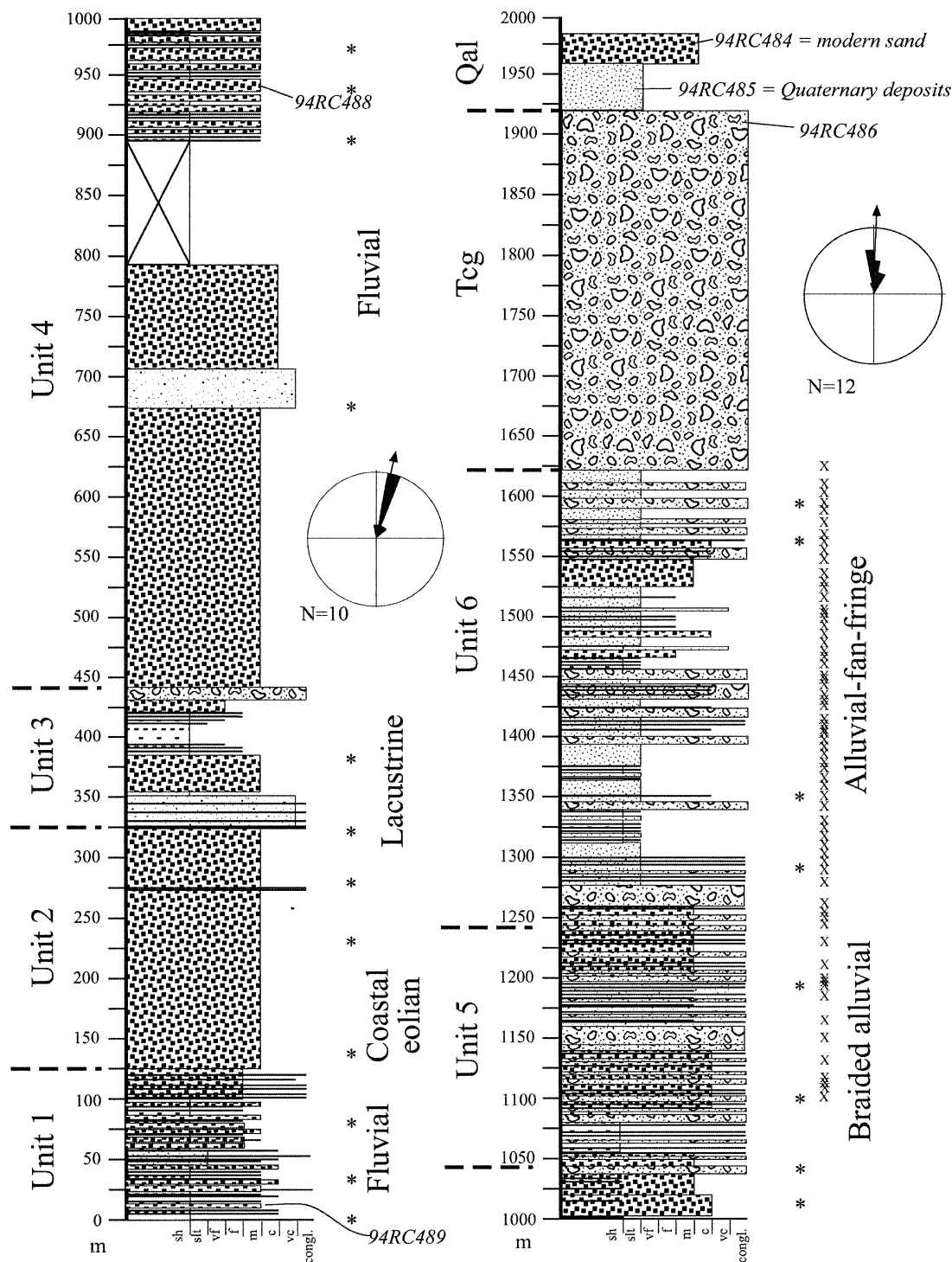


Figure 10. Lithostratigraphy of the Jianglisai section. All symbols are the same as those in Figure 6. Stratigraphic positions of fission-track samples are also shown. See text for details.

Xishuigou Section

This section is located near Subei where the east-northeast–striking Altyn Tagh fault makes a sharp turn to become a south-dipping thrust (= Subei thrust; Figs. 2 and

11). The Xishuigou section is folded and locally deformed by minor north-verging thrusts. The restored stratigraphic section is shown in Figure 12. Because the base of the section is not exposed, the age of the measured section only provides an upper-age

bound for Cenozoic sedimentation in the western Nan Shan. We divide the measured section into four units. Unit 1 (~900 m) is sandstone interbedded with conglomerate channels, claystone, and siltstone. Clasts in the conglomerate are granitic, metavolcanic,

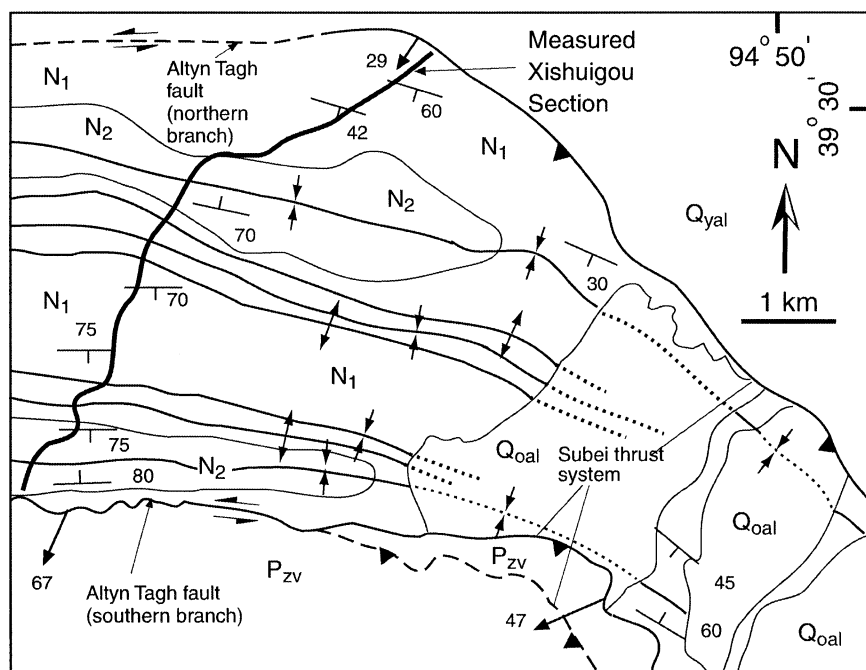


Figure 11. Simplified geologic map of the Xishuigou area and the location of the measured section. Symbols in the map: Pzv—Paleozoic metavolcanic rocks; N₁—older Tertiary unit, characterized by fine-grained deposits corresponding to units 1 and 2 in our measured section; N₂—younger Tertiary deposits, characterized by coarse-grained deposits and corresponding to units 3 and 4 in our measured section.

and phyllitic. Units 2–4 represent a coarsening-upward sequence. Specifically, unit 2 (~400 m) consists of conglomerate interbedded with claystone and siltstone. Clasts in the conglomerate are mainly granitic and metavolcanic rocks with subordinate amounts of phyllite

and quartzite, which can be correlated to lithologies in the hanging wall of the Subei thrust (Liu, 1988). Unit 3 (~340 m) consists of mostly pebble to boulder conglomerate interbedded with sandstone. The most abundant clasts are angular and consist of dark-

green mafic intrusive rocks; phyllite, schist, and quartzite are subordinate. Unit 4 (~260 m) consists of conglomerate interbedded with sandstone and rare claystone or siltstone. On the basis of the clast composition and paleocurrent directions, we interpret the entire Xishuigou section to be related to uplift and denudation of the Danghe Nan Shan above the Subei thrust.

AGE CONSTRAINTS

Biostratigraphic Constraints

Aertashi

The age of the thick (900–1600 m) Paleogene marine strata is crucial in defining the onset age of Cenozoic deformation in the western Kunlun Shan. The Aertashi Formation contains bivalves and was assigned to the early Paleocene (p. 42, Lan and Wei, 1995). The Qimugen Formation contains bivalves and ostracods and was assigned to the late Paleocene to early Eocene (Lan and Wei, 1995; Yang et al., 1995). The Kalatar Formation contains bivalves and ostracods indicative of a middle Eocene age (p. 43, Lan and Wei, 1995; p. 15, Yang et al., 1995). The Wulagen Formation contains abundant bivalves and was assigned to the middle Eocene (p. 37, Lan and Wei, 1995; p. 38, Yang et al., 1995).

The Bashibulake Formation is commonly divided into five members in the western part of the southern Chinese Tian Shan (Hao and Zeng, 1984; Sobel, 1995; Yang et al., 1995).

TABLE 1. APATITE FISSION-TRACK DATA

Sample number	Grains (number)	Standard track density ($\times 10^6 \text{ cm}^{-2}$)	Fossil track density ($\times 10^6 \text{ cm}^{-2}$)	Induced track density ($\times 10^6 \text{ cm}^{-2}$)	Uranium content (ppm)	Chi square probability (%)	Age dispersion (%)	Fission-track age* (Ma) ($\pm 1\sigma$)	Mean track length (\pm std. error) (μm)	Std. dev. (μm)
Basin										
XSG25	8	1.517 (5866)	0.692 (181)	2.705 (708)	22.3	7.6	18.46	72.9 \pm 7.8	11.85 \pm 0.39 (4)	0.77
XSG51	20	1.531 (5866)	0.910 (727)	13.136 (2507)	25.6	4.9	12.70	84.3 \pm 4.5	10.11 \pm 0.28 (25)	1.42
XSG60	15	1.545 (5866)	0.485 (305)	2.368 (1488)	19.2	0	33.37	58.7 \pm 6.5	N.D.	N.D.
XSG64	11	1.559 (5866)	0.435 (145)	2.696 (899)	21.6	1.7	31.26	45.5 \pm 6.1	9.31 \pm 1.17 (2)	1.65
XSG72	14	1.572 (5866)	0.873 (528)	3.082 (1864)	24.5	0	23.40	83.6 \pm 6.9	10.50 \pm 0.27 (16)	1.09
94RC484	21	1.396 (4857)	0.441 (511)	2.137 (2478)	19.1	0	100	57.5 \pm 13.1	11.74 \pm 0.35 (43)	2.28
94RC484A	7	1.415 (4857)	0.760 (387)	2.006 (1022)	17.7	0	83.78	100.9 \pm 32.7	12.21 \pm 0.23 (43)	1.53
94RC485	9	1.434 (4857)	0.830 (356)	3.575 (1533)	31.2	0	73.37	60.7 \pm 15.5	12.98 \pm 0.28 (29)	1.52
94RC485A	3	1.452 (4857)	0.395 (101)	2.691 (689)	23.2	10.2	4.05	40.3 \pm 4.5	12.83 \pm 0.41 (18)	1.76
94RC486	8	1.471 (4857)	1.006 (396)	1.662 (654)	14.1	0	40.54	151.0 \pm 24.8	12.49 \pm 0.84 (12)	2.92
94RC486A	20	1.490 (4857)	0.947 (1078)	2.595 (2954)	21.8	0	67.47	108.5 \pm 17.1	12.65 \pm 0.29 (64)	2.31
94RC488	14	1.509 (4857)	1.063 (537)	3.767 (1902)	31.2	0	53.88	89.4 \pm 13.8	12.41 \pm 0.25 (51)	1.82
94RC488A	3	1.527 (4857)	2.252 (147)	5.867 (383)	48	0	62.69	101.0 \pm 37.9	12.72 \pm 0.45 (17)	1.86
94RC489	1	1.546 (4857)	0.406 (26)	0.891 (57)	7.2	100	0	132.6 \pm 31.5	12.15 \pm 0.48 (4)	0.97
94RC489A	3	1.565 (4857)	1.021 (147)	1.861 (268)	14.9	32.2	0.04	161.0 \pm 16.7	12.50 \pm 0.38 (17)	1.57
ARTSSSTOP	1	1.584 (4857)	0.156 (12)	2.721 (209)	21.5	100	0	17.3 \pm 5.1	15.55 (1)	N.D.
ARTSSMID	2	1.602 (4857)	2.068 (180)	7.571 (659)	59.1	0	78.90	139.1 \pm 78.6	11.90 \pm 0.72 (7)	1.92
ARTSSBOT	1	1.640 (4857)	5.424 (243)	7.612 (341)	58.0	100	0	218.3 \pm 18.8	11.84 \pm 0.99 (4)	1.99

Note: Brackets show number of tracks counted or measured. Standard and induced track densities measured on external mica detectors ($g = 0.5$) and fossil-track densities on internal mica surfaces. N.D.—not determined.

*Apatite ages calculated by using zeta factor of 380 ± 5 (from A. Raza) for dosimeter glass CN-5. All ages are central ages (Galbraith and Laslett, 1993).

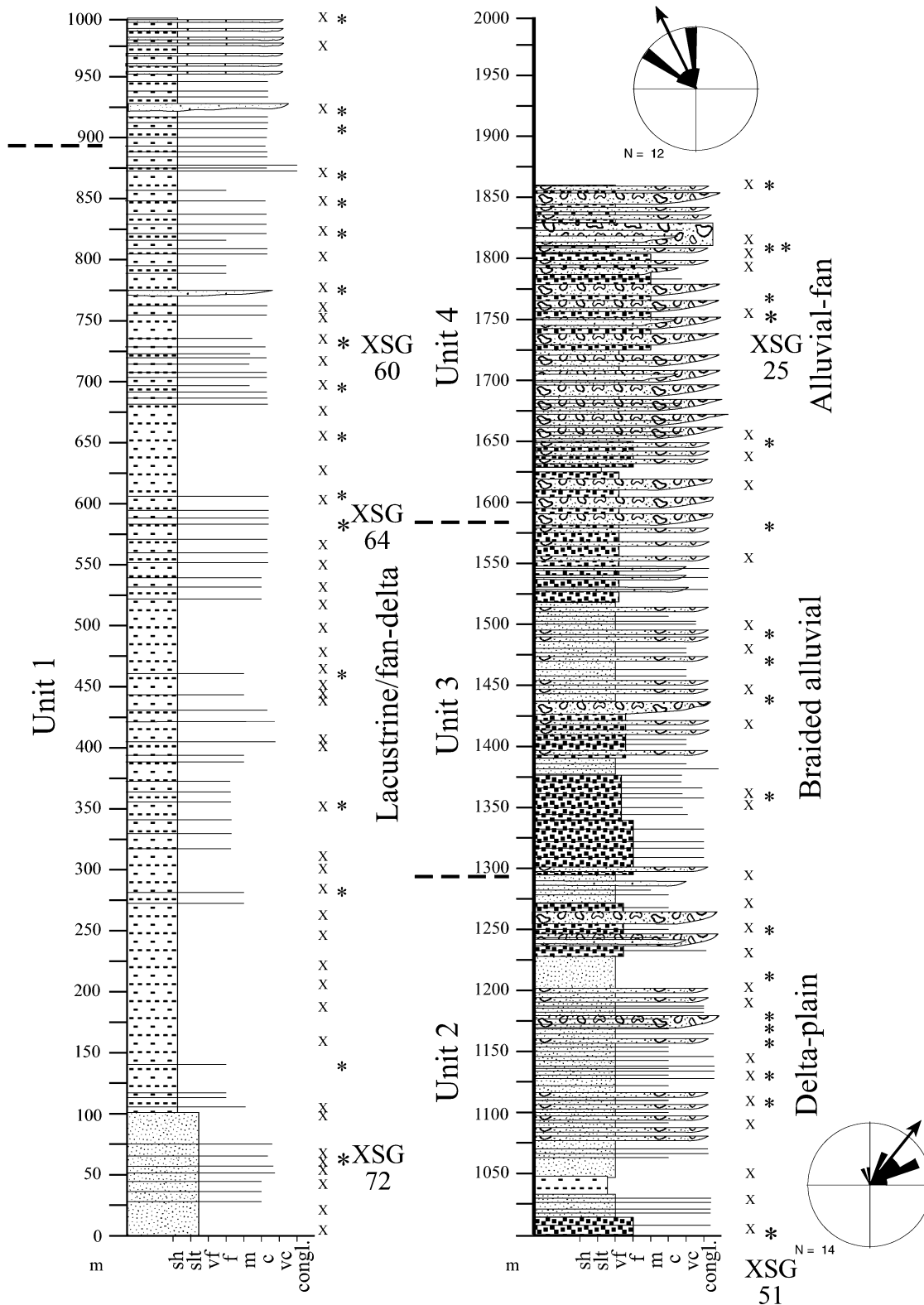


Figure 12. Lithostratigraphy of the Xishuigou section. See Figure 6 for lithologic symbols. Locations and numbers of fission-track samples are also shown.

A Aertashi Section

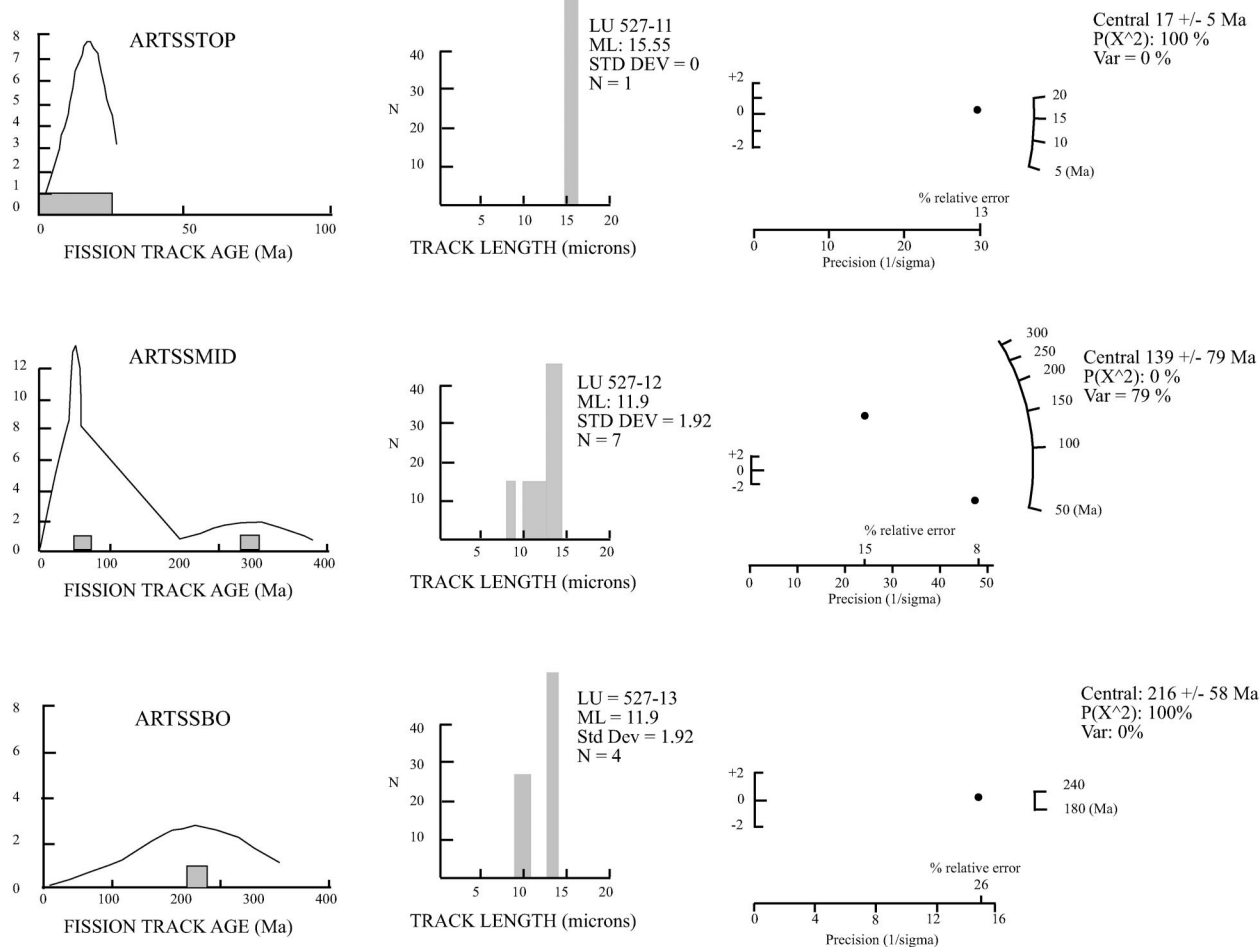


Figure 13. (A) Fission-track data for samples from the Aertashi section. (B) Fission-track data for samples from the Xishuigou section. (C) Composite probability plots for single-grain detrital-apatite fission-track data from Xishuigou section (Brandon, 1992). Plots with high-amplitude narrow peaks indicate greater accuracy. Samples are in stratigraphic order; that is, stratigraphic lowest samples are at the bottom of the figure. (D) Fission-track data from samples collected at Jianglisai. See text for details.

Most researchers (e.g., Ye and Huang, 1990) agree that its lower three members are lower Eocene to middle upper Eocene on the basis of the age of bivalves. The bivalve assemblage in the upper fourth and fifth members suggests a late Eocene–early Oligocene age (Lan and Wei, 1995; Yang et al., 1995), although calcareous nannofossils indicate a late Eocene age (Zhong, 1989, 1992). In our magnetostratigraphic analysis, we assume that this formation was deposited in the late Eocene to the earliest Oligocene (between 37 and 32 Ma). Our measured section is ~200 m above the top of the Bashibulake Formation.

Puska

Bivalves of *Ostrea (Turkostrea) striplicata* are abundant in the carbonate horizon of unit I in our measured section. They are characteristic of the middle Eocene Kalatar Formation in the western Kunlun Shan (p. 16, Yang et al., 1995).

Western Nan Shan Thrust Belt

Bohlin (1942, 1946) first recognized and studied the mammal fossils at Xishuigou and considered them to be late Oligocene. Regional correlation of Bohlin's mammal fossils with those in the Inner Mongolia

suggests that their age could be as old as early Oligocene (Zhai and Cai, 1984). Bohlin's fossil list was examined by W.R. Downs (cited as personal commun. by Wang, 1997), who concluded the age of the listed fossils to be at the Oligocene/Miocene transition but certainly not younger than 16 Ma. This age inference, slightly younger than Bohlin's early interpretation, has not been demonstrated rigorously by correlating individual mammal species to well-dated localities in Asia elsewhere, an approach Bohlin (1942, 1946) and Zhai and Cai (1984) took.

B Xishuigou Section

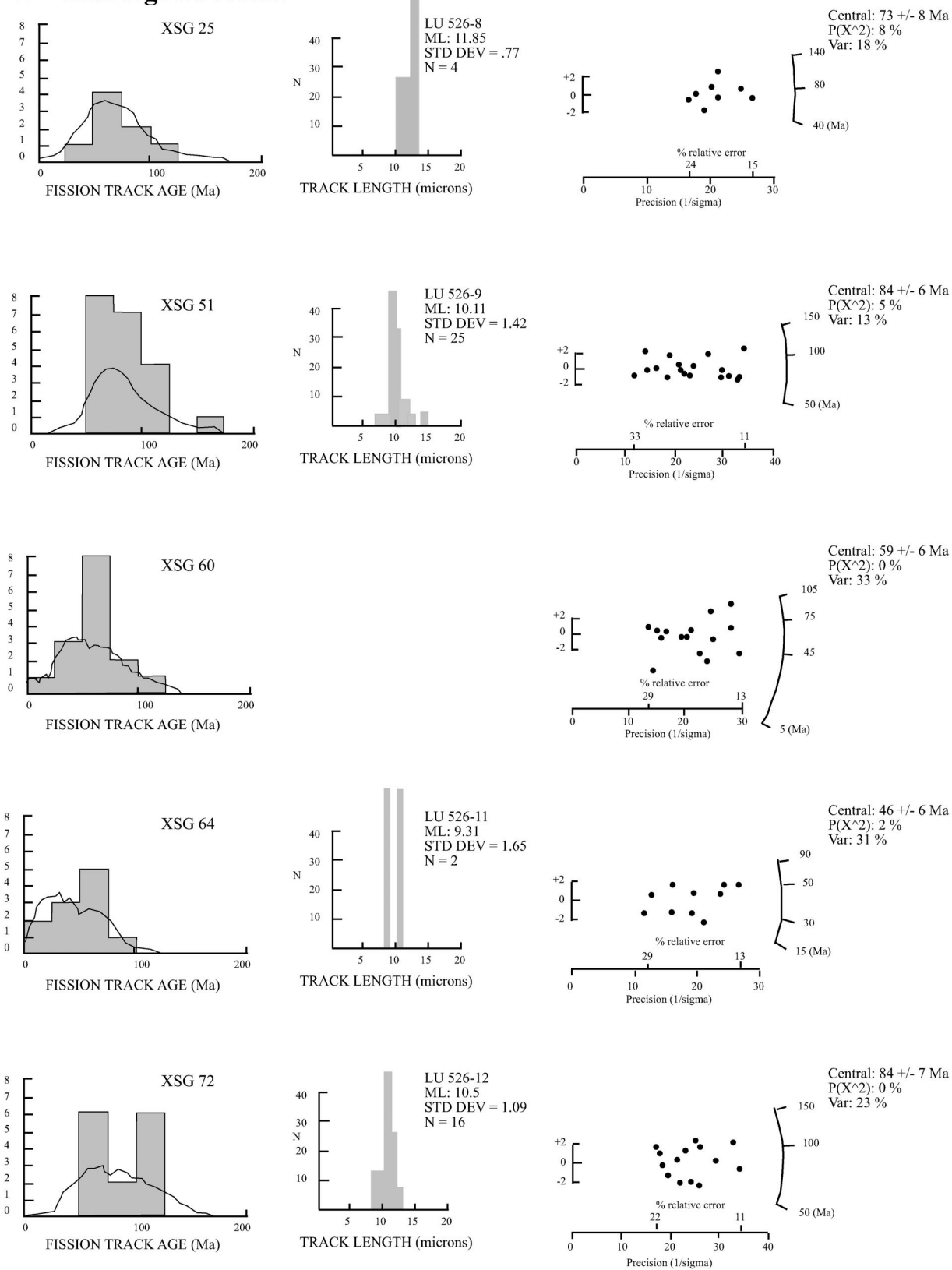


Figure 13. (Continued.)

C Xishuigou Section

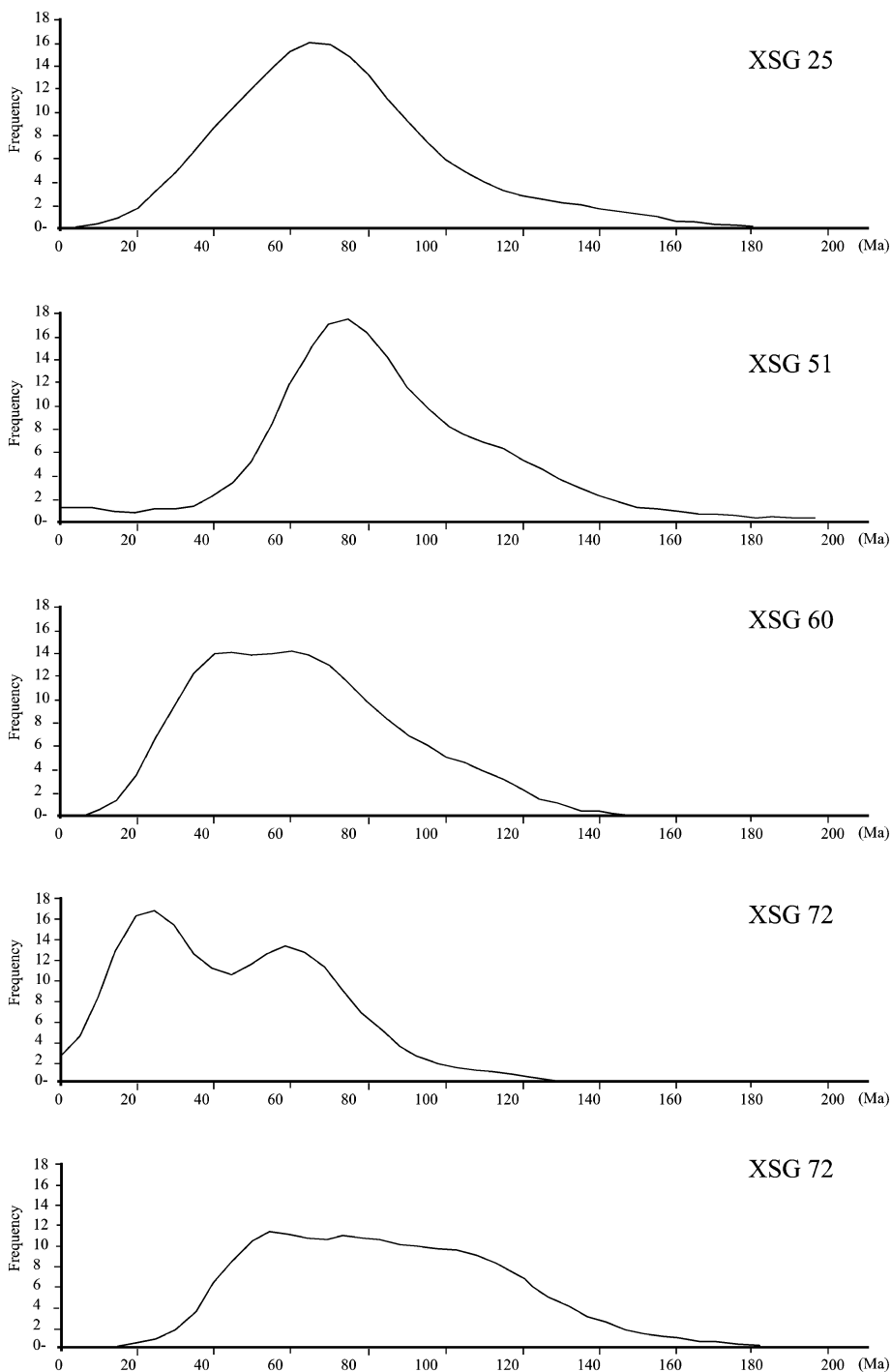


Figure 13. (Continued.)

Fission-Track Dating of Detrital Apatites

Fission-track analyses of detrital apatites separated from sandstones of the Aertashi, Jianglisai, and Xishuigou sections were undertaken at the University of Melbourne, Aus-

tralia (Table 1). Because fission tracks in apatite anneal at $\sim 60\text{--}120^\circ\text{C}$ (e.g., Green et al., 1989a, 1989b; Gallagher et al., 1998), little denudation in the source terrane can yield completely annealed apatites that are transported to a basin. Without reheating, the de-

trital apatite age provides the oldest-age bound for sedimentation. However, if the apatite is heated by burial to temperatures above $\sim 60^\circ\text{C}$, it would be partially annealed and its fission-track lengths (and thus track density) would be reduced, resulting in an underestimate of

D Jianglisai Section

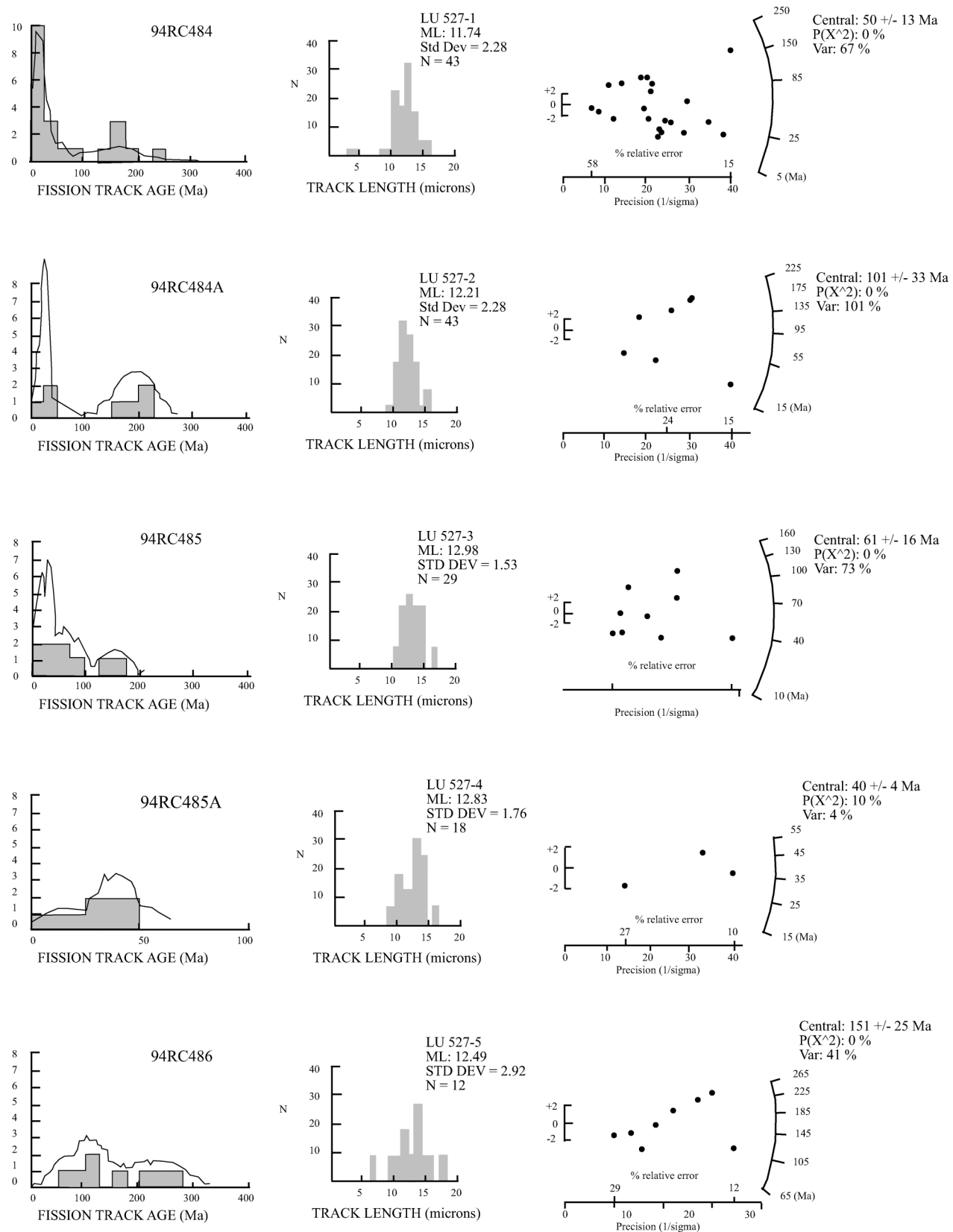


Figure 13. (Continued.)

D (Continued)

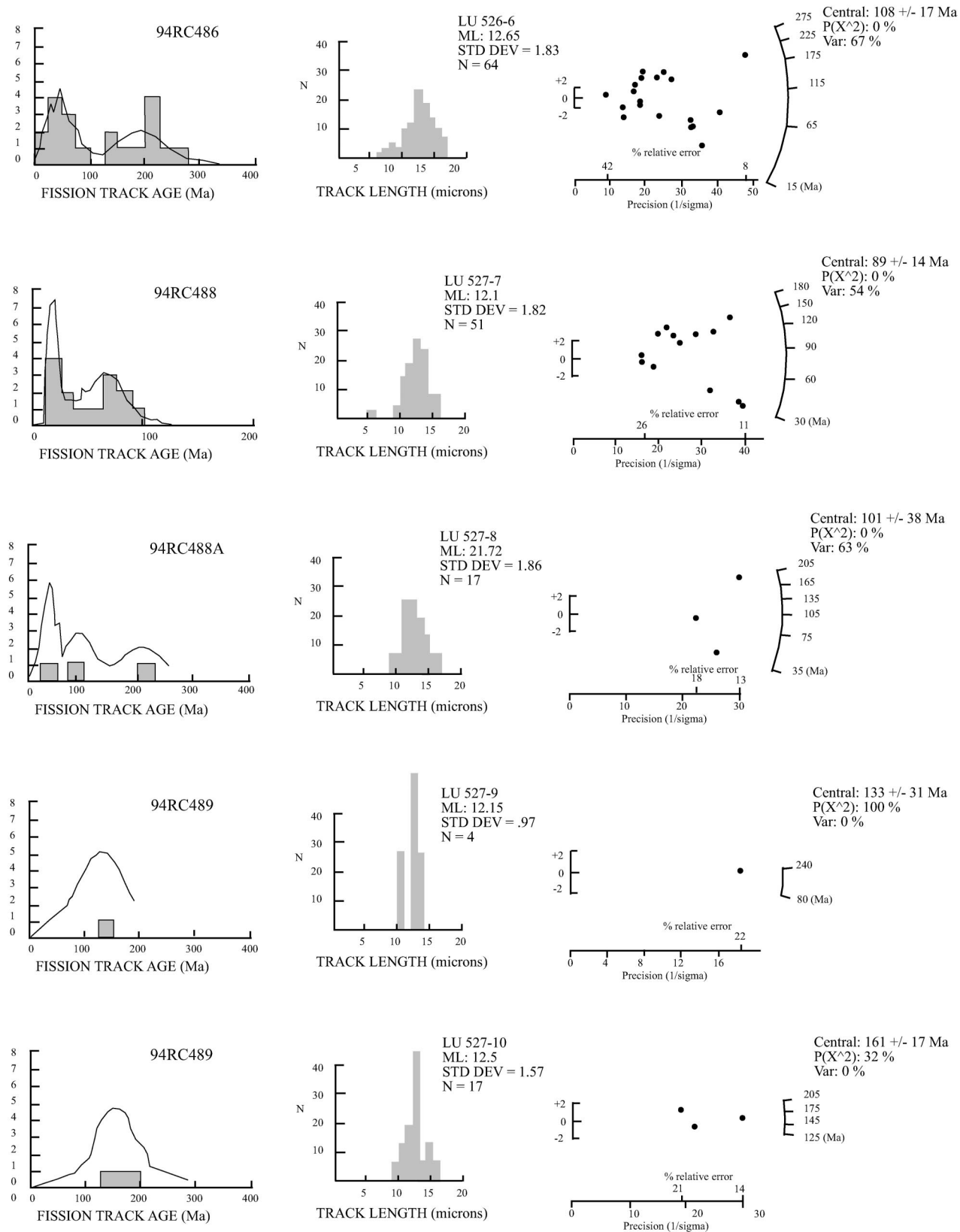


Figure 13. (Continued.)

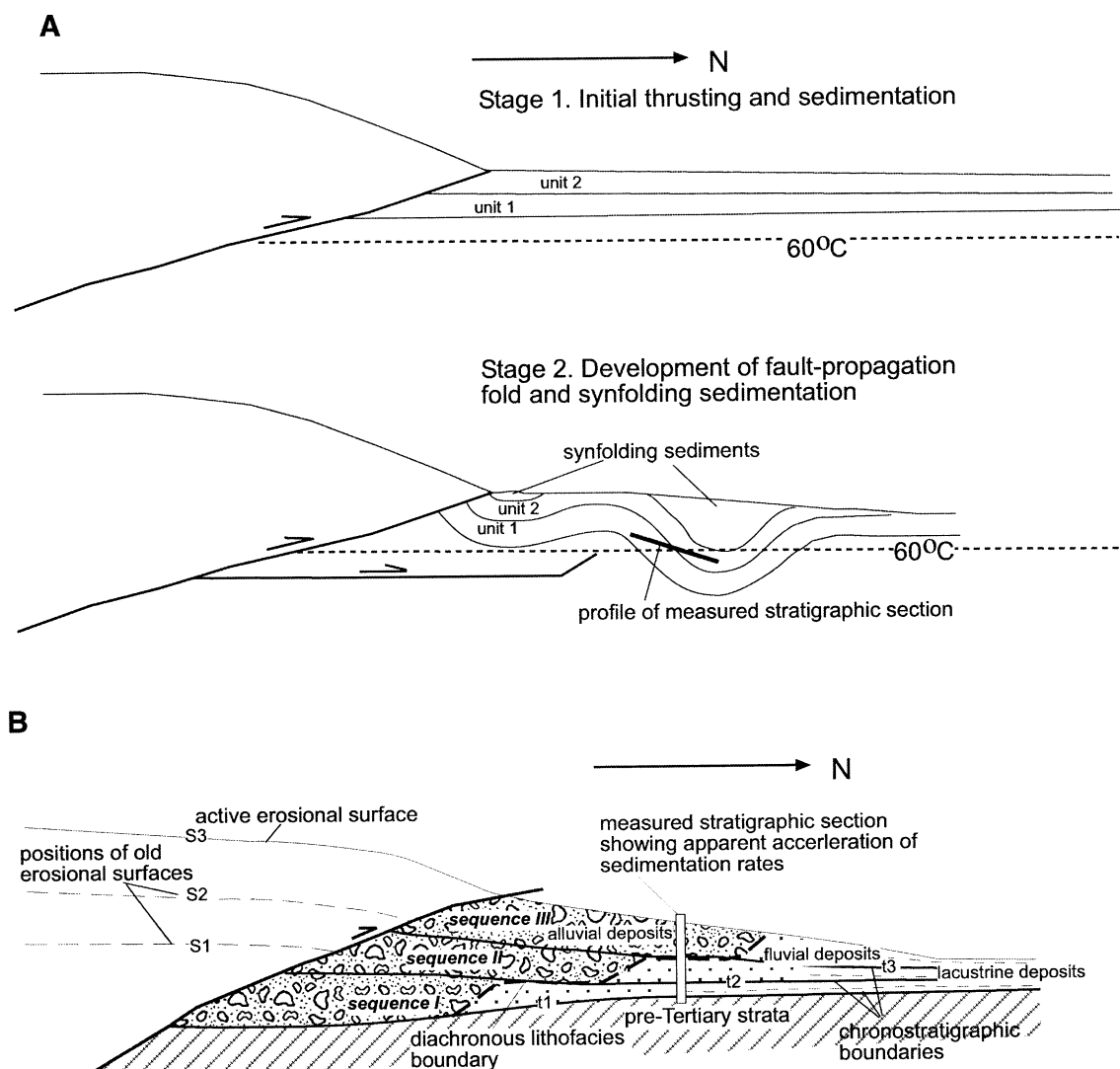


Figure 14. (A) A structural model explaining the role of synfolding sedimentation in causing partial annealing of apatite fission tracks in the younger strata. (B) A schematic diagram illustrating coarsening-upward sedimentation and apparent acceleration of sedimentation rates due to steady-state forward migration of a thrust front.

depositional age (e.g., Gleadow and Duddy, 1981; Gallagher et al., 1998). Using these properties as a guide allows us to discuss the age constraints of our measured sections by the fission-track analysis of apatites.

Aertashi Section

Ten samples of ~0.5 kg each were amalgamated into three composites: Samples from the upper 500 m formed the ARTSSTOP composite (unit 3 and the entire unit 4, Fig. 6), samples from unit 2 and lower part of unit 3 formed the ARTSSMID composite, and samples from the bottom part of unit 1 formed the ARTSSBOT composite. Following standard heavy-liquid mineral separation, only one dateable grain was obtained from each of the

top and bottom composites and two from the middle composite (Fig. 13A).

Because only 12 spontaneous tracks were observed in the single grain from the ARTSSTOP sample, the resulting age of 17 ± 10 Ma is highly uncertain (note that all uncertainties cited herein are $\pm 2\sigma$). The single track length measured in this grain of $15.6 \mu\text{m}$ is typical of an unannealed sample (Gleadow et al., 1986), which implies the upper section to be no older than 27 Ma. However, the long track length may also be attributed to high Cl content, and the sample may in fact have undergone partial annealing (Sobel and Dumitru, 1997). Sobel and Dumitru (1997) reported fission-track ages of detrital apatite from Tertiary strata of the Aertashi area. In one of their samples (sample

A1), about half of the 20 grains examined yielded an age of 30 ± 5 Ma, and the rest have much older ages. The track-length distribution of their sample ($\bar{x} = 10.6 \pm 0.3 \mu\text{m}$) may have resulted from partial annealing. However, because the track lengths associated with the ca. 30 Ma population were not specifically identified, the degree of annealing of that component is unknown. From the sample location and its associated lithofacies provided by Sobel and Dumitru (1997), it appears that their sample A1 is from either the uppermost part of or above our measured section. If their sample has undergone partial annealing, it implies that most of our measured section is older than ca. 25 Ma and could be even older than 35 Ma.

A Aertashi section

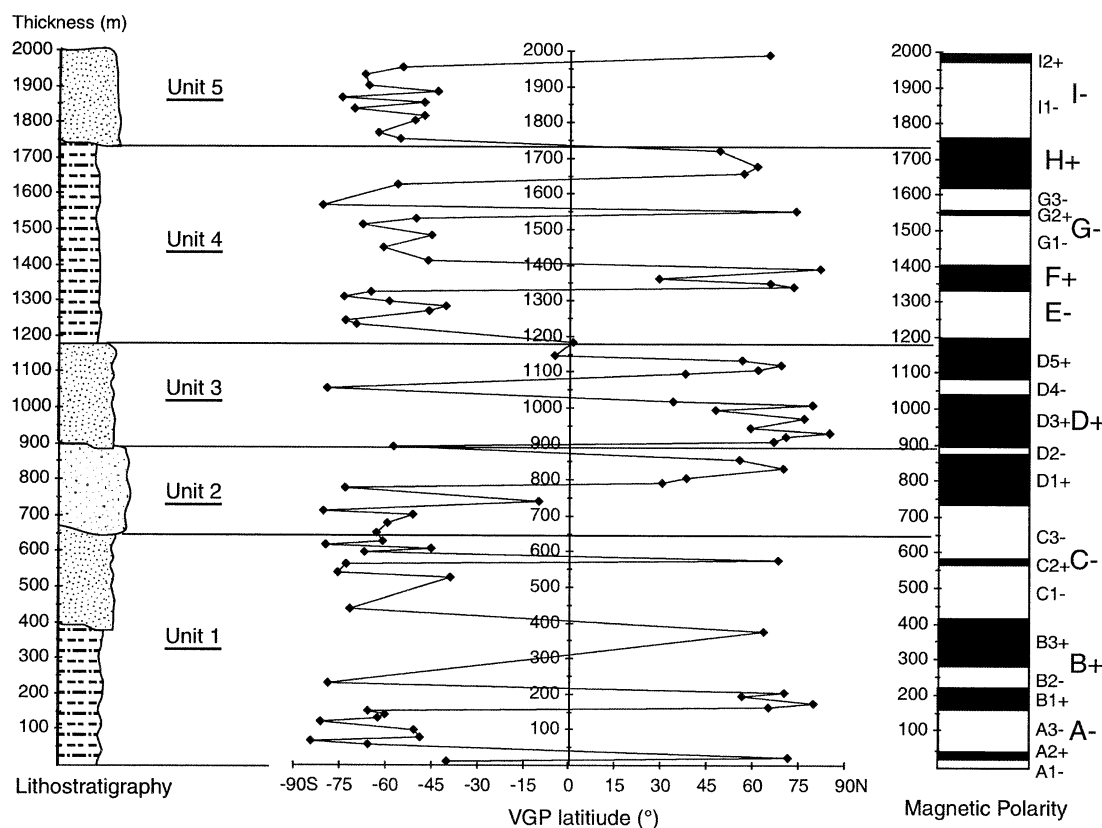


Figure 15. (A) Latitude of virtual geomagnetic poles (VGPs) and interpreted polarity stratigraphy for the Aertashi section. Each datum represents a site-mean VGP latitude; positive VGP latitude indicates normal polarity and negative VGP latitude indicates reverse polarity. Magnetic polarity zones are designated “+” for normal polarity and “-” for reversed polarity and are labeled alphabetically from the base of the section with subzones defined by single sites. This procedure correctly emphasizes the major polarity zones while including subzones that are given less weight in correlations with the geomagnetic polarity time scale (GPTS). (B) Magnetostratigraphic correlation of the Aertashi section to the geomagnetic polarity time scale of Cande and Kent (1992, 1995). Arrows indicate primary tie lines from magnetic-polarity sequence to GPTS. Older correlation marked by * is preferred; see discussion in text.

Two of the three apatite grains from the sample ARTSSMID and ARTSSBOT samples yielded ages of >200 Ma, and one high-U (~ 70 ppm) grain from the ARTSSMID composite sample yielded an age of 52 ± 11 Ma. These results suggest negligible annealing of the middle and lower sections and contradict partial annealing of apatites in the uppermost section. It is possible that the upper part of the section was located closer to the axis of a growing syncline, receiving synfolding sedimentation. This process could avoid the lower part of the stratigraphic section having to have been buried below the depth for partial annealing of apatite (Fig. 14A).

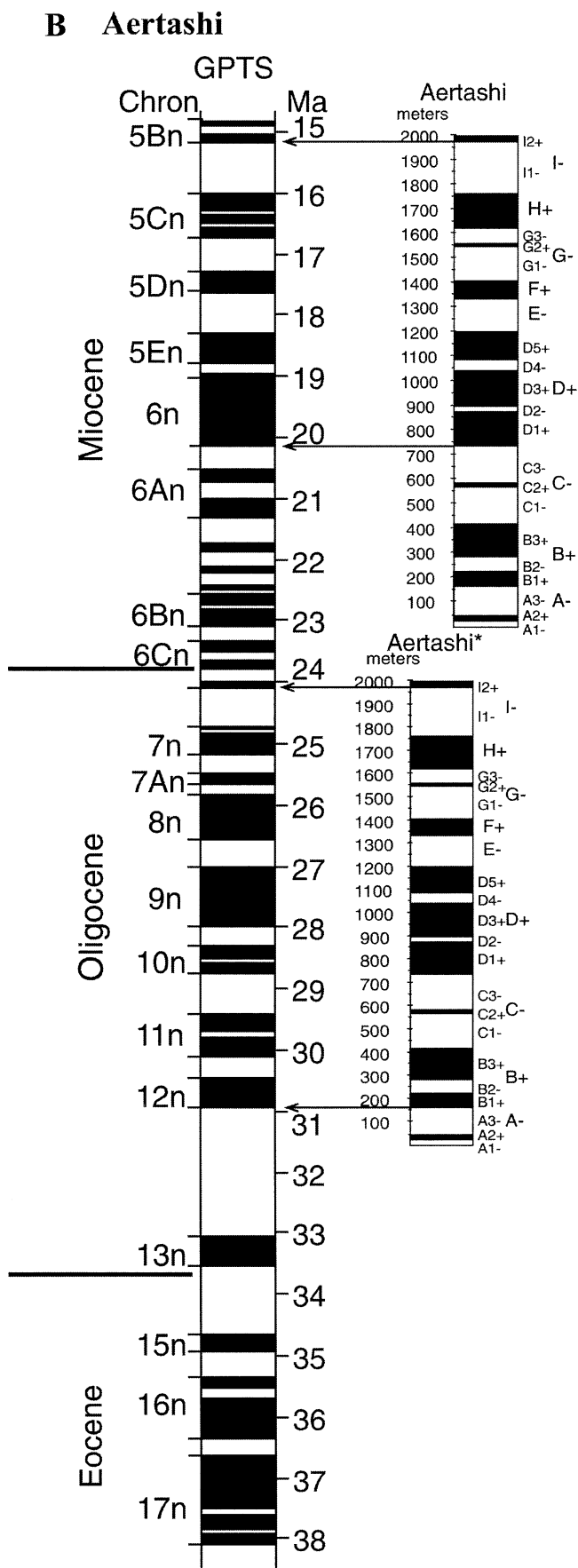
Xishuigou Section

Five samples from the Xishuigou section were processed to obtain detrital apatites, and each provided adequate yields for fission-track

dating. The sample locations in the stratigraphic section are shown in Figure 12. Ideographs and radial plots of the results for the five samples are shown in Figure 13B. The stratigraphically lowest sample (XSG72) shows both a significant scatter in age and narrow track-length distribution ($\bar{x} = 10.5 \pm 1.1 \mu\text{m}$), indicating that the sample has not been subject to temperatures in excess of ~ 100 °C subsequent to burial. Sample XSG64 shows a bimodal distribution and a shift to younger ages relative to XSG72 (Fig. 13C). The single-grain ages fail a χ^2 test, indicating scatter beyond statistical variation. The two populations are most clearly separated on the radial plot (Galbraith, 1990). The Kolmogorov-Smirnoff test (Press et al., 1992) for similarity indicates that the two age populations in sample XSG64 (XSG64-A and XSG64-B) are different at the 98% confidence level. XSG64-A has a mean

age of 29 ± 4 Ma, whereas XSG64-B has a mean age of ca. 63 Ma. By sequentially applying the Kolmogorov-Smirnoff test to population XSG64-A against the other samples, it can be demonstrated that XSG64-A is a different population at greater than the 99% confidence level. The minimum fission-track age of 29 ± 4 Ma may suggest that the depositional age of the Xishuigou section from the middle of unit 1 upward (see Fig. 12) is younger than 33–25 Ma, provided that the sample has not undergone annealing following burial. However, the assumption of negligible annealing is questionable because of the $\sim 9 \mu\text{m}$ length of the two measured tracks for the sample. Because annealing reduces the age of the sample, it requires that the deposition of the Xishuigou section from the middle of unit 1 downward to be older than 29 ± 4 Ma.

Sample XSG60 yields a broad ideograph



and divergent radial plot (Fig. 13B). This result could indicate a mixture of source ages. The sharp drop in the probability distribution at younger ages suggests that the datum that defines this “edge” is not a member of a single Gaussian distribution. Apatite from this sample did not contain horizontally confined tracks, so no track-length data are shown in Figure 13B. The minimum ages of the two uppermost samples (XSG25 and XSG51) only restrict their depositional age to be less than ca. 60 Ma (Fig. 13B).

Jianglisai Section

Two samples from modern sands (94RC484, 94RC484A) and two samples from Quaternary deposits (94RC485, 94RC485A) were processed to obtain detrital apatites. Of the 28 grains in samples 94RC484 and 94RC484A, ages of 6 ± 6 Ma, 10 ± 10 Ma, and 12 ± 10 Ma were obtained (two other grains with ages within the uncertainty of a zero age contained ≤ 5 ppm U). In addition, a weighted mean of the youngest 11 grains gives an age of 8 ± 2 Ma. These results suggest that this approach for the Jianglisai section can define an upper bound for its depositional age within 10–20 m.y.

Sixty-one apatite grains were dated from the three other samples within the section. Because of the significant scatter in age (Fig. 13D) and narrow track-length distributions in the stratigraphically lowest samples (94RC488 and 94RC489), temperatures of ~ 100 °C were not exceeded during burial. Sample 94RC486 was collected from the top of a Tertiary conglomerate sequence that overlies our measured section. With 95% confidence error bounds on individual detrital apatite ages, oldest possible ages of deposition of this sample are between ca. 16 and 37 Ma, on the basis of the range of single-grain ages. A weighted mean of the seven youngest grains gives an age of 36 ± 6 Ma, which we take as the maximum age of deposition. The general uniformity of these results gives us confidence in concluding that the conglomerate (Tcg) unit above our measured section was deposited subsequent to ca. 25 Ma.

Sample 94RC488 was collected from the top part of unit 4 of the Jianglisai section (Fig. 10). This sample yielded the youngest central fission-track age of 89 ± 14 Ma ($\pm 2 \sigma$) (Fig. 12D). The single-grain ages fail a χ^2 test, indicating multiple sources. The weighted mean of the youngest grain population (seven grains) gives an age of 36 ± 7 Ma, which is the same as the mean of the younger grains from 94RC486. This result supports the interpretation that this deposit is younger than ca.

Figure 15. (Continued.)

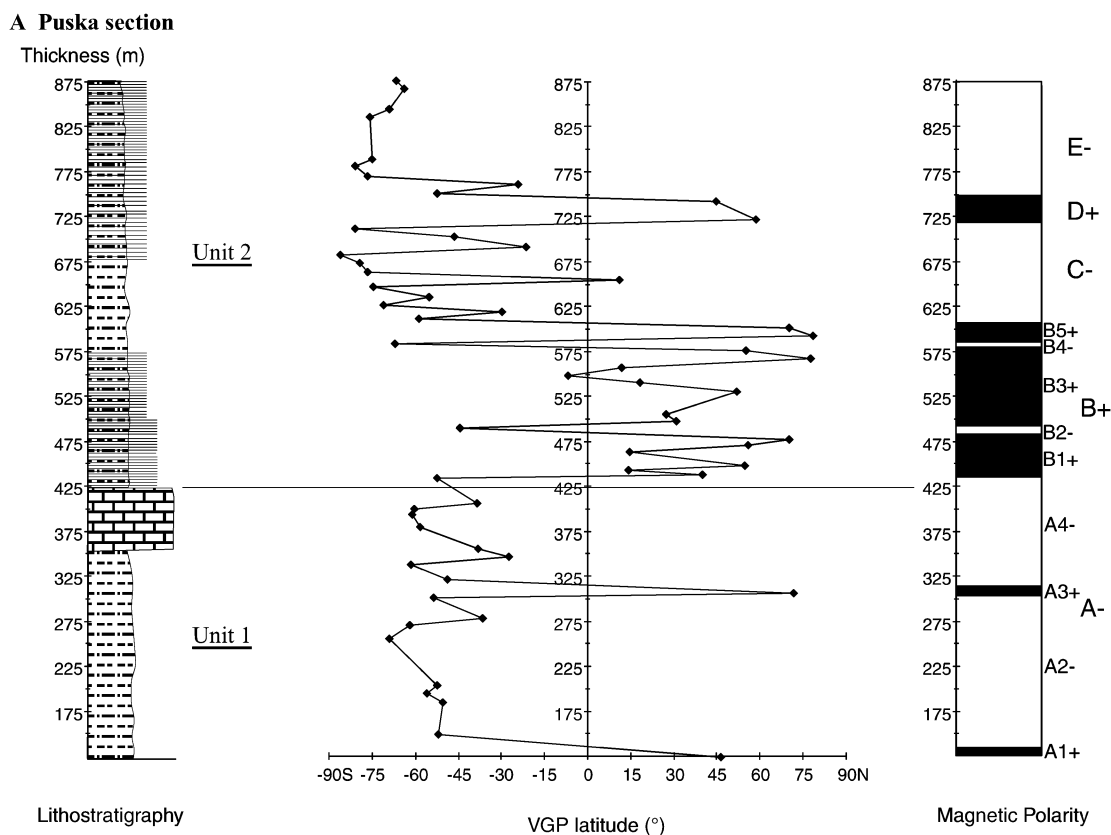


Figure 16. (A) Latitude of virtual geomagnetic poles (VGPs) and polarity stratigraphy for the Puska section. (B) Magnetostratigraphic correlation of the Puska section to GPTS. Symbols same as in Figure 14. Preferred correlation is indicated by *; see discussion in text.

36 Ma. Detrital-apatite grains in sample 94RC489 are dominated by Mesozoic ages that are not useful in defining the Cenozoic age of the Jianglisai strata.

MAGNETOSTRATIGRAPHY

Paleomagnetic samples were collected as standard paleomagnetic cores (Aertashi, Puska, and Jianglisai sections) or oriented hand samples (Xishuigou section). At a single site, three to five samples were collected. Stratigraphic intervals between sampling sites were 4–15 m. All samples were analyzed at the Paleomagnetic Laboratory of the University of Arizona. Following preparation, all paleomagnetic specimens were stored, demagnetized, and measured within a magnetically shielded room with average field intensity of <200 nT. The magnetic field inside the thermal-demagnetization furnaces was <10 nT. Measurements of natural remanent magnetization (NRM) were made with a three-axis cryogenic magnetometer (2G Model 755R). Alternating-field demagnetization was attempted for a few test specimens but produced little response. Thermal demagnetization employed 8 to 18

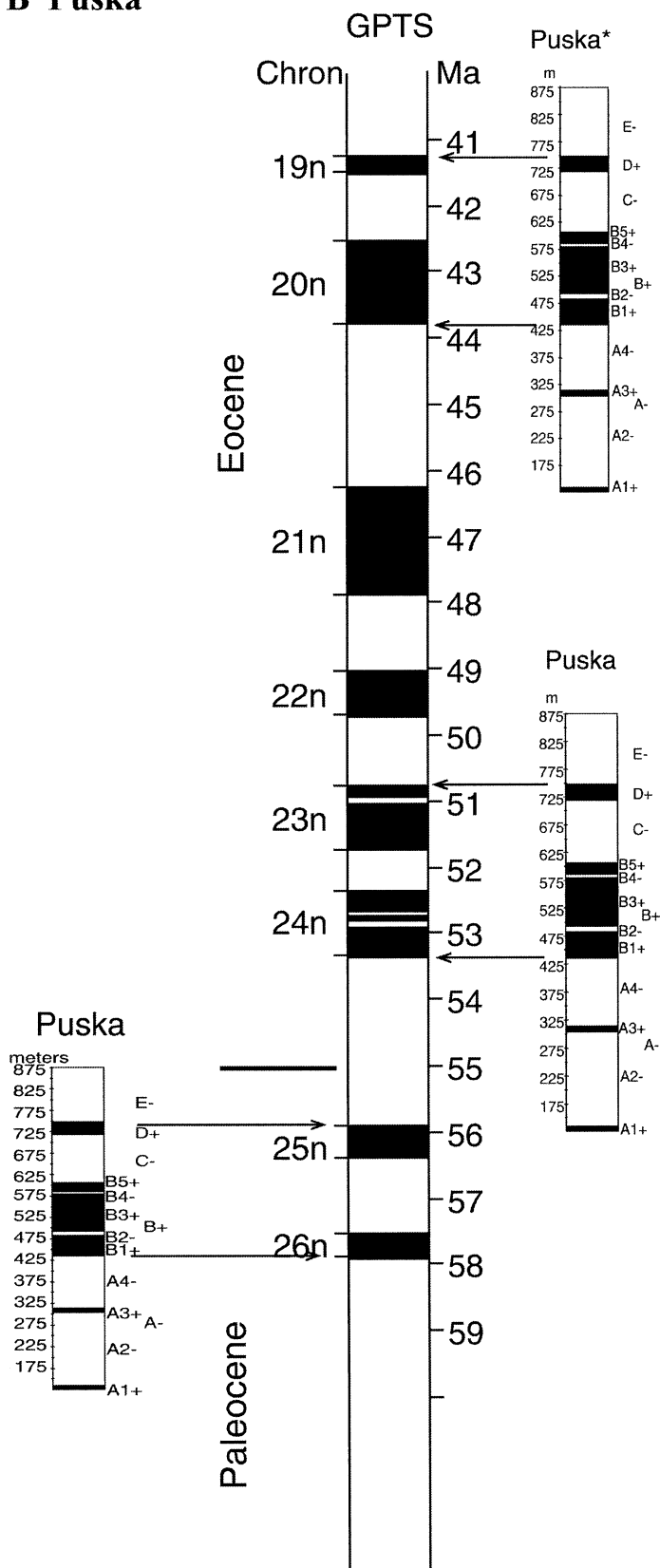
temperature steps from 250 to 710 °C. Demagnetization at 10 °C increments above 650 °C was commonly necessary to adequately determine the characteristic remanent magnetization (ChRM) carried by hematite. Demagnetization behaviors are discussed in Rumelhart (1998). Principal-component analysis (Kirschvink, 1980) was applied to results from three to six temperature steps to determine specimen ChRM directions. Typical maximum angular deviation (MAD) was 3°–15°, although ChRM directions with MAD < 25° were used to compute site-mean ChRM directions (Fisher, 1953). Resulting site-mean ChRM directions are tabulated in Rumelhart (1998).

Because each section is exposed as a homocline, the grouping of site-mean ChRM directions within individual sections is only slightly improved by application of the bedding-tilt correction. Further complicating this analysis is the observation that the sampling region has undergone differential vertical-axis rotation (Rumelhart et al., 1999). However, major differences in bedding attitude do exist between the four sampled sections, permitting a regional inclination-only bedding-tilt test to be applied (McFadden and Reid, 1982; Richards

et al., 1993). This test is positive at the 0.1% significance level, indicating that the sampled sections were at least coplanar, if not necessarily horizontal, at the time of ChRM acquisition (Burmester et al., 1990). Given the wide geographic distribution of sampling locations, it is a virtual certainty that the sections were horizontal at the time of ChRM acquisition. We conclude that the ChRM was most likely acquired at or soon after deposition.

Determination of sediment-accumulation rates associated with various sedimentary facies is an important aspect of magnetostratigraphic analysis (e.g., Burbank et al., 1996). Sadler (1981) showed that, at a million-year time scale, fluvial sediment-accumulation rates varied from 0.01 to 1.0 m/k.y., although more proximal facies may have higher accumulation rates (Burbank and Reynolds, 1988; Jordan et al., 1988; Beer, 1990). In the following analysis, correlations of our magnetostratigraphic sections with the geomagnetic polarity time scale (GPTS) are presented; constraints from the fission-track ages and biostratigraphy already described are used. Sedimentation rates were then calculated to

B Puska



assure that implied sediment-accumulation rates are reasonable.

Aertashi Section

Of the ~140 sampled sites, 86 yielded usable data, resulting in a 22.5 m average sampling interval. The antipode of the mean of reverse-polarity sites is within 3.9° of the mean for normal-polarity sites. Therefore, the Aertashi section passes the reversal test (and the bedding-tilt test, as already discussed) with C classification (McFadden and McElhinny, 1990). Figure 15A shows the latitudes of the virtual geomagnetic poles (VGPs), interpreted polarity zones, and lithostratigraphy for the Aertashi stratigraphic section. As already discussed, the Aertashi section is younger than ca. 31 Ma, the youngest age of the Bashibulake Formation below our measured section. Because apatites in the uppermost part of the Aertashi section may have undergone partial annealing at 30 ± 5 Ma (Sobel and Dumitru, 1997), the section should be younger than 25 Ma. By using biostratigraphic constraints alone and a reasonable range of sedimentation rates (0.1–1.0 m/k.y.) for the depositional settings we determined, we derived two possible correlations of the magnetic polarity stratigraphy to the GPTS (Fig. 15B). The younger correlation suggests that the measured section was deposited between ca. 23 and 15 Ma, whereas the older correlation implies deposition between 31 and 24 Ma. If the younger correlation is correct, it implies a 9-m.y.-long hiatus between the top of the Bashibulake Formation and the base of our measured section, which we consider to be highly unlikely. The younger correlation also violates the age constraints derived from the fission-track studies as discussed earlier.

Puska Section

At Puska, 61 of the 100 paleomagnetic sites yielded useful data, resulting in a 12.3 m average sampling interval. The antipode of the mean of reverse-polarity sites is within 9.5° of the mean for normal-polarity sites, although the reversal test for the Puska section was indeterminate. The resulting polarity stratigraphy is illustrated in Figure 16A. Each zone contains at least two sites and is well defined, except for the top of zone E- and the base of zone A-, which are not exposed. The relatively small thickness of the Puska section with resulting small number of polarity zones makes unique correlation with the GPTS challenging (Fig. 16B). Three possible correlations of the Puska polarity sequence with the

Figure 16. (Continued.)

A Jianglisai section

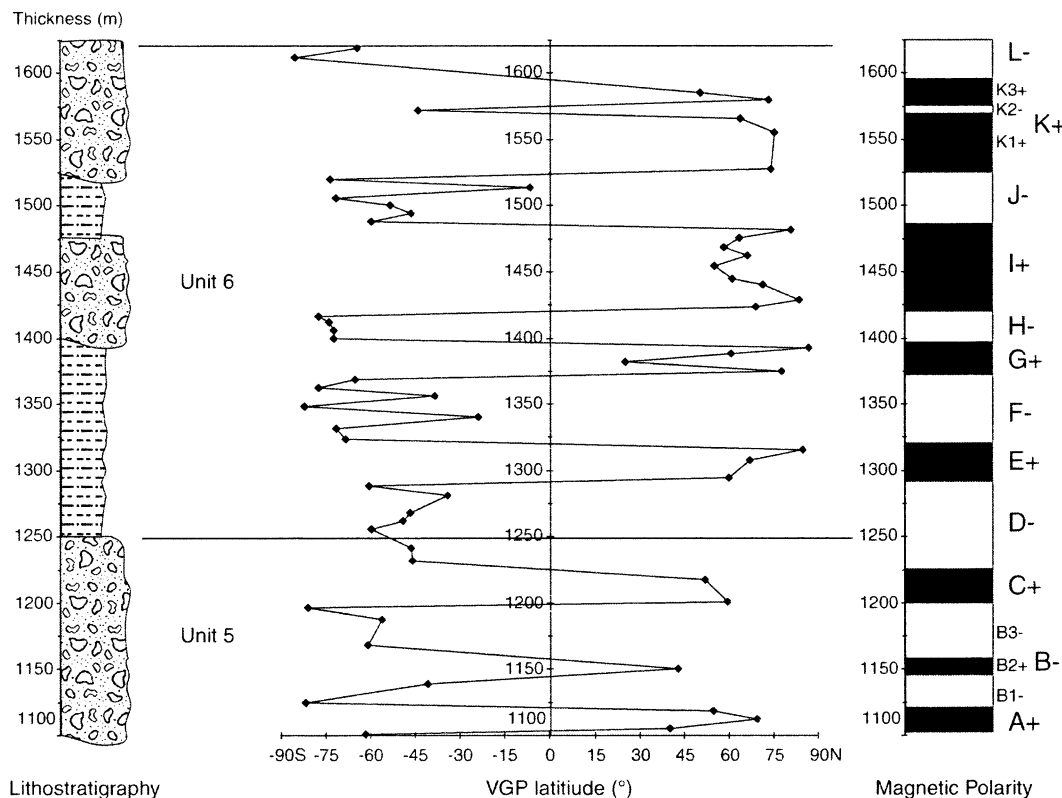


Figure 17. (A) Latitude of virtual geomagnetic poles (VGPs) and polarity stratigraphy for the Jianglisai section. (B) Correlation of magnetic-polarity sequence to GPTS. Symbols as in Figure 14. Preferred correlation is indicated by *; see discussion in text.

GPTS imply ages ranging from late Paleocene to middle Eocene. The youngest correlation is suggested by the presence of middle Eocene *Ostrea (Turkostrea) striplicata* at Puska. This correlation implies that the section was deposited from ca. 46 Ma to ca. 40 Ma and thus contains the oldest rocks sampled in our study. The implied sedimentation rates are in the range 0.10–0.14 m/k.y.

Jianglisai Section

At Jianglisai, the 61 of 138 paleomagnetic sites that yielded useful data are concentrated in the upper ~500 m of the 2-km-thick section, resulting in an average sampling interval of 8.1 m. The antipode of the mean of reverse-polarity sites is within 13.5° of the mean for normal-polarity sites; therefore, these data pass the reversal test (and the bedding-tilt test, see previous description) with C classification (McFadden and McElhinny, 1990). The sequence of magnetic polarity zones and possible correlations to the GPTS are illustrated, respectively, in Figure 17. No fossils were found in the measured section, so there are no biostratigraphic age constraints. However, the

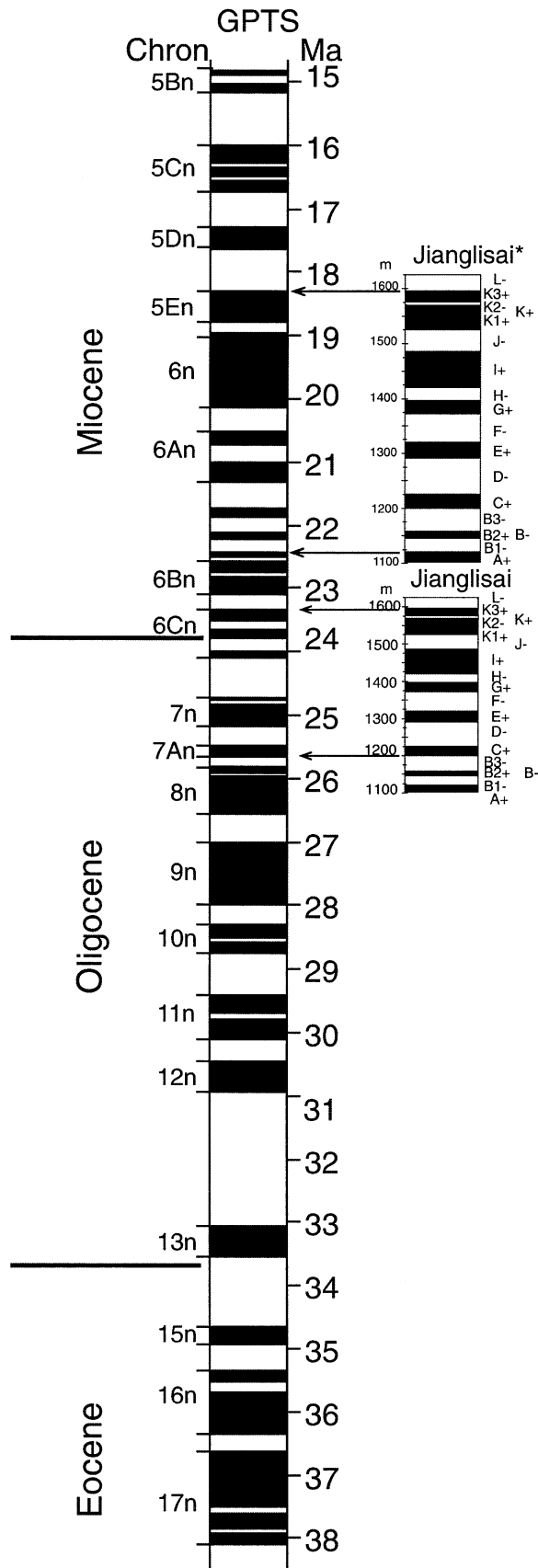
top part of unit 4 is younger than 32.6 ± 11.8 Ma ($\pm 2\sigma$)—the youngest fission-track ages of detrital apatites. As already discussed, the conglomerate unit overlying our measured section should be younger than ca. 25 Ma on the basis of fission-track ages of detrital apatites. By using these constraints, two possible correlations are evident; the younger correlation indicates deposition between ca. 22 Ma and ca. 18 Ma, and the older correlation indicates deposition between ca. 26 Ma and ca. 23 Ma. We favor the older correlation because deformation in the Altyn Tagh Range was already on the way at 26 ± 2 Ma, as reflected by the fission-track cooling ages (Sobel et al., 2001). Our preferred older correlation suggests that sedimentation rates varied between 0.06 and 0.48 m/k.y. (or 167 m/m.y.).

Because three-quarters of the 2000-m-thick Jianglisai section lies below the 26–23 Ma section analyzed by magnetostratigraphy, the initial age of sedimentation for the section must be much older. If we extrapolate the sedimentation rates obtained from the top 500 m down to the rest of the 1500-m-thick section, the result implies that the initial deposition of the Jianglisai section started at 35 Ma. Even

this older age estimate for the onset of Tertiary deposition in the Jianglisai must be a minimum. First, the lower part of the section is much finer grained and may have considerably lower sedimentation rates than the uppermost section. Second, the 2 km thickness of the measured section is a minimum because the base of the section is cut by the left-slip Jianglisai fault.

Xishuigou Section

At Xishuigou, 77 of the 100 paleomagnetic sites yielded useful polarity determinations for a 24-m-thick average sampling interval. Figure 12 shows sample positions within the lithostratigraphic section. The antipode of the mean of reverse-polarity sites is within 23.3° of the mean for normal-polarity sites. Because the deviation is $>20^\circ$, these data fail the reversal test (McFadden and McElhinny, 1990). We interpret this failure to indicate that the ChRM was not completely isolated by the demagnetization procedures. The possibility that structural complications are responsible is rejected because our measured section was affected by only minor thrust faults and folds.

B Jianguisai

Because the section has reasonably defined polarity zones and passes the bedding-tilt test, we conclude that the magnetostratigraphy has chronologic utility. The magnetic-polarity zonation from the section and its correlations to the GPTS are illustrated in Figure 18.

Fossils of the Xishuigou section define its deposition to be between Oligocene and early Miocene (Bohlin, 1942; Zhai and Cai, 1984; Wang, 1997). Fission-track ages of detrital apatites suggest that the middle section (sample XSG64) may have undergone partial annealing due to burial, which requires that the lower part of our measured section should be older than 29 ± 4 Ma ($\pm 2\sigma$). These age constraints lead to two possible correlations with the GPTS (Fig. 18B). The younger correlation implies that the Xishuigou section was deposited between ca. 25 Ma and ca. 19 Ma, whereas the older correlation suggests deposition between ca. 33 and ca. 27 Ma. We favored the older correlation because it not only satisfies the Oligocene fossil-age assignment of Bohlin (1942) and Zhai and Cai (1984) but also explains our fission-track age data (cf. Gilder et al., 2001). This correlation implies sediment-accumulation rates between 0.20 and 0.45 m/k.y.

SANDSTONE PETROLOGY

The sandstone and conglomerate composition of basin strata can be used to establish the provenance of sediments and the exhumation history of the source area (e.g., Dickinson, 1985; Ingersoll et al., 1986; Jordan and Gardeweg, 1988; Graham et al., 1993). To achieve this goal, a total of 133 samples was collected from the four measured sections. Because sediments of all measured sections were deposited in a continental setting, they were probably derived from first- and second-order drainage systems (Ingersoll, 1990; Ingersoll et al., 1993). All samples were stained for potassium feldspar. Modal composition of sandstone samples was determined by counting 300 grains per thin section using the Gazzi-Dickinson method (Gazzi, 1966; Dickinson, 1970; Ingersoll et al., 1984). Grain types were identified and tabulated separately through point-counting analysis, following the conventions of Ingersoll et al. (1984) and Dickinson (1985). We have summed our detrital modes, through recalculation and normalization, into grain categories that are widely used for purposes of comparative petrology (see Rumelhart, 1998 for details). These are framework-grain assemblages (QmFLt), framework mineral grains (QmKP), and framework lithic grains (LmLvLs and QpLvLsm) (see Table

Figure 17. (Continued.)

A Xishuigou section

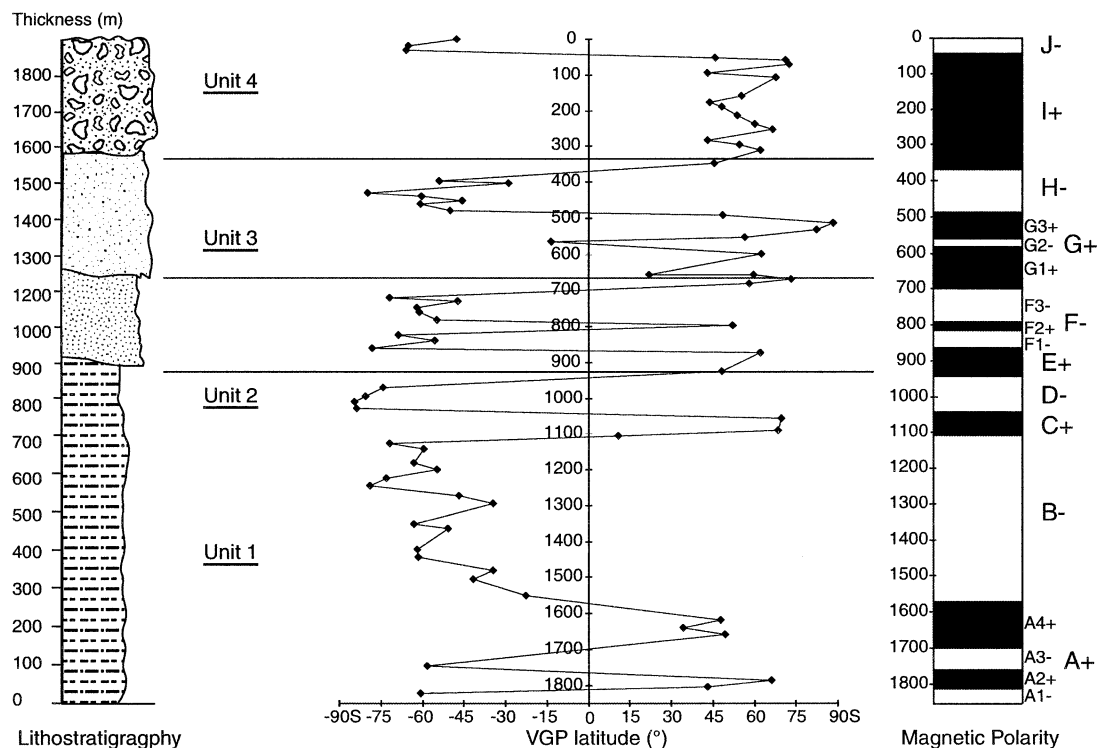


Figure 18. (A) Latitude of virtual geomagnetic poles (VGPs) and polarity stratigraphy for the Xishuigou section. (B) Magnetostratigraphic correlation of Xishuigou polarity sequence to GPTS. Symbols as in Figure 14. Preferred correlation is indicated by *; see discussion in text.

2 for definition of the symbols). We did not use the QtFL data in the analysis because Qp grains are generally in such low abundance that the QmFLt plots differ little from the QtFL plots. The QmFLt plots are preferred here because of their emphasis of provenance over grain stability (Dickinson, 1985).

Aertashi

Twenty-six samples were analyzed from the Aertashi section (Table 2; Fig. 19). Overall, these samples are quartzolithic arenites (QmFLt = 58, 14, 28; Pettijohn et al., 1987) and dominated by monocrystalline quartz

grains (i.e., Qm = 80, K = 12, P = 8). Among the framework lithic grains (Qp-LvmLsm and LmLvLs), carbonate (Lsc) and metasedimentary (Lms) grains predominate, with subordinate amounts of volcanic (Lv) and metavolcanic (Lmv) grains. Very low amounts of polycrystalline quartz (Qp) grains

TABLE 2A. GRAIN CATEGORY DEFINITIONS AND RECALCULATED PARAMETERS

Grain category definitions		Categories after Ingersoll et al., (1984)	Recalculated parameters	
Qp	Aphanitic polycrystalline quartz	→	Qp	QmFLt:
Qm	Monocrystalline quartz	→	Qm	Qm = Qm
P	Plagioclase feldspar	→	P	F = P + K
K	Potassium feldspar	→	K	Lt = Lv + Lm + Ls + Qp
Lv	Volcanic lithic fragments	→	Lv	
Lmv	Metavolcanic lithic fragments	→	Lmv	QtFL:
PxM	Polycrystalline phyllosilicates	→	Lms	Qt = Qm + Qp
QMFA	Quartz-mica-feldspar aggregate	→	Lms	F = P + K
QMFT	Quartz-mica-feldspar tectonite	→	Lms	L = Lv + Lm + Ls
Lss	Argillaceous sedimentary lithic fragments	→	Ls	
Lsc	Aphanitic carbonate lithic fragments	→	Ls	LmLvLs:
M	Monocrystalline phyllosilicates	→	M	Lm = Lm
D	"Dense" mineral grains	→	D	Lv = Lv
Misc	Unidentified	→	Misc.	Ls = Ls
Cmt	Matrix and cement (interstitial) (Not a grain category)	→	I	
Lm	Metamorphic lithic fragments	→	Lm	QpLvmLsm:
				Qp = Qp
				Lvm = Lv + Lmv
				Lsm = Ls + Lms
				QmKP:
				Qm = Qm
				K = K
				P = P
				Ratio Parameter:
				P/F
				Lmv/Lm
				%M = (M/(Q + F + L + M + D)) × 100
				%D = (D/(Q + F + L + M + D)) × 100

B Xishuigou

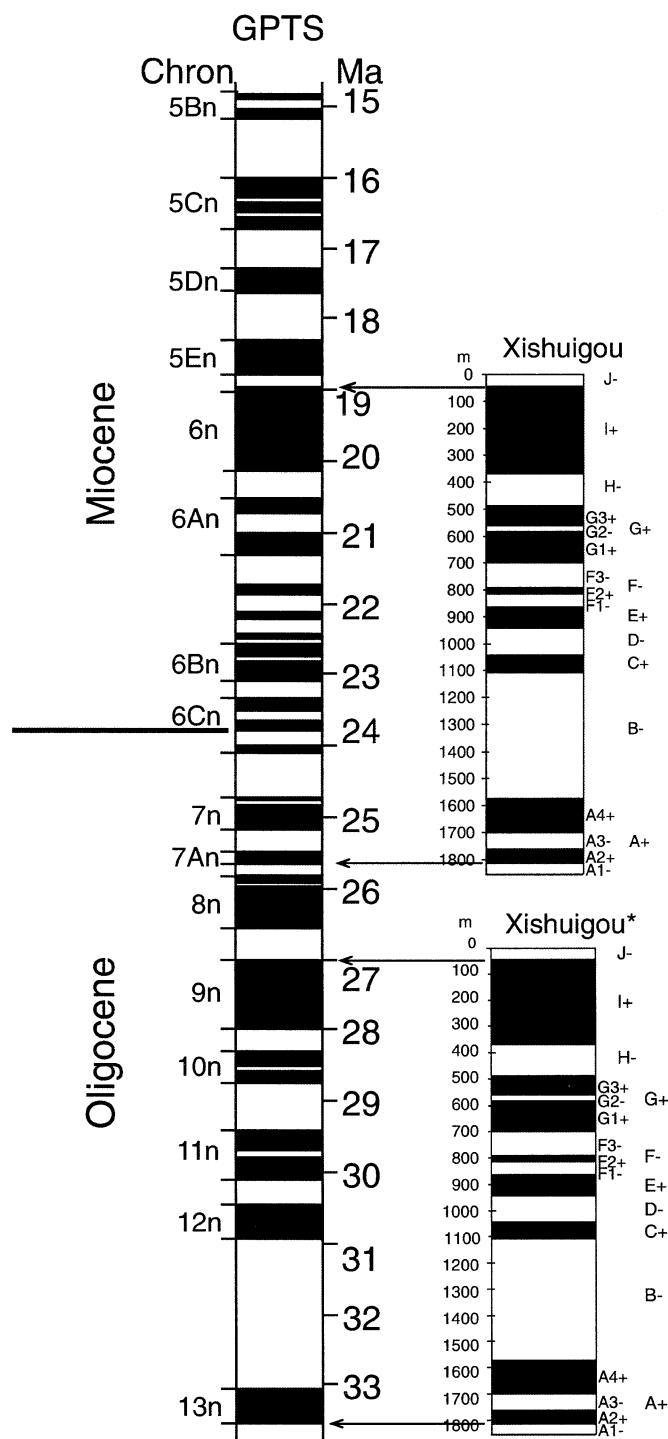


Figure 18. (Continued.)

indicate the scarcity of chert within the source area. Our observed modal composition of Oligocene sandstone is similar to that of Middle Jurassic to Paleogene strata studied in the Aertashi area by Sobel (1995, 1999), suggesting

that the source region has not changed substantially since Middle Jurassic time. However, the two uppermost samples directly above our measured section (i.e., unit 5 in Fig. 6) show significant changes in modal com-

position. These changes are expressed by a dramatic increase in lithic percentage QmFL%L (23%–55%) at the expense of quartz, associated with a marked increase in LmLvLs%Lv (13%–23%), and an increase in $P/(P + K) = P/F$ from 0.41–0.65 (P = plagioclase, K = potassium feldspar, F = total feldspar). Such a rapid increase in lithic component may have resulted from initiation of a new thrust fault in the foreland. As a result, alluvial sediments of a proximal facies were shed from a source closer to the location of the measured section. Because unit 5 in Figure 6 lies directly above our magnetostratigraphic section (Fig. 13B), movement along the inferred new thrust front in the western Kunlun foreland must have been initiated after ca. 24 Ma.

Puska

Forty-five samples were analyzed for the Puska section (Table 2, Fig. 19). Sandstone samples are generally quartzolithic arenites (Qm = 58, F = 12, Lt = 30) with significantly more plagioclase (P) than potassium feldspar (K) (i.e., $P/F = 0.70$, where $F = P + K$). The section may be divided into four petrofacies from bottom to the top (P1–P4, see Table 2). The lowest petrofacies (P1) is characterized by relatively high Qm and low F (Qm = 70, F = 6, Lt = 24) and very high sedimentary lithic fragments (Lm = 16, Lv = 8, Ls = 76) dominated by carbonate fragments. Petrofacies P2 is characterized by moderate amounts of Qm and F (Qm = 59, F = 12, Lt = 29), low sedimentary lithics (Lm = 62, Lv = 16, Ls = 22) and moderate meta-volcanic (Lmv) grains (Qp = 9, Lmv = 31, Lms = 60). Petrofacies P3 is characterized by subequal amounts of metasedimentary (Lms) and carbonate (Lsc) grains (Lm = 48, Lv = 11, Ls = 41; Qp = 6, Lvm = 22, Lsm = 72). P3 also has the highest proportion of lithic fragments of any of the petrofacies (Qm = 52, F = 10, Lt = 38). Petrofacies P4 is characterized by high proportions of sedimentary (mostly Lsc) and metasedimentary lithics (Qp = 1, Lvm = 14, Lsm = 85) and high monocrySTALLINE phyllosilicate grains (M = 5%–11% of framework grains). This description suggests that, from the bottom to the top of the section, the sandstone compositions exhibit a steady decrease in monocrySTALLINE quartz grains (Qm) and an increase in lithic fragments (L). We relate this observation to progressive unroofing of the western Kunlun Shan in late Eocene time, as the Carboniferous–Permian shallow-marine strata were eroded away to expose early Paleozoic metamorphic and plutonic rocks that lie unconformably be-

TABLE 2B. SANDSTONE POINT-COUNT DATA

Sample number	Depth (m)	Qm	Qp	K	P	QMfA	QMfT	PxM	Lmv	Lv	Lss	Lsc	M	D	Misc	Cmt	Total	Notes	
<u>Aertashi section</u>																			
ART01	10	136	6	19	24	12	13	0	42	6	2	31	9	0	0	13	313	Calcite cement	
ART02	294	199	6	40	16	6	2	0	12	7	0	11	1	0	0	112	412	Calcite cement	
ART03	441	172	14	45	10	6	4	1	11	7	2	28	0	0	0	40	340	Calcite cement	
ART04	553	192	12	39	23	1	4	2	13	6	1	7	0	0	0	19	319	Calcite cement	
ART05	564	179	12	36	20	6	4	0	10	10	4	17	2	0	0	18	318	Calcite cement	
ART06	628	189	10	48	7	5	1	0	12	6	1	18	3	0	0	37	337	Calcite cement	
ART07	713	183	10	30	19	6	3	1	11	4	2	31	0	0	0	46	346	Calcite cement	
ART08	753	191	13	25	17	7	3	1	10	10	2	20	1	0	0	35	335	Calcite cement	
ART09	817	181	24	21	13	14	2	0	4	8	4	29	0	0	0	26	326	Calcite cement	
ART10	892	175	16	25	13	11	2	0	14	10	1	32	1	0	0	56	356	Calcite cement	
ART11	943	172	17	21	14	5	1	1	17	12	5	32	3	0	0	17	317	Calcite cement	
ART12	982	164	14	19	12	9	6	0	8	5	6	55	2	0	0	42	342	Calcite cement	
ART13	994	182	13	10	23	4	3	0	14	8	4	38	1	0	0	38	338	Calcite cement	
ART14	1106	167	17	27	13	8	10	0	8	12	5	32	1	0	0	39	339	Calcite cement	
ART15	1170	175	22	20	14	5	8	1	16	9	3	24	3	0	0	24	324	Calcite cement	
ART16	1245	191	11	16	8	10	9	1	14	13	1	24	2	0	0	22	322	Calcite cement	
ART18	1362	172	7	11	28	7	11	0	15	2	6	37	4	0	0	41	341	Calcite cement	
ART19	1514	188	6	21	15	8	11	0	16	3	7	21	4	0	0	37	337	Calcite cement	
ART20	1626	206	12	15	10	6	0	0	13	9	0	29	0	0	0	89	389	Calcite cement	
ART21	1694	66	11	9	4	3	1	0	1	2	20	183	0	0	0	35	335	Calcite cement	
ART22	1770	166	11	25	14	12	10	0	17	8	2	30	5	1	0	59	360	Calcite cement	
ART23	1854	170	5	32	30	6	5	1	10	16	2	17	5	1	0	50	350	Calcite cement	
ART24	?	171	2	18	15	12	8	0	14	8	6	40	4	2	0	82	382	Calcite cement	
ART25	?	174	8	34	8	10	2	0	6	9	4	45	0	0	0	49	349	Calcite cement	
<u>Puska section</u>																			
96P01	0	207	6	5	30	10	2	0	1	9	13	30	0	0	0	10	323	Calcite cement	
96P02	21	213	5	10	18	6	0	0	6	4	1	38	0	1	0	14	316	Calcite cement	
96P03	36	202	6	1	18	8	1	0	2	5	0	57	0	1	0	16	317	Calcite cement, sphene	
96P04	93	218	3	0	10	3	1	0	4	0	1	61	0	1	0	0	302		
96P05	262	208	10	0	1	4	0	0	3	7	0	67	0	0	0	26	326	Calcite cement	
96P08	330	144	6	2	38	21	1	0	2	9	0	75	2	2	0	30	332	Calcite cement	
96P09	338	120	6	34	23	18	1	0	24	53	2	16	3	0	0	0	300	Garnet	
96P10	353	122	2	30	28	41	2	0	31	33	6	5	0	0	0	30	330	Calcite cement	
96P11	432	214	4	25	12	13	0	1	3	4	0	23	2	2	0	29	332	Calcite cement	
96P12	442	215	3	18	32	15	1	0	5	5	1	4	1	4	0	89	393	Calcite, zeolite cement; garnet	
96P13	468	183	3	17	52	35	3	0	3	3	0	1	0	0	0	125	425	Zeolite cement	
96P15	545	162	6	3	12	31	10	0	42	13	0	12	10	1	0	18	320	Calcite cement	
96P16	580	197	6	6	27	34	7	0	7	8	0	6	2	1	0	9	310	Calcite cement	
96P17	588	201	12	5	27	19	2	0	7	5	0	21	1	0	0	6	306	Calcite cement	
96P18	660	182	2	8	31	30	7	0	12	15	0	11	2	0	0	22	322	Calcite cement	
96P19	741	204	7	13	13	26	3	0	6	18	1	7	2	0	0	10	310	Calcite cement	
96P20	797	191	14	17	13	33	3	0	9	11	1	8	0	1	0	7	308	Calcite cement	
96P21	866	184	10	3	25	28	5	0	20	14	0	11	0	1	0	6	307	Hematite cement	
96P22	912	150	4	7	15	41	15	3	25	4	2	18	16	3	0	14	317	Calcite cement	
96P23	?	187	7	0	11	37	10	1	20	7	0	15	0	1	0	15	311	Calcite cement	
96P34	?	166	14	66	2	6	2	0	6	6	0	11	6	6	0	47	338	Calcite cement	
96P33	?	167	7	63	3	28	3	0	0	4	8	9	8	0	3	26	329	Calcite cement	
96P32	?	154	2	3	20	34	13	11	21	23	0	12	0	1	2	30	326	Calcite cement	
96P31	?	179	2	9	28	24	6	1	9	18	1	18	7	0	2	32	336	Calcite cement	
96P25	?	190	7	5	17	24	5	0	22	20	0	6	4	0	1	18	319	Calcite cement	
96P24	?	176	4	9	26	26	3	0	24	15	2	13	2	0	1	26	327	Calcite cement	
96P29	?	184	13	6	28	37	2	0	13	12	0	5	0	0	0	2	302		
96P28	?	188	10	18	15	10	1	0	20	5	1	31	0	0	1	67	367	Calcite cement	
96P27	?	207	5	3	13	21	2	1	16	10	0	18	3	1	0	25	325	Calcite cement	
96P26	?	145	9	7	24	41	25	0	24	8	0	13	4	0	1	18	319	Calcite cement	
96K04B	29.6	154	2	11	24	25	5	0	21	21	0	30	6	1	0	37	337	Calcite cement	
96K13	126	156	4	2	16	33	12	0	9	15	0	45	8	0	4	30	334	Calcite cement	
96K17	170	158	9	4	14	37	13	0	15	5	3	40	2	0	0	20	320	Calcite cement	
96K20	226	168	9	11	14	30	7	0	13	11	0	34	3	0	9	39	348	Calcite cement	
96K21	240	161	5	7	26	39	6	1	16	7	2	25	3	2	2	33	335	Calcite cement, opaques	
96K22	253	166	4	3	17	34	4	0	9	10	0	48	5	0	6	30	336	Calcite cement	
96K23	315	156	9	7	23	18	10	2	15	7	4	42	3	4	0	35	335	Calcite cement, opaques	
96K29	511	146	9	6	23	30	0	0	18	7	5	53	3	0	10	59	369	Calcite cement	
96K30	526	150	10	9	22	29	6	0	13	7	6	45	3	0	1	52	353	Calcite cement	
96K31	537	155	10	7	20	35	5	0	10	11	0	45	2	0	8	51	359	Calcite cement	
96K32	544	135	8	22	15	26	11	0	5	14	2	60	2	0	1	59	360	Calcite cement, opaques	
96K33	553	155	9	25	15	21	7	0	8	20	5	32	2	1	1	35	336	Calcite cement, opaques	
96-28-2.5	?	147	1	25	31	21	16	0	2	5	0	31	19	2	3	13	316	Calcite cement, biotite, muscovite	
96-28-6	?	133	0	15	54	26	5	1	2	1	0	35	22	6	1	18	319	Calcite cement, biotite, muscovite	
96-28-4	?	137	0	14	30	38	13	1	1	6	1	24	31	4	0	16	316	Calcite cement, biotite, muscovite	
96-28-8	?	108	4	12	43	51	13	0	38	5	0	11	15	0	0	0	300		

TABLE 2B. (Continued.)

Sample number	Depth (m)	Qm	Qp	K	P	QMfa	QMft	Pxm	Lmv	Lv	Lss	Lsc	M	D	Misc	Cmt	Total	Notes
<u>Jianglisa section</u>																		
97Q21	?	169	5	11	17	29	4	7	15	32	0	12	6	0	0	32	339	Calcite cement, garnet
97Q22	?	171	0	14	8	31	0	0	11	28	0	25	11	3	0	67	369	Calcite cement
97Q23	?	100	0	33	59	13	4	5	13	4	0	44	22	14	0	34	345	Calcite cement, biotite, garnet, hornblende
97Q01	0	185	12	16	8	28	4	0	0	2	0	1	44	4	0	17	321	Calcite, silica, zeolite cement; sphene; biotite; muscovite
97Q02	34	182	11	22	20	22	10	2	2	4	0	19	8	3	0	44	349	Calcite cement, biotite, muscovite, garnet; gneisses; igneous
97Q05	229	221	8	9	10	11	1	0	18	19	3	1	2	1	0	12	316	Gneisses, igneous fragment
97Q07	278	149	5	11	24	33	7	9	5	23	0	11	23	0	0	81	381	Calcite, zeolite cement; biotite; muscovite
97Q08	379	165	1	31	18	24	9	1	19	20	0	4	4	0	0	42	338	Calcite cement
97Q09	421	163	3	8	17	12	2	0	14	33	0	38	10	4	0	61	365	Calcite cement
97Q10A	674	210	9	13	31	13	4	0	7	15	2	1	2	2	0	11	320	Gneisses, igneous fragment
97Q10B	674	175	2	38	19	19	3	3	4	31	0	3	6	0	0	28	331	Calcite cement
97Q11	890	219	2	26	8	14	0	3	9	7	0	14	1	0	0	34	337	Calcite cement
97Q12	939	212	8	19	10	11	1	1	8	29	0	2	0	0	0	11	312	
97Q13A	970	228	6	26	8	4	3	0	1	24	0	0	0	1	0	11	312	
97Q13B	970	209	7	24	11	13	0	4	8	17	0	8	3	4	0	57	365	Calcite cement
97Q14	1092	178	3	50	21	14	1	6	7	19	0	5	2	4	0	44	354	Calcite cement, garnet
97Q16	1196	190	5	24	23	9	4	0	5	15	0	23	2	3	0	118	421	Calcite cement
97Q18	1348	104	0	20	34	42	2	11	14	0	0	51	33	9	0	34	354	Calcite cement, garnet, biotite, muscovite
97Q19	1561	165	2	13	36	26	1	4	16	16	0	14	11	4	0	37	345	Calcite cement
<u>Subei section</u>																		
XSG02	?	86	3	37	102	18	11	3	15	3	3	5	10	8	0	70	374	Calcite cement, biotite, hornblende, igneous rock fragments
XSG04	?	83	0	38	121	9	11	0	14	1	1	1	11	9	2	90	391	Calcite, chlorite cement; hornblende; zirc; biotite
XSG05	?	75	0	48	143	0	4	4	4	5	1	0	12	4	0	85	385	Calcite, zeolite, hematite, chlorite cement; epidote
XSG06	?	69	0	37	95	10	38	4	16	1	3	0	23	4	15	8	323	Hornblende, epidote
XSG07	?	137	0	76	63	1	5	0	3	2	0	1	3	9	0	73	373	Calcite cement
XSG08	?	79	1	48	112	10	13	2	16	3	0	1	11	4	0	108	408	Calcite, zeolite cement; epidote
XSG09	?	106	1	42	101	9	8	1	9	2	0	0	12	9	0	50	350	Sphene, epidote
XSG10	?	68	0	34	111	8	41	0	20	1	0	0	11	6	0	69	369	Calcite cement, hornblende
XSG16	?	73	0	23	114	4	41	3	24	2	2	0	6	8	0	40	340	Hornblende
XSG17	?	88	1	59	88	14	59	4	32	1	1	0	15	9	0	102	473	Calcite cement, hornblende, biotite, muscovite, chlorite
XSG19	1890	73	0	51	126	4	12	0	5	0	1	0	20	8	0	112	412	Calcite cement, apatite, plutonic rock fragments
XSG19B	1890	78	1	53	120	8	10	0	16	0	0	0	11	3	0	85	385	Calcite cement
XSG20	1858	90	0	19	94	15	29	5	21	1	0	0	13	13	0	10	310	Sphene, epidote, hornblende
XSG21	1838	74	1	11	97	17	45	4	27	3	4	0	12	5	0	35	335	Hematite, calcite cement; epidote; hornblende
XSG22	1838	94	1	11	54	9	44	3	70	2	1	0	4	7	0	35	335	Calcite cement, epidote
XSG25	1797	136	1	34	66	4	14	0	28	0	0	0	11	6	0	24	324	Clinozoisite
XSG26	1782	115	0	32	107	9	9	0	8	5	0	0	8	7	0	29	329	Zeolite cement
XSG28	1676	111	0	53	90	11	5	1	16	0	3	0	7	3	0	30	330	Zeolite cement
XSG28	1676	94	3	54	102	2	3	2	28	0	2	0	7	3	0	60	360	Calcite, zeolite, chlorite cement
XSG29	1651	132	0	37	78	12	8	3	6	4	3	0	13	4	0	36	336	Calcite, chlorite cement; muscovite
XSG31	1605	96	0	12	67	27	39	5	24	6	4	0	8	13	0	35	336	Zeolite, hematite cement; hornblende; sphene
XSG33A	1516	100	2	41	86	11	12	0	9	1	1	1	23	13	4	71	375	Calcite, chlorite, zeolite cement; hornblende; sphene
XSG33B	1516	103	0	36	103	6	7	6	21	2	2	0	6	8	0	54	354	Calcite cement, garnet
XSG34	1494	128	0	38	73	15	11	0	7	5	4	2	10	7	4	82	386	Calcite, chlorite, zeolite cement; hornblende
XSG36	1459	77	3	35	103	8	30	5	24	0	6	4	6	1	0	92	394	Calcite, zeolite, chlorite, hematite cement
XSG37	1399	83	1	9	46	36	86	4	17	2	0	0	12	4	6	60	366	Calcite, zeolite, hematite cement
XSG42	1269	62	1	14	52	13	29	1	28	0	1	0	8	7	0	120	336	Apatite
XSG45	1198	127	2	22	78	15	22	1	10	0	3	3	15	2	0	80	380	Calcite, zeolite cement
XSG46	1188	104	0	34	80	13	31	2	8	3	2	1	14	8	8	32	340	Chlorite, zeolite, calcite cement
XSG47	1171	55	2	41	134	3	26	2	17	0	3	0	10	7	0	65	365	Calcite cement, sphene
XSG48	1131	107	0	30	75	15	28	5	23	2	1	0	10	3	5	138	442	Calcite, zeolite cement; hornblende
XSG49	1131	121	0	16	61	11	35	1	18	6	17	2	5	6	0	73	372	Calcite, cement, apatite, epidote
XSG52	1030	109	0	31	103	14	16	1	11	1	1	2	9	2	0	28	328	Calcite chlorite, zeolite cement
XSG53	1017	95	0	35	73	11	33	3	35	1	1	0	9	5	0	61	362	Calcite, zeolite cement
XSG54	936	79	1	18	64	14	37	7	48	2	1	0	8	22	0	47	348	Calcite cement, epidote, igneous rocks
XSG55	919	95	0	29	92	17	32	1	9	2	3	0	13	7	1	9	310	Chlorite, zeolite cement
XSG56	860	83	0	24	102	13	36	0	16	1	2	0	13	10	5	18	323	Chlorite, zeolite cement; epidote; sphene
XSG57	835	105	1	24	89	11	19	0	30	2	2	1	8	8	11	27	338	Chlorite, zeolite, calcite cement
XSG59	786	85	0	39	104	7	5	3	50	2	0	0	2	3	0	14	314	Calcite cement, very large Lmv
XSG60	748	63	2	23	112	3	37	4	31	0	3	1	9	13	0	100	401	Calcite cement
XSG61	707	117	0	33	58	10	14	9	28	2	17	3	8	1	0	0	300	
XSG62	665	84	1	34	101	11	17	4	28	2	3	1	8	9	0	18	321	Zeolite/calcite cement
XSG63	617	112	4	22	83	12	26	2	23	2	4	0	7	3	0	80	380	Calcite cement, sphene, epidote
XSG64	595	148	1	10	53	25	15	0	31	5	5	1	5	2	3	37	341	Calcite cement
XSG66	467	91	1	5	119	7	29	3	31	0	0	0	6	8	0	135	435	Calcite, zeolite, chlorite, hematite cement
XSG67	363	93	0	24	64	11	35	5	51	1	3	0	10	3	0	23	323	Zeolite/calcite cement
XSG68	291	92	1	43	77	13	11	3	31	0	7	0	19	3	2	80	382	Fine- to medium-grained calcite cement, epidote, sphene
XSG69	143	66	0	20	74	12	39	8	62	1	3	0	6	9	0	0	300	
XSG70	124	60	0	20	83	14	33	1	71	1	1	0	5	11	0	60	360	Epidote
XSG72	67	82	0	20	75	6	37	4	52	0	1	0	12	11	0	32	332	Calcite cement, apatite, hornblende, mudstone

Note: for abbreviations, see Table 2A.

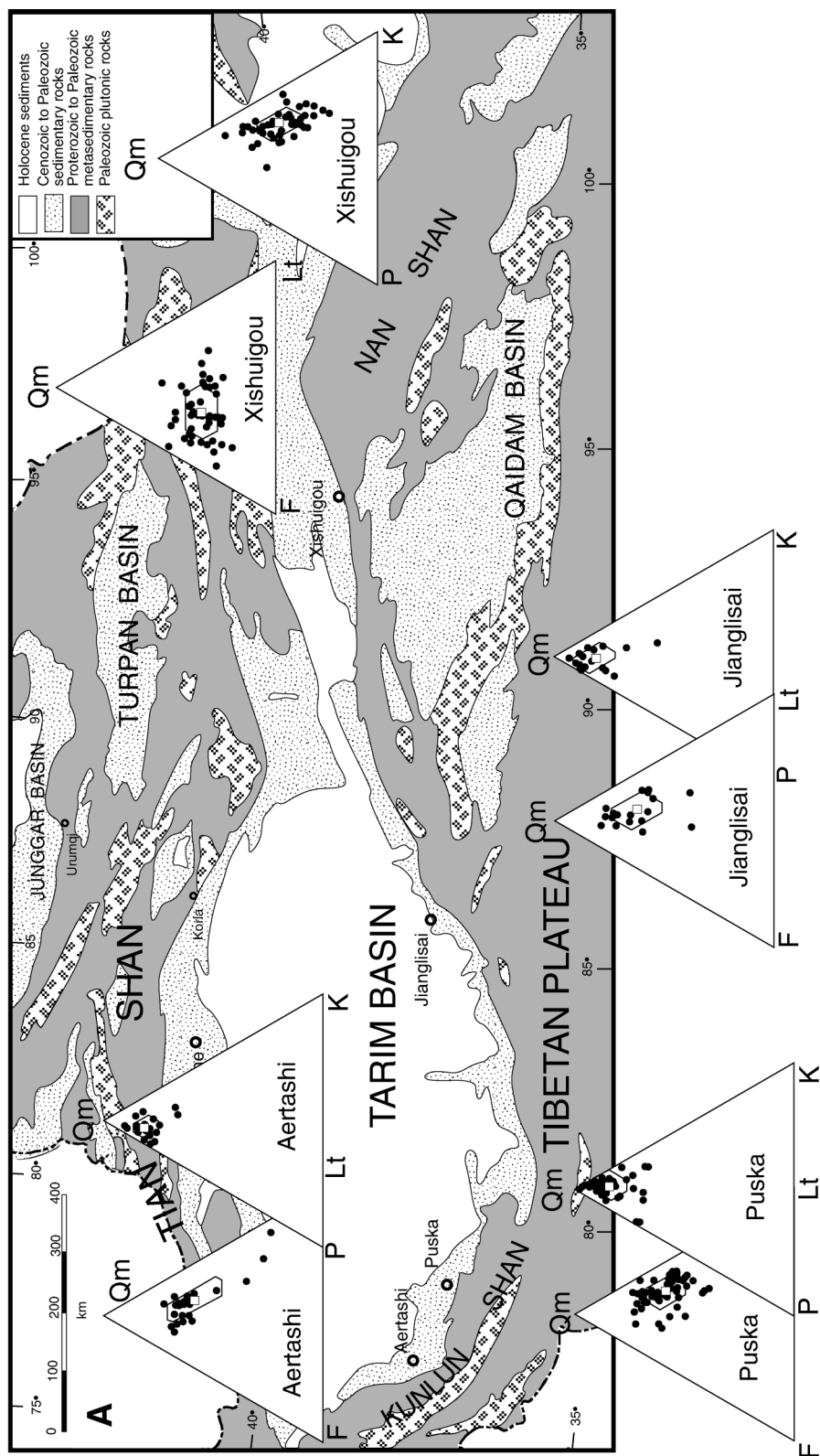


Figure 19. (A) QmFLt and QmKP ternary plots of Tertiary sandstone compositional data for all the measured sections. Dark circles are individual samples, white squares are section means, and hexagons are the standard deviations from the mean. (B) LmLvLs and QpLvLsm ternary plots of Tertiary sandstone compositional data for all the measured sections. Dark circles are individual samples, white squares are section means, and hexagons are the standard deviations from the mean.

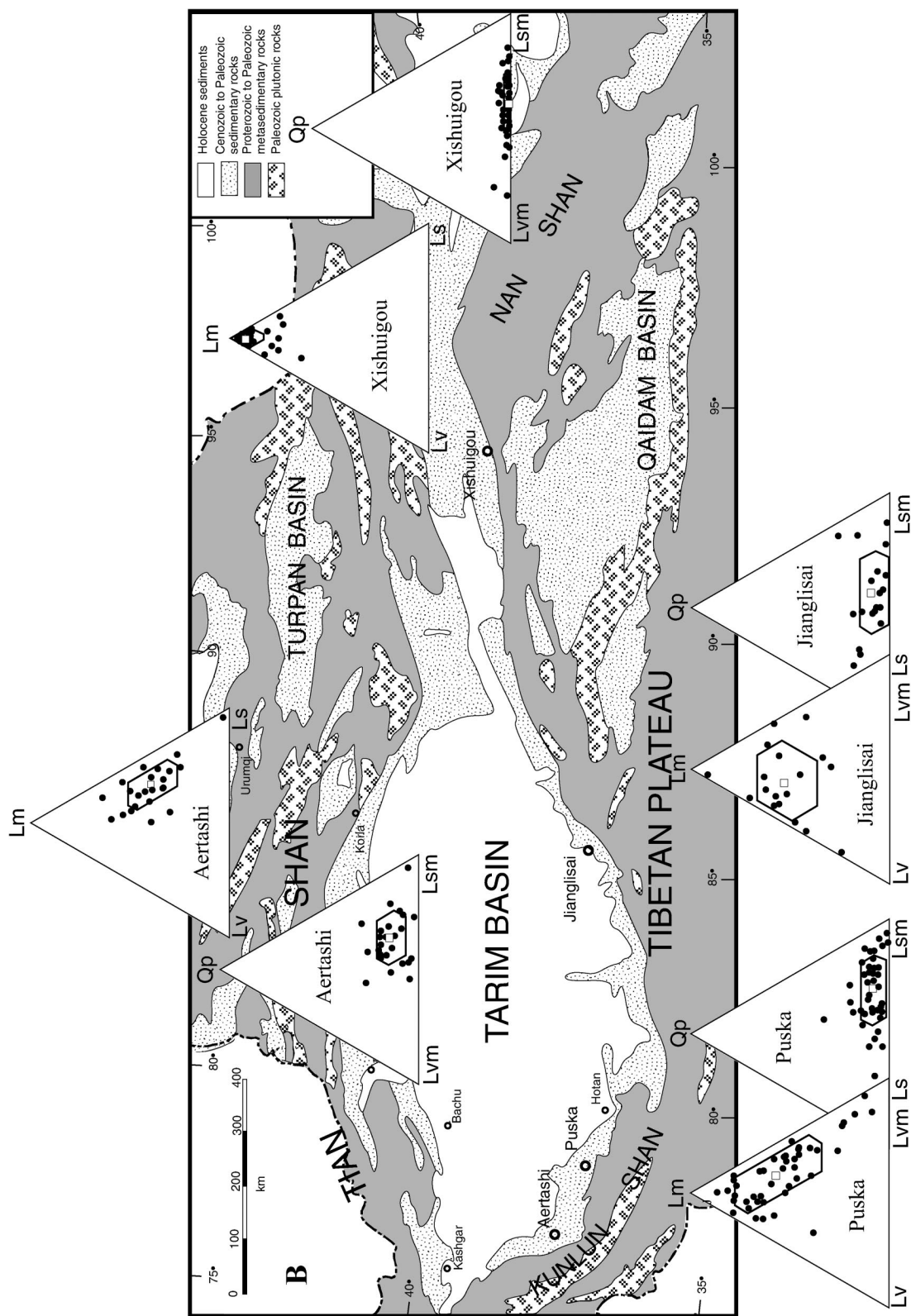


Figure 19. (Continued.)

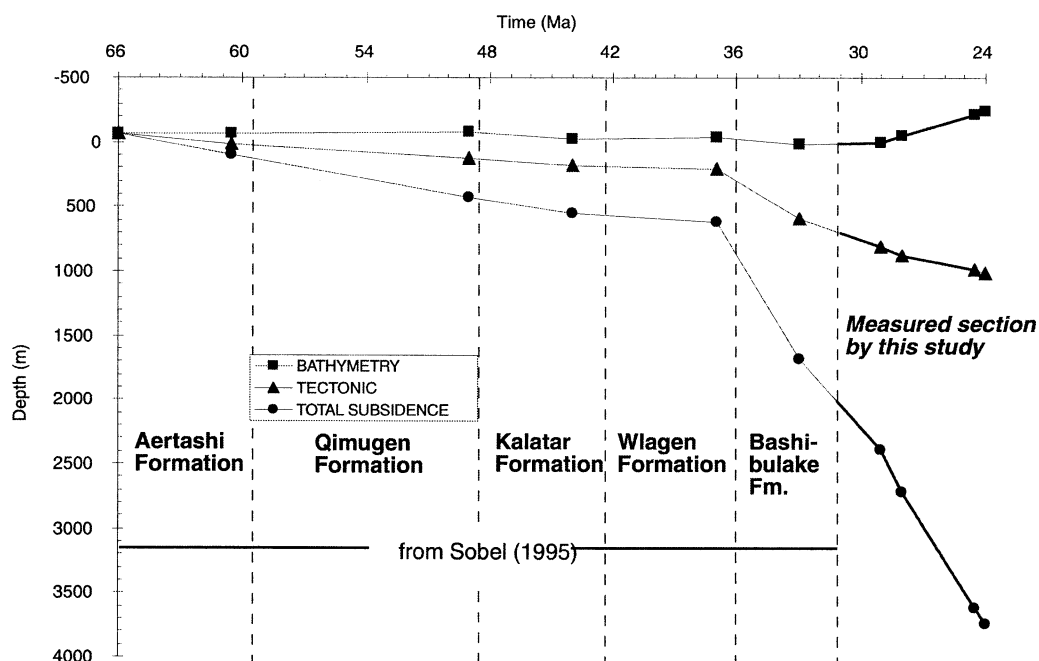


Figure 20. Subsidence curve of the Aertashi section. Note that rapid tectonic subsidence began at ca. 37 Ma at the beginning of deposition for the Bashibulake Formation.

low (Xinjiang BGMR, 1993). This observation suggests that the western Kunlun thrust system was already in existence during the deposition of the Puska section, causing uplift and denudation of the western Kunlun Shan and shedding sediments to the foreland basin.

Jianglisai

Nineteen samples were analyzed from Cretaceous and Cenozoic strata exposed at Jianglisai (Fig. 19, Table 2). Overall, the samples are quartzolithic arenites ($Q_m = 62$, $F = 4$, $L_t = 24$), with about equal amounts of plagioclase (P) and potassium feldspar (K) ($Q_m = 81$, $K = 10$, $P = 9$). The Jianglisai section is characterized by relatively low carbonate (Lsc) and high volcanic (Lv) grains ($L_m = 52$, $L_v = 29$, $L_s = 19$). However, the samples from the uppermost part of the section (Table 2) show much higher amounts of carbonate lithic fragments (Lsc) up to 53% ($L_m - L_v L_s \% L_s$). The metamorphic grains are mostly metasedimentary fragments (Lms) with some tectonites and metavolcanic (Lmv) grains ($Q_p = 8$, $L_{vm} = 39$, $L_{sm} = 53$). The variation of petrofacies from volcanic-clast-dominated lithics to an increasing amount of carbonate lithics may have resulted from sequential unroofing of the Altyn Tagh Range. That is, the volcanic lithics were derived from the Paleozoic volcanic arc complexes that built on top of a Proterozoic passive continental-

margin sequence dominated by thick carbonate strata (Liu, 1988; Xinjiang BGMR, 1993).

Xishuigou

Forty-six samples were analyzed from the Xishuigou section in the Subei area (Fig. 19, Table 2). Sandstone samples are generally lithofeldspathic arenites ($Q_m = 33$, $F = 43$, $L_t = 24$). Unlike the other sections, the modal compositions of the Xishuigou sandstones are dominated by plagioclase feldspar ($P/F = 0.75$). This section has the lowest proportion of monocristalline quartz ($Q_m = 44$, $K = 14$, $P = 42$). In terms of the framework lithic grains, the Xishuigou section is characterized by a high percentage of metamorphic (Lm) lithics and an almost total lack of volcanic (Lv) and sedimentary (Ls) grains ($L_m = 91$, $L_v = 4$, $L_s = 5$). The metamorphic lithics are composed of mostly granular and tectonized metasedimentary rocks (Lms), but have a significant amount of highly chloritized metavolcanic (Lmv) grains ($Q_p = 1$, $L_{vm} = 38$, $L_{sm} = 61$). The modal compositions of sandstone are consistent with the hanging-wall lithologies exposed in the Danghe Nan Shan above the Subei thrust (Liu, 1988; Gansu BGMR, 1989). This lithologic correlation suggests that deposition of the Xishuigou section was associated with movement along the Subei

thrust that is geometrically and kinematically linked with the Altyn Tagh fault.

TIMING OF DEFORMATION IN NORTHERN TIBET

Subsidence Analysis

Sobel (1995) conducted subsidence analysis of Jurassic to Paleogene strata in the western Kunlun Shan by using both his own measured sections and published Chinese stratigraphic data. One of his analyzed sections is at Aertashi and shows a brief but rapid increase in tectonic subsidence at the initial deposition of the Paleocene Aertashi Formation (ca. 66 Ma). Because the marine basin during Aertashi deposition expanded in the western Tarim Basin at the time when the global sea level was relatively low, Sobel (1995) concluded that tectonic loading in the western Kunlun Shan may have started in the early Paleocene caused by Indo-Asian collision. Although Sobel's (1995) analysis also indicates a rapid increase in subsidence in the late Eocene, no specific tectonic significance was assigned for this event. We expand Sobel (1995)'s analysis by including the section we measured above the Bashibulake Formation (Fig. 20). To be consistent, we also adopted the BasinWorks software package (Marco Polo Software, Inc., 1988–1991) used by Sobel (1995) in our analysis. The stratigraphic thickness and lithology were tak-

en from our measured section. Subdivision within the section was defined on the basis of lithostratigraphic units, each of which was assigned a gross lithology and a compaction coefficient. The depth versus porosity relationship used in the analysis was from Bond and Kominz (1984) and Dickinson et al. (1987). In our age assignment, we assumed that terrestrial deposition at Aertashi began at 32 Ma and that the associated surface uplift above sea level has increased linearly with time since 32 Ma. There are no constraints on the amount of error introduced by this assumption. Post-24 Ma strata above our measured section have poorly defined ages and thicknesses and thus are not included in the analysis. The tectonic-subsidence curve indicates that our measured section represents part of a sequence laid down during rapid subsidence that began at ca. 37 Ma at the start of the Bashibulake deposition (Fig. 20). The increased subsidence recorded in the Aertashi section after 37 Ma lasted much longer (>10 m.y.) and had a larger magnitude (total subsidence >2–3 km) than the subsidence event at ca. 66 Ma (~5 m.y. duration and a total subsidence of <500 m; see Sobel, 1995). Therefore, we suggest that movement of the frontal part of the western Kunlun thrust belt began at ca. 37 Ma. However, contractional deformation could have started much earlier in the interior of the western Kunlun Shan. The brief 66 Ma subsidence event documented by Sobel (1995) in the Kunlun foreland may have been associated with the development of the south-directed Tianshuihai thrust belt, which lies at the western end of the Altyn Tagh fault and may have accommodated >400 km of north-south shortening due to motion along the Altyn Tagh fault (Cowgill, 2001). This thrust belt deforms Upper Cretaceous marine strata that are widespread in western Tibet (Xinjiang BGMR, 1993). Thus, its development must have occurred in the Cenozoic. This thrust belt is currently inactive, but its upper-age bound is unknown.

Facies Analysis

Although the appearance of conglomerate in a foreland sequence is a classical indicator of thrust-belt initiation (e.g., Jordan et al., 1988), other alternatives should also be considered. First, during the rapid movements of early thrust-belt development, fine-grained sediments were deposited in the foreland basin. Only when thrust motion became relatively slow or completely terminated did the coarse sediment flux catch up with subsidence (e.g., Heller et al., 1988; Frostick and Steel,

1993). In this case, coarse-grained sedimentation only provides an upper-age bound for thrust initiation. Second, as the thrust-belt front migrated gradually toward the foreland, the time of vertical juxtaposition of the proximal (coarse-grained) over the distal (fine-grained) facies in the foreland basin must have been diachronous, and the facies boundaries must have dipped toward the thrust front (e.g., Schlunegger et al., 1997). Therefore, the early record of such a facies transition that would document the time of thrust initiation may have been buried underneath the long-traveled master thrust (e.g., the Lewis thrust in the North American Cordillera, Yin and Kelty, 1991). This forward migration of lithofacies may leave a false impression that contractional deformation was initiated at a younger age with an accelerated intensity (Fig. 14B; cf. Métiévier et al., 1998).

Climate change may also have induced rapid erosion and therefore deposition of coarse-grained sediments. However, deposition of Tertiary strata in the southern Tarim Basin must have been a result of tectonics because climate-induced increases in sedimentation rates can only fill preexisting basins but provide no mechanisms to create significant accommodation space (e.g., Frostick and Steel, 1993). The presence of >9 km of Cenozoic strata in the southwestern Tarim Basin requires tectonic loading. These strata thicken toward the western Kunlun thrust front (Li et al., 1996), which is inconsistent with climatically driven sedimentation that produces tabular stratal successions thickening away from the thrust front (Burbank et al., 1996).

Two packages of coarse clastic detritus occur in the Aertashi section. Deposition of the lower cobble conglomerate (Aertashi unit 2) began at ca. 29.5 Ma (Fig. 12B), whereas deposition of the upper (>6-km-thick) cobble to boulder conglomerate started at and after ca. 25 Ma (Aertashi units 4 and 5). The older coarse-grained sequence represents a minimum age of initiation for thrust tectonics within the western Kunlun Shan, whereas the younger coarse-grained package probably represents initiation of a new thrust in the foreland closer to the measured section. The first appearance of proximal-facies conglomerate in the Aertashi section at ca. 25 Ma is nearly 12 m.y. after the time of initial rapid subsidence at ca. 37 Ma (Fig. 19). This conclusion highlights the fact that the appearance of conglomerates can be significantly later than the onset of tectonic loading.

Except for one layer of conglomerate and several intervals of sandstone, the Puska section is dominated by fine-grained sedimentation

(Fig. 8). Thus, the 39.5 Ma age for the top of the section is a maximum for the onset of proximal-facies conglomerate deposition (Fig. 14B). Because the fine-grained section in Puska is thick (>900 m) and its sandstone composition records progressive unroofing of the western Kunlun Shan, we interpret that the section records thrusting-induced uplift. This interpretation implies that gravels from the uplifted western Kunlun Shan prograded toward the foreland at a very slow rate. This slow rate may be attributed to the fact that a large marine embayment was present in the footwall of the western Kunlun thrust in the Eocene (Yang et al., 1995). This large standing water may have prevented coarse-grained sediments from entering the distal part of the foreland basin now juxtaposed closely with the thrust front marked by the Shangzhu thrust. The interpretation of thrust-induced uplift together with the estimated 46–39 Ma age of the Puska section determined by both marine fossils and magnetostratigraphy requires that the western Kunlun thrust belt at Puska was initiated at or prior to ca. 46 Ma. Middle Eocene *Ostrea* (*Turkostrea*)-bearing sediments were also identified at Keliyang (Lan and Wei, 1995) and Shangzhu (Norin, 1946; Şenğöb and Okurogullari, 1991) ~60 and 40 km east of Puska, respectively, which could be part of the same foreland basin as studied in Puska.

This initiation age of deformation at Puska is significantly older than that for the Aertashi section ~200 km to the west and implies that the western Kunlun Shan thrust belt started developing diachronously from east to west. As the western Kunlun thrust belt is the termination structure of the Altyn Tagh fault system, the age constraint from Puska implies that movement on the western Altyn Tagh fault was initiated at or prior to ca. 46 Ma.

Although magnetostratigraphic analysis was successful only within the top 500 m of the coarse clastic deposits at Jianglisai, the basal age of the fine-grained section remains undefined. However, if we extrapolate the average sedimentation rate from the top 500 m to the lower 1500-m-thick section, the base of our measured section could be as old as 35 Ma as already discussed. We further interpret that sedimentation of the Jianglisai section was related to the uplift of the Altyn Tagh Range induced by transpression between the Jianglisai fault in the Altyn Tagh fault system.

Although the delta-plain to braided-fluvial transition occurred at ca. 29.5 Ma at Xishuigou (Fig. 17B), the entire section records the uplift history of the Danghe Nan Shan above the Subei thrust starting at ca. 33 Ma because clastic sediments derived

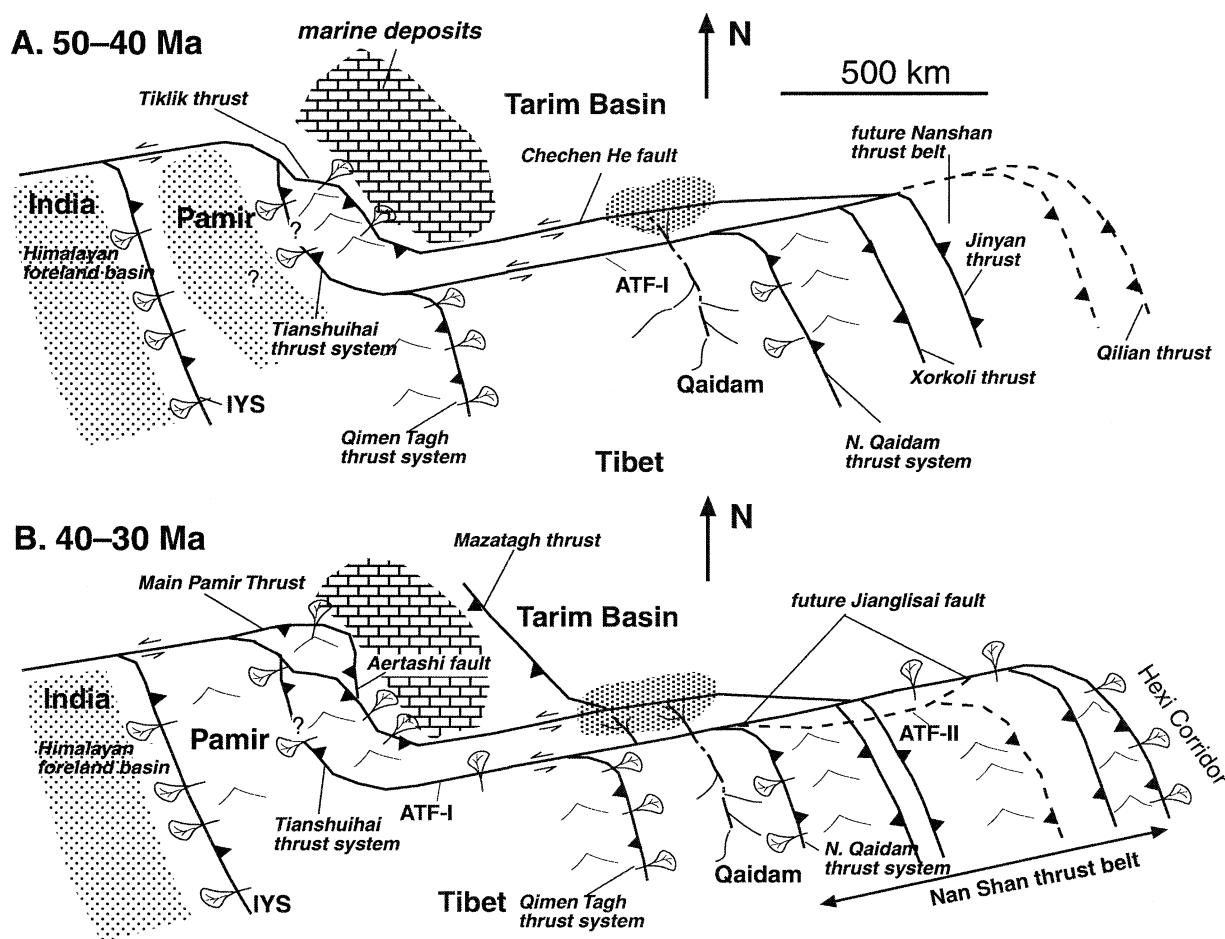


Figure 21. Tectonic history of the Altyn Tagh fault system. In stage 1 (50–40 Ma), the left-slip Altyn Tagh and Chechen He faults together with the western Kunlun, Qimen Tagh, and the North Qaidam thrusts began to develop. Sediments were shed from the north and south into the Qaidam Basin. Major drainage systems may have flowed westward from the Qaidam Basin into the Tarim Basin. During stage 2 (40–30 Ma), movement on the Aertashi fault began, and the Nan Shan thrust belts began to develop. The Jinyan-Xorkoli thrust system in the western Nan Shan is offset to the eastern Altyn Tagh Range by a younger branch of the Altyn Tagh fault (ATF II). The northern branch of the Altyn Tagh fault is the Jianglisai fault, which may have remained active after its offset by the younger Altyn Tagh fault II. The Altyn Tagh Range acted as a moving source, shedding sediments northward into the Tarim Basin and southward into the Qaidam Basin. The southwestward-moving Altyn Tagh Range also acted as a sliding door, blocking the western side of the triangular Qaidam Basin. In stage 4 (20–10 Ma), the current configuration of the Altyn Tagh fault system was established, but continuing contraction across Tibet shortened the overall length of the Altyn Tagh fault. In stage 5 (10–0 Ma), the Altyn Tagh fault lengthened at both ends, creating the Karakash fault in the west and the Kuantai Shan thrust in the east. The right-slip Karakoram fault was also created at this time, assisting eastward extrusion of Tibet.

from the Subei thrust sheet and northward paleocurrent indicators are observed throughout the section. Because the Altyn Tagh fault and the Subei thrust are the same structure, the initiation age of the Subei thrust is older than 33 Ma.

Provenance Analysis

In the western Kunlun Shan and the Altyn Tagh Range, Mesozoic strata, when present, contain little or no carbonate (Liu, 1988; Xinjiang BGMR, 1993). Similarly, the amount of carbonate found in the Paleocene–Eocene strata is too small and too localized to account for the

large quantity of carbonate detritus observed in our measured Aertashi, Puska, and Jianglisai sections. These observations suggest that Paleozoic strata (i.e., Devonian to Permian), which in northern Tibet contain both carbonate and volcanic rocks (e.g., Liu, 1988; Şenö and Okurogullari, 1991; Sobel, 1995; Matte et al., 1996; Pan, 1996), were the primary sources of the measured sections. Exposing and exhumation of the Paleozoic sequences must have started prior to the Late Jurassic because modal compositions of sandstones from Lower Jurassic to Tertiary strata are remarkably similar, as shown by comparing our results with those obtained by Sobel (1995). We speculate that the

initial denudation of the Paleozoic strata occurred in the Late Triassic and Early Jurassic during crustal extension. The importance of extensional tectonics in the Early Jurassic was recently documented in the western Kunlun Shan on the basis of sedimentological arguments (Sobel, 1999). In the eastern Altyn Tagh Range, the Lapeiquan detachment fault was active during the latest Triassic to earliest Jurassic (Fig. 2) (Yin et al., 2000). Documenting Mesozoic extension in the Altyn Tagh Range also explains a widespread Late Triassic–early Jurassic cooling event in northern Tibet (Cowgill, 2001; Sobel et al., 2001). Early Jurassic extensional structures have also been documented in central

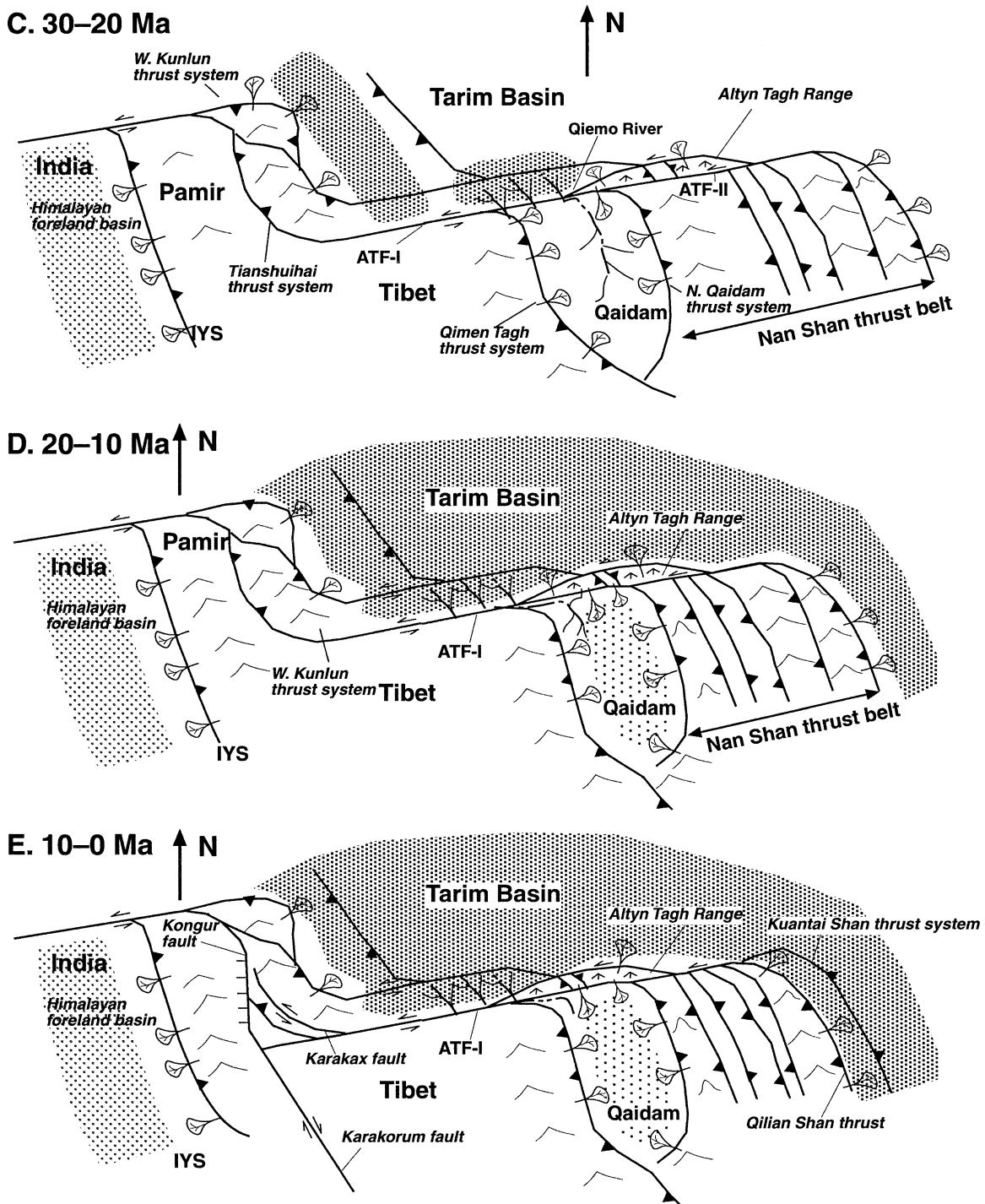


Figure 21. (Continued.)

Tibet (Kapp et al., 2000) and the northern Qilian Shan region (Huo and Tan, 1995). This extensional event in northern Tibet may have been responsible for the observed modal compositions of sandstones in the southern Tarim Basin. Because the sandstones consist of a large amount of unstable lithic grains, we infer that the Tertiary sediments were derived from

nearby drainage divides created by individual thrusts (Schlunegger et al., 1997).

Average Slip Rate Along the Altyn Tagh Fault

The preceding discussion suggests that movement along the western and central Altyn

Tagh fault was initiated at ca. 49 Ma. The total offset along the western Altyn Tagh fault was recently estimated by Cowgill (2001) by correlating Ordovician and Permian plutonic belts across the fault. That study indicates 470 ± 70 km of left-lateral offset along the Altyn Tagh fault. This estimate is consistent with the early estimates of 300–550 km of left-lateral

offset across the western Altyn Tagh fault, determined by comparing geology in the western and eastern Kunlun Shan (Pan, 1984; Peltzer and Tapponnier, 1988). These amounts of offset suggest that the maximum average slip rate on the Altyn Tagh fault is ~ 11 mm/yr, but could be as low as ~ 8 mm/yr. This average slip rate is remarkably similar to the active slip rate of ~ 9 mm/yr determined by the GPS surveys for the Altyn Tagh fault (Bendick et al., 2000; Chen et al., 2000; Z.K. Shen et al., 2001).

TEMPORAL EVOLUTION OF THE ALTYN TAGH FAULT SYSTEM

In the western Kunlun Shan, thrusting was initiated prior to 46 Ma in the southeast (Puska) and at ca. 37 Ma in the northwest (Aertashi). Because the western Kunlun thrust belt is the termination structure of the Altyn Tagh fault system, the westernmost Altyn Tagh fault must have started at or prior to ca. 46 Ma. At Jianglisai, we interpret sedimentation to have been related to transpressional deformation along the left-slip Jianglisai fault of Cowgill et al. (2000). This fault as part of the Altyn Tagh system must have been initiated before 26 Ma and possibly earlier than 35 Ma. Similarly, the Subei thrust and eastern Altyn Tagh fault may have been active since or prior to 33 Ma. In the eastern Altyn Tagh Range north of the central segment of the Altyn Tagh fault, the development of the Xorkoli and Jinyan thrusts was associated with the deposition of a late Eocene–early Oligocene basin (Xinjiang BGMR, 1981). Because the currently active segment of the Altyn Tagh fault cuts the thrusts and the related basin, the left-slip motion along this fault must be younger than early Oligocene time.

The Qaidam Basin is internally drained and is bounded on three sides by tectonically induced uplifted regions. They are the Altyn Tagh Range in the west associated with the Altyn Tagh fault, the Nan Shan in the north associated with the North Qaidam thrust system, and the Qimen Tagh and eastern Kunlun Shan in the south associated with the Qimen Tagh and North Kunlun thrust systems. Previous sedimentologic and biostratigraphic studies suggest that thrust-induced sedimentation in the Qaidam Basin began in the middle Eocene, as indicated by the deposition of the Lulehe Formation (Huo, 1990; Zhang, 1997). This formation characteristically thickens and coarsens toward the North Qaidam and Qimen Tagh thrust fronts, suggesting that the sedimentation was induced by tectonic loading along the north and south edge of the

Qaidam Basin (Huo, 1990; Zhang, 1997). This interpretation suggests that movement along thrusts along the margin of the Qaidam Basin was initiated in the middle Eocene (ca. 49 Ma). Because the counter parts of the Qimen Tagh and North Qaidam thrusts and their associated Eocene sediments are not present north of the Altyn Tagh fault, thrusting along the north and south edges of the Qaidam Basin must have been synchronous with motion on the Altyn Tagh fault. Hanson (1999) showed that the Altyn Tagh Range was already a topographic high region in the Oligocene, shedding sediments into the Qaidam Basin from the northwest. The presence of the Altyn Tagh Range in the Oligocene is consistent with our inferred age of sedimentation for the Jianglisai section. These observations imply that the Altyn Tagh fault system, consisting of the Jianglisai and currently active Altyn Tagh fault, had already been created by the early Oligocene.

George et al. (2001) found that the northeasternmost Nan Shan thrust belt on both sides of the Hexi Corridor began to develop between 20 and 10 Ma. This age is at least 10 m.y. younger than the early Oligocene age for initial proximal-facies sedimentation in the Hexi Corridor as defined by mammal fossils and magnetostratigraphic analysis (Huang et al., 1993). One possible explanation for the discrepancy is that the denudation rate in the Nan Shan foreland is extremely low, causing a time lag between the initiation of thrusting and the recording of its related denudation.

On the basis of the age constraints summarized previously, we propose the following tectonic history for the evolution of the Altyn Tagh fault system (Fig. 21). In stage A (50–40 Ma), the western segment of the Altyn Tagh fault and possibly the Chechen He fault began to develop. Associated with this tectonic event is the development of the north-dipping Tianshuihai and the south-dipping Tiklik thrust systems in the western Kunlun Shan. In addition, thrusts bounding the north and south margin of the Qaidam Basin—the Qimen Tagh and the North Qaidam thrusts—were also developed and shed sediments into the basin from their hanging walls. At this time, the major drainages flowed westward from the Qaidam Basin into the Tarim Basin. During stage B (40–30 Ma), the Aertashi fault (part of the Main Pamir thrust system) began to develop and caused rapid subsidence in Aertashi. The Chechen He fault remained active and initiated the development of the Mazatagh thrust system in the southern Tarim Basin as a branching fault. The Nan Shan thrust belt was developed at this time, shedding sedi-

ments both to the north into the Tarim Basin in the Xishuigou area and to the east into the Hexi Corridor area. The Jinyan-Xorkoli thrust system (now in the eastern Altyn Tagh Range) was originally part of the Nan Shan thrust offset by a younger branch of the Altyn Tagh fault system (= ATF II, Fig. 21). In stage C (30–20 Ma), the Jinyan-Xorkoli thrust system was truncated and offset by the Altyn Tagh fault II, the southern strand of the Altyn Tagh fault system that cuts and offsets a slice of the western Nan Shan thrust belt to the southwest. The northern strand of the Altyn Tagh fault (ATF I = Jianglisai fault) may have remained active and formed a strike-slip duplex with the southern strand (Cowgill et al., 2000). Transpression along the Altyn Tagh system may have further uplifted the Altyn Tagh Range, which acted as a moving source that shed sediments northward into the Tarim Basin and southward into the Qaidam Basin. Continuous southwestward movement of the Altyn Tagh Range acted as a sliding door that eventually closed the western drainage outlets of the Qaidam Basin. Meanwhile, thrusting along the Qimen Tagh and the North Qaidam faults closed the eastern end of the Qaidam Basin, which became internally drained. In stage D (20–10 Ma), the current configuration of the Altyn Tagh fault system was established. Because of continuous shortening in the southwestern Nan Shan thrust belt and around the Qaidam Basin, the overall length of the Altyn Tagh fault decreased since the Miocene due to shortening across Tibet. Since 10 Ma, the Altyn Tagh fault has lengthened both to the west and east, creating the left-slip Karakash fault in the west and the north-dipping Kuantai Shan thrust system in the east. Meanwhile, the right-slip Karakoram fault was also created, which terminates in the north at the Kongur Shan normal fault system.

CONCLUSIONS

1. The uplift of the northern margin of the Tibetan plateau induced by crustal thickening began prior to 46 Ma in the western Kunlun Shan, at ca. 49 Ma around the Qaidam Basin, and prior to ca. 33 Ma in the Nan Shan. Movement along the western Kunlun thrust belt began diachronously, at ca. 46 Ma in the southeast to ca. 37 Ma in the northwest.

2. The western and central Altyn Tagh fault system—consisting of the Chechen He fault, the Jianglisai fault, and the active Altyn Tagh fault itself—started developing at ca. 49 Ma. At its initiation, this left-slip fault system was

linked with the western Kunlun thrust belt and the thrusts bounding the Qaidam Basin as its western and eastern termination structures. The eastern segment of the Altyn Tagh fault developed prior to ca. 33 Ma, but whether movement on it began significantly later than on its central and western segment is unknown.

3. The Altyn Tagh Range has been a topographically high region since at least the beginning of the Oligocene. Its continuous southwestward motion has caused the range to act as a sliding door that eventually closed the westward drainage outlets of the Qaidam Basin.

4. By using the total offset of 470 ± 70 km and our estimated initiation age of 49 Ma, the averaged long-term slip rate along the Altyn Tagh fault is 9 ± 2 mm/yr, remarkably similar to that determined by GPS surveys. This similarity implies that geologic deformation rates have essentially been at steady state over tens of millions of years during continental collision.

5. Modal analysis of Tertiary sandstones provides several important insights into the denudation history of the source region and transport processes of the sediments. First, systematic changes in composition of fine-grained clastic sediments are sensitive indicators for initiation of thrust-induced uplift. Such compositional changes indicate that movement in the western Kunlun thrust belt started prior to 46 Ma despite its dominant fine-grained sedimentation. Second, much of the detrital grains observed from our measured sections were locally derived from the hanging walls of the nearby thrusts or blocks uplifted against transpressional faults; these grains provided a link between sedimentation and tectonic activities. Third, the primary provenance of the measured sections is the Paleozoic volcanic and sedimentary strata exposed along the northern margin of the Tibetan plateau. Because of the lack of detrital clasts from the Mesozoic strata in the Tertiary sections and the similarity of sandstone modal composition between Jurassic–Cretaceous and Tertiary strata, we suggest that a significant denudation event occurred in the Late Triassic and Early Jurassic along the northern margin of the Tibetan plateau. From the regional structural setting, this event was most likely related to widespread extension in northern and central Tibet.

ACKNOWLEDGMENTS

This work was supported by the Continental Dynamics Program of the U.S. National Science Foundation. Fission-track sampling at Jianglisai was sup-

ported by the Stanford China Geosciences Industrial Affiliates Program and grants from the Geological Society of America and the American Association of Petroleum Geologists Grant-in-Aid programs awarded to A. Hanson. We appreciate critical reviews by Ed Sobel, Peter DeCelles, Brad Ritts, and Steward Gilder.

REFERENCES CITED

- Allègre, C.J., Courtillot, V., Tapponnier, P., Hirn, A., Mat-tauer, M., Coulon, C., Jaeger, J.J., Achache, J., Schaer-er, U., Marcoux, J., Burg, J.P., Girardeau, J., Armijo, R., Garipey, C., Goepel, C., Li Tindong, Xiao Xuchang, Chang Chenfa, Li Guanggin, Lin Baoyu, Teng Ji-Wen, Wang Naiwen, Chen Guoming, Han Tonglin, Wang Xibin, Den Wanming, Sheng Huaibin, Cao You-gong, Zhou Ji, Qiu Hongrong, Bao Peisheng, Wang Songchan, Wang Bixiang, Zhou Yaoxiu, and Ronghua Xu, 1984, Structure and evolution of the Himalayan-Tibet orogenic belt: *Nature*, v. 307, p. 17–22.
- Arakel, A.V., 1986, Pedogenic calcretes in the Old Red sandstone facies (Late Silurian–early Carboniferous) of the Anglo-Welsh area, southern Britain, in Chivas, A.R., Torgersen, T., and Bowler, J.M., ed., *Paleosols: Their recognition and interpretation*: Oxford, Blackwell Scientific Publications, p. 58–86.
- Avouac, J.P., and Tapponnier, P., 1993, Kinematic model of active deformation in central Asia: *Geophysical Research Letters*, v. 20, p. 895–898.
- Beer, J.A., 1990, Steady sedimentation and lithologic completeness, Bermejo basin, Argentina: *Journal of Geology*, v. 98, p. 501–517.
- Bendick, R., Bilham, R., Freymueller, J., Larson, K., and Yin, G., 2000, Geodetic evidence for a low slip rate in the Altyn Tagh fault system: *Nature*, v. 404, p. 69–72.
- Bohlin, B., 1942, The fossil mammals from the Tertiary deposit of Taben-Buluk: Part I. Sino-Swedish Expedition: Nanking, Geological Survey of China, Publication 28, 113 p.
- Bohlin, B., 1946, The fossil mammals from the Tertiary deposit of Taben-Buluk, western Kansu, Part II: *Simplidactylata, Carnivora, Artiodactyla, Perissodactyla, and Primates*: Nanking, Geological Survey of China, 259 p.
- Bond, G.C., and Kominz, M.A., 1984, Construction of tectonic subsidence curves for the early Paleozoic miogeocline, southern California: *Geological Society of America Bulletin*, v. 95, p. 155–173.
- Brandon, M.T., 1992, Decomposition of fission-track grain-age distributions: *American Journal of Science*, v. 292, p. 535–564.
- Burbank, D.W., and Reynolds, R.G., 1988, Stratigraphic keys to the timing of thrusting in terrestrial foreland basins: Applications to the northwestern Himalayas, in Kleinspehn, K.L., and Paola, C., eds., *New perspectives in basin analysis*: New York, Springer-Verlag, p. 331–352.
- Burbank, D.W., Beck, R.A., and Mulder, T., 1996, The Himalayan foreland basin, in Yin, A., and Harrison, T.M., eds., *The tectonic evolution of Asia*: Cambridge, Cambridge University Press, p. 149–189.
- Burchfiel, B.C., and Royden, L.H., 1991, Tectonics of Asia 50 yr after the death of Emile Argand: *Eclogae Geologicae Helveticae*, v. 84, p. 599–629.
- Burchfiel, B.C., Quidong, D., Molnar, P., Royden, L., Yipeng, W., Peizhen, Z., and Weiqi, Z., 1989, Intracrustal detachment zones of continental deformation: *Geology*, v. 17, p. 448–452.
- Burmeister, R.F., Bazard, D.R., and Beck, M.E., 1990, Post-folding remagnetization that passes the fold test: *Geophysical Journal International*, v. 102, p. 455–463.
- Cande, S.C., and Kent, D.V., 1992, A new geomagnetic polarity time scale for the Late Cretaceous and Cenozoic: *Journal of Geophysical Research*, v. 97, p. 13,917–13,951.
- Cande, S.C., and Kent, D.V., 1995, Revised calibration of the geomagnetic polarity time scale for the Late Cre-taceous and Cenozoic: *Journal of Geophysical Research*, v. 100, p. 6093–6095.
- Chen, Z., Burchfiel, B.C., Liu, Y., King, R.W., Royden, L.H., Tang, W., Wang, E., Zhao, J., and Zhang, X., 2000, Global Positioning System measurements from eastern Tibet and their implications for India/Eurasia intercontinental deformation: *Journal of Geophysical Research*, v. 105, p. 16,215–16,227.
- Cowgill, E., 2001, Tectonic evolution of the Altyn Tagh–Western Kunlun fault system, northwestern China [Ph.D. thesis]: Los Angeles, University of California, 311 p.
- Cowgill, E., Yin, A., Wang, X., and Zhang, Q., 2000, Late Cenozoic left-slip movement along the northern Altyn Tagh fault and its possible development as the northern boundary of a transpressional strike-slip duplex: *Geology*, v. 28, p. 255–258.
- CSBS (Chinese State Bureau of Seismology), 1992, *The Aejin active fault belt*: Beijing, Seismology Publishing House, 319 p.
- Delville, N., Arnaud, N., Montel, J.M., Roger, F., Brunel, M., Tapponnier, P., and Sobel, E., 2001, Paleozoic to Cenozoic deformation along Altyn-Tagh fault in the Altun Shan massif area, eastern Qilian Shan, northeast Tibet, China, in Hendrix, M.S., and Davis, G.A., ed., *Paleozoic and Mesozoic tectonic evolution of central and eastern Asia: From continental assembly to intra-continental deformation*: Geological Society of America Memoir 194, p. 269–292.
- Dewey, J.F., and Burke, K., 1973, Tibetan, Variscan and Precambrian basement reactivation: Products of continental collision: *Journal of Geology*, v. 81, p. 683–692.
- Dewey, J.F., Shackelton, R.M., Chang, C., and Sun, Y., 1988, The tectonic evolution of the Tibetan plateau: *Royal Society of London Philosophical Transactions*, v. A327, p. 379–413.
- Dewey, J.F., Cande, S., and Pitman, W.C., 1989, Tectonic evolution of the India-Eurasia collision zone: *Eclogae Geologicae Helveticae*, v. 82, p. 717–734.
- Dickinson, W.R., 1970, Interpreting detrital modes of gray-wacke and arkose: *Journal of Sedimentary Petrology*, v. 40, p. 695–707.
- Dickinson, W.R., 1985, Interpreting provenance relations from detrital modes of sandstones, in Zuffa, G.G., ed., *Provenance of arenites*: Dordrecht, Netherlands, Reidel, p. 333–361.
- Dickinson, W.R., Armin, R.A., Beckvar, N., Goodlin, T.C., Janecek, S.U., Mark, R.A., Norris, R.D., Radel, G., and Wortman, A.A., 1987, Geohistory analysis of rates of sediment accumulation and subsidence for selected California basins, in Ingersoll, R.V., and Ernst, W.G., eds., *Cenozoic basin development of coastal California [Rubey Volume VI]*: Englewood Cliffs, New Jersey, Prentice-Hall, p. 1–23.
- England, P., and Houseman, G., 1986, Finite strain calculations of continental deformation: II. Comparison with the India-Asia collision zone: *Journal of Geophysical Research*, v. 91, p. 3664–3676.
- England, P., and Houseman, G., 1989, Extension during continental convergence, with application to the Tibetan plateau: *Journal of Geophysical Research*, v. 94, p. 17,561–17,579.
- England, P., and Molnar, P., 1998, The field of crustal velocity in Asia calculated from Quaternary rates of slip on faults: *International Geophysical Journal*, v. 130, p. 551–582.
- Fisher, R.A., 1953, Dispersion on a sphere: *Proceedings of the Royal Society of London, Ser. A*, v. 217, p. 245–248.
- Frostick, L.E., and Steel, R.J., 1993, Tectonic signatures in sedimentary basin fills: An overview, in Frostick, L.E., and Steel, R.J., eds., *Tectonic controls and signatures in sedimentary successions*: Blackwell, p. 1–12.
- Galbraith, R.F., and Laslett, G.M., 1993, Statistical models for mixed fission track ages: *Nuclear Tracks and Radiation Measurements*, v. 21, p. 459–470.
- Gallagher, K., Brown, R., and Johnson, C., 1998, Fission track analysis and its applications to geological problems: *Annual Review of Earth and Planetary Sciences*, v. 26, p. 519–527.
- Gansu BGMR, 1989, *Regional geology of Gansu Province*

- (in Chinese with English summary): Beijing, Geological Publishing House, 690 p.
- Gazzi, P., 1966, Le arenarie del flysch sopracretaceo dell'Appennino modenese: Correlazioni con il flysch di Monghidoro: *Mineralogica e Petrographica Acta*, v. 12, p. 69–97.
- George, A., Marshallsea, S.J., Wyrwoll, K.-H., Chen, J., and Lu, Y., 2001, Miocene cooling in the northern Qilian Shan, northeastern margin of the Tibetan plateau, revealed by apatite fission-track and vitrinite-reflectance analysis: *Geology*, v. 29, p. 939–942.
- Gilder, S., Chen, Y., and Sen, S., 2001, Oligo-Miocene magnetostratigraphy and rock magnetism of the Xishuigou section, Subei (Gansu Province, western China) and implications for shallow inclinations in central Asia: *Journal of Geophysical Research*, v. 106, p. 30,505–30,521.
- Gleadow, A.J.W., and Duddy, I.R., 1981, A natural long-term track annealing experiment for apatite: *Nuclear Tracks and Radiation Measurements*, v. 5, p. 169–174.
- Gleadow, A.J.W., Duddy, I.R., Green, P.F., and Lovering, J.F., 1986, Confined fission-track lengths in apatite—A diagnostic tool for thermal history analysis: *Contributions to Mineralogy and Petrology*, v. 94, p. 405–415.
- Graham, S.A., Hendrix, M.S., Wang, L.B., and Carrol, A.R., 1993, Collisional successor basins of western China: Impact of tectonic inheritance on sand composition: *Geological Society of America Bulletin*, v. 105, p. 323–344.
- Green, P.F., Duddy, I.R., Laslett, G.M., Hegarty, K.A., Gleadow, A.J.W., and Lovering, J.F., 1989a, Thermal annealing of fission tracks in apatite: 4. Quantitative modeling techniques and extension to geological time scales: *Chemical Geology*, v. 79, p. 155–182.
- Green, P.F., Duddy, I.R., Gleadow, A.J.W., and Lovering, J.F., 1989b, Apatite fission-track analysis as a paleotemperature indicator for hydrocarbon exploration, in Naeser, N.D., and McCulloch, T.H., eds., *Thermal history of sedimentary basins: Methods and case histories*: New York, Springer-Verlag, p. 181–195.
- Hanson, A.D., 1999, Organic geochemistry and petroleum geology, tectonics and basin analysis of southern Tarim and northern Qaidam Basins, northwest China [Ph.D. thesis]: Stanford, California, Stanford University, 388 p.
- Hao, Y., and Zeng, X., 1984, On the evolution of the west Tarim gulf from Mesozoic to Cenozoic in terms of characteristics of foraminiferal fauna: *Acta Micropalaeontologica Sinica*, v. 1, p. 1–16.
- Harrison, T.M., Copeland, P., Kidd, W.S.F., and Yin, A., 1992, Raising Tibet: *Science*, v. 255, p. 1663–1670.
- Harrison, T.M., Yin, A., and Ryerson, F.J., 1998, Orographic evolution of the Himalaya and Tibetan plateau, in Crowley, T., and Burke, K., eds., *Boundary conditions for climate changes*: New York, Oxford University Press, p. 38–72.
- Heller, P.L., Angevine, C.L., Winslow, N.S., and Paola, C., 1988, Two-phase stratigraphic model of foreland-basin sequences: *Geology*, v. 16, p. 501–504.
- Hildebrand, P.R., Noble, S.R., Searle, M.P., Waters, D.J., and Parrish, R.R., 2001, Old origin for an active mountain range: *Geology and geochronology of the eastern Hindu Kush, Pakistan*: *Geological Society of America Bulletin*, v. 113, p. 625–639.
- Holt, W.E., Chamot-Rooke, N., Le Pichon, X., Haines, A.J., Shen-Tu, B., and Ren, J., 2000, Velocity field in Asia inferred from Quaternary fault slip rates and Global Positioning System observations: *Journal of Geophysical Research*, v. 105, p. 19,185–19,209.
- Huang, J.Q., and Chen, B.W., 1981, On the formation of the Pliocene-Quaternary molasses in the Tethys-Himalayan tectonic domain and its relation with the Indian plate motion: Beijing, Geological Publishing House, *Scientific Papers of Geology for International Exchange*, v. 1, p. 1–14.
- Huang, H.F., Peng, Z.L., Lu, W., and Zheng, J.J., 1993, Paleomagnetic division and comparison of the Tertiary system in Jiuxi and Jiudong Basins: *Acta Geologica Gansu*, v. 2, p. 6–16.
- Huo, G.M., ed., 1990, *Petroleum geology of China*: Oil fields in Qianghai and Xizang, Volume 14: Beijing, Chinese Petroleum Industry Press, 483 p.
- Huo, Y.L., and Tan, S.D., 1995, Exploration case history and petroleum geology in Jiuquan continental basin: Beijing, Petroleum Industry Press, 211 p.
- Ingersoll, R.V., 1990, Actualistic sandstone petrofacies: Discriminating modern and ancient source rocks: *Geology*, v. 18, p. 733–736.
- Ingersoll, R.V., Bullard, T.F., Ford, R.L., Grimm, J.P., Pickle, J.D., and Sares, S.W., 1984, The effect of grain size on detrital modes: A test of the Gazzi-Dickinson point-counting method: *Journal of Sedimentary Petrology*, v. 54, p. 103–116.
- Ingersoll, R.V., Cavazza, W., Graham, S.A., and Indiana University Graduate Field Seminar Participants, 1986, Provenance of impure calcilithites in the Laramide foreland of southwestern Montana: *Journal of Sedimentary Petrology*, v. 57, p. 995–1003.
- Ingersoll, R.V., Kretzmer, A.G., and Valles, P.K., 1993, The effect of sampling scale on actualistic sandstone petrofacies: *Sedimentology*, v. 40, p. 937–953.
- Jia, C., Yao, H., Wi, G., and Li, L., 1991, Plate tectonic evolution and characteristics of major tectonic units of the Tarim Basin, in Tong, X., and Liang, D., eds., *The Tarim Basin*: Urumqi, Xinjiang Scientific Publishing House, p. 207–225 (in Chinese).
- Jiang C., Yang J., Feng B., Zhu Z., Zhao M., Chai Y., Shi X., Wang H., and Hu J., 1992, Opening-closing tectonics of Kunlun Mountains: Beijing, Geologic Publishing House, 224 p. (in Chinese with English abstract).
- Jolivet, L., Tamaki, K., and Fournier, M., 1994, Japan Sea, opening history and mechanism—A synthesis: *Journal of Geophysical Research*, v. 99, p. 22,237–22,259.
- Jordan, T.E., and Gardeweg, M., 1988, Tectonic evolution of the late Cenozoic central Andes (20°–33°), in Ben-Avraham, A., ed., *Cenozoic and Mesozoic evolution of the Pacific margin*: New York, Cambridge University Press, p. 193–207.
- Jordan, T.E., Flemings, P.B., and Beer, J.A., 1988, Dating thrust-fault activity by use of foreland-basin strata, in Kleinspehn, K.L., and Paola, C., eds., *New perspectives in basin analysis*: New York, Springer-Verlag, p. 307–330.
- Kang, Y.Z., ed., 1996, *Petroleum geology and resource assessment in the Tarim Basin, Xinjiang, China*: Beijing, Geological Publishing House, 348 p.
- Kapp, P.A., Yin, A., Manning, C., Murphy, M.A., Harrison, T.M., Ding, L., Deng, X.G., and Wu, C.M., 2000, Blueschist-bearing metamorphic core complexes in the Qiangtang block reveal deep crustal structure of northern Tibet: *Geology*, v. 28, p. 19–22.
- Khadkikar, A.S., Merh, S.S., Malik, J.N., and Chamyal, L.S., 1998, Calcrete in semiarid alluvial systems: Formative pathways and sinks: *Sedimentary Geology*, v. 116, p. 251–260.
- Khadkikar, A.S., Chamyal, L.S., and Ramesh, R., 2000, The character and genesis of calcrete in late Quaternary alluvial deposits, Gujarat, western India, and its bearing on the interpretation of ancient climates: *Palaeogeography, Palaeoclimatology, Palaeoecology*, v. 162, p. 239–261.
- Kirschvink, J.L., 1980, The least-squares line and plane and the analysis of palaeomagnetic data: *Royal Astronomical Society Geophysical Journal*, v. 62, p. 699–718.
- Kong, X., and Bird, P., 1996, Neotectonics of Asia: Thin-shell, finite-element models with faults, in Yin, A., and Harrison, T.M., eds., *The tectonic evolution of Asia*, New York, Cambridge University Press, p. 18–35.
- Kong, X., Yin, A., and Harrison, T.M., 1997, Evaluating the role of preexisting weakness and topographic distributions in the Indo-Asian collision by use of a thin-shell numerical model: *Geology*, v. 25, p. 527–530.
- Lan, X., and Wei, J., 1995, Late Cretaceous–early Tertiary marine bivalve fauna from the western Tarim Basin: Beijing, Chinese Science Publishing House, 212 p.
- Le Pichon, X., Fournier, M., and Jolivet, L., 1992, Kinematics, topography, shortening, and extrusion in the India-Eurasia collision: *Tectonics*, v. 11, p. 1085–1098.
- Li, T., 1996, The process and mechanism of rise and the Qinghai-Tibet plateau: *Tectonophysics*, v. 260, p. 45–53.
- Li, D., Liang, D., Jia, C., Wang, G., Wu, Q., and He, D., 1996, Hydrocarbon accumulations in the Tarim Basin, China: *American Association of Petroleum Geologists Bulletin*, v. 80, p. 1587–1603.
- Li, H., Yang, J., Xu, Z., Wu, C., Zhang, J., Wan, Y., Shi, R., Liou, J.G., and Ireland, T.R., 2000, Age of the Altyn Tagh strike-slip fault: Beijing, China University of Geosciences, 15th Himalaya-Karakoram-Tibet Workshop Abstract Volume, p. 208.
- Liu, Z.Q., 1988, Geologic map of Qinghai-Xizang plateau and its neighboring regions (in Chinese): Beijing, Academia Sinica, Chengdu Institute of Geology and Mineral Resources, Geologic Publisher, scale 1: 500,000.
- Liu, T., Ding, M., and Derbyshire, E., 1996, Gravel deposits on the margins of the Qinghai-Xizang plateau, and their environmental significance: *Palaeogeography, Palaeoclimatology, and Palaeoecology*, v. 120, p. 159–170.
- Marco Polo Software, Inc., 1988–1991, *Basin-Works*: Houston, Texas, Marco Polo Software, 42 p.
- Matte, P., Tapponnier, P., Arnaud, N., Bourjot, L., Avouac, J., Vidal, P., Liu, Q., Pan, Y., and Wang, Y., 1996, Tectonics of western Tibet, between the Tarim and the Indus: *Earth and Planetary Science Letters*, v. 142, p. 311–330.
- McFadden, P.L., and McElhinny, M.W., 1990, Classification of the reversal test in paleomagnetism: *Geophysical Journal International*, v. 103, p. 725–729.
- McFadden, P.L., and Reid, A.B., 1982, Analysis of palaeomagnetic inclination data: *Royal Astronomical Society Geophysical Journal*, v. 69, p. 307–319.
- Meriaux, A.S., Tapponnier, P., Ryerson, F.J., Xu, X., Wang, F., and van der Woerd, J., 2000, Large-scale strain patterns, great earthquake breaks, and late Paleocene slip-rate along the Altyn Tagh fault (China): The 15th Himalaya-Karakoram-Tibet Workshop Abstract Volume, p. 230.
- Métivier, F., Gaudemer, Y., Tapponnier, P., and Meyer, B., 1998, Northeastward growth of the Tibet plateau deduced from balanced reconstruction of two depositional areas: The Qaidam and Hexi Corridor Basins, China: *Tectonics*, v. 17, p. 823–842.
- Meyer, B., Tapponnier, P., Gaudemer, Y., Shunmin, G., and Chen, Z., 1996, Rate of left-lateral movement along the easternmost segment of the Altyn Tagh fault, east of 96°E (China): *Geophysical Journal International*, v. 124, p. 29–44.
- Meyer, B., Tapponnier, P., Bourjot, L., Métiévier, F., Gaudemer, Y., Peltzer, G., Shunmin, G., and Zhitai, C., 1998, Crustal thickening in Gansu-Qinghai, lithospheric mantle subduction, and oblique, strike-slip controlled growth of the Tibet plateau: *Geophysical Journal International*, v. 135, p. 1–47.
- Milnes, A.R., 1992, Calcrete, in Martin, I.P., and Chesworth, W., ed., *Development of Earth surface processes 2: Weathering, soils, and paleosols*: Amsterdam, Elsevier, p. 309–347.
- Molnar, P., and Tapponnier, P., 1975, Cenozoic tectonics of Asia—Effects of a continental collision: *Science*, v. 189, p. 419–426.
- Molnar, P., England, P., and Martinod, J., 1993, Mantle dynamics, uplift of the Tibetan plateau, and the Indian monsoon: *Reviews of Geophysics*, v. 31, p. 357–396.
- Murphy, M.A., Yin, A., Harrison, T.M., Durr, S.B., Chen, Z., Ryerson, F.J., Kidd, W.S.F., Wang, X., and Zhou, X., 1997, Did the Indo-Asian collision create the Tibetan plateau?: *Geology*, v. 25, p. 719–722.
- Norin, E., 1946, Geological explorations in western Tibet, Reports from the scientific expedition to the northwestern provinces of China under the leadership of Dr. Sven Hedin: Thuletryck, Stockholm, 214 p.
- Pan, G.T., 1984, Cenozoic structures and the nature of mountain building in the Altyn Tagh region: Beijing, Chinese Science Press, *Geology of the Qinghai-Xizang (Tibet) plateau*, v. 15, p. 113–120 (in Chinese).
- Pan, Y.S., 1996, Regional geologic evolution and conclusion, in Pan, Y., ed., *Geologic evolution of the Karakoram and Kunlun Mountains*: Beijing, Seismological Press, 263–288.
- Peltzer, G., and Saucier, F., 1996, Present-day kinematics of

- Asia derived from geologic fault rates: *Journal of Geophysical Research*, v. 101, p. 27,943–27,956.
- Peltzer, G., and Tapponnier, P., 1988, Formation and evolution of strike-slip faults, rifts, and basins during the India-Asia collision: An experimental approach: *Journal of Geophysical Research*, v. 93, p. 15,085–15,117.
- Peltzer, G., Tapponnier, P., and Armijo, R., 1989, Magnitude of late Quaternary, left-lateral movement along the north edge of Tibet: *Science*, v. 246, p. 1285–1289.
- Pettijohn, F.J., Potter, P.E., and Siever, R., 1987, *Sand and sandstone* (second edition): New York, Springer-Verlag, 553 p.
- Press, W.H., Teukolsky, S.A., Vetterling, W.T., and Flannery, B.P., 1992, *Numerical recipes* (second edition): Cambridge, Cambridge University Press, 800 p.
- Qinghai BGMR, 1983, Geologic map of the Lenghu Sheet: Beijing, Geological Publishing House, scale 1: 200,000.
- Qinghai BGMR, 1984, Geologic map of the Mangnai Sheet: Beijing, Geological Publishing House, scale 1:200,000.
- Qinghai BGMR, 1989, Geologic history of the Qinghai region: Beijing, Geological Publishing House, 563 p.
- Richards, D.R., Butler, R.F., and Harms, T.A., 1993, Paleomagnetism of the late Paleozoic Slide Mountain terrane, northern and central British Columbia: *Canadian Journal of Earth Sciences*, v. 30, p. 1898–1913.
- Ritts, B.D., and Biffi, L., 2000, Magnitude of post-Jurassic (Bajocian) displacement on the central Altyn Tagh fault system, northwest China: *Geological Society of America Bulletin*, v. 112, p. 61–74.
- Rumelhart, P.E., 1998, Cenozoic basin evolution of southern Tarim, northwestern China: Implications for the uplift history of the Tibetan plateau [Ph.D. thesis]: Los Angeles, University of California, 268 p.
- Rumelhart, P.E., Yin, A., Cowgill, E., Butler, R., Zhang, Q., and Wang, X.F., 1999, Cenozoic vertical-axis rotation of the Altyn Tagh fault system: *Geology*, v. 27, p. 819–822.
- Sadler, P.M., 1981, Sediment accumulation rates and the completeness of stratigraphic sections: *Journal of Geology*, v. 89, p. 569–584.
- Schlunegger, F., Jordan, T.E., and Klaper, E.M., 1997, Controls of erosional denudation in the orogen on foreland basin evolution: The Oligocene central Swiss molasse basin as an example: *Tectonics*, v. 16, p. 823–840.
- Şengür, A.M.C., and Okurogullari, A.H., 1991, The role of accretionary wedges in the growth of continents: Asiatic examples from Argand to plate tectonics: *Eclogae Geologicae Helveticae*, v. 84, p. 535–597.
- Shen, F., Royden, L.H., and Burchfiel, B.C., 2001, Large-scale crustal deformation of the Tibetan plateau: *Journal of Geophysical Research*, v. 106, p. 6793–6816.
- Shen, Z.K., Wang, M., Li, Y., Jackson, D.D., Yin, A., Dong, D., and Fang, P., 2001, Crustal deformation along the Altyn Tagh fault system, western China, from GPS: *Journal of Geophysical Research*, v. 106, p. 30,607–30,621.
- Sobel, E.R., 1995, Basin analysis and apatite fission-track thermochronology of the Jurassic–Paleogene southwest Tarim Basin, northwest China [Ph.D. thesis]: Stanford, California, Stanford University, 308 p.
- Sobel, E.R., 1999, Basin analysis of the Jurassic–lower Cretaceous southwest Tarim Basin, northwest China: *Geological Society of America Bulletin*, v. 111, p. 709–724.
- Sobel, E.R., and Arnaud, N.A., 1999, Possible middle Paleozoic suture in the Altyn Tagh, northwest China: *Tectonics*, v. 18, p. 64–74.
- Sobel, E.R., and Dumitru, T.A., 1997, Thrusting and exhumation around the margins of the western Tarim Basin during the India-Asia collision: *Journal of Geophysical Research*, v. 102, p. 5043–5063.
- Sobel, E.R., Arnaud, N., Jolivet, M., Ritts, B.D., and Brunel, M., 2001, Jurassic to Cenozoic exhumation history of the Altyn Tagh range, northwest China constrained by ⁴⁰Ar/³⁹Ar and apatite fission track thermochronology, in Hendrix, M.S., and Davis, G.A., ed., *Paleozoic and Mesozoic tectonic evolution of central and eastern Asia: From continental assembly to intracontinental deformation*: Geological Society of America Memoir 194, p. 247–268.
- Song, T., and Wang, X., 1993, Structural styles and stratigraphic patterns of syndepositional faults in a contractional setting: Examples from Qaidam Basin, northwestern China: *American Association of Petroleum Geologists Bulletin*, v. 77, p. 102–117.
- Spötl, C., and Wright, V.P., 1992, Groundwater dolocretes from the Upper Triassic of the Paris basin, France: A case study of an arid, continental diagenetic facies: *Sedimentology*, v. 39, p. 1119–1136.
- Tapponnier, P., and Molnar, P., 1977, Active faulting and tectonics in China: *Journal of Geophysical Research*, v. 82, p. 2905–2930.
- Tapponnier, P., Meyer, B., Avouac, J.-P., Peltzer, G., Gaudemer, Y., Guo Shunmin, Xiang Hongfa, Yin Kelun, Chen Zhitai, Cai Shuuhua, and Dai Huangang, 1990, Active thrusting and folding in the Qilian Shan, and decoupling between upper crust and mantle in north-eastern Tibet: *Earth and Planetary Science Letters*, v. 97, p. 382–403.
- Wang, E., 1997, Displacement and timing along the northern strand of the Altyn Tagh fault zone, northern Tibet: *Earth and Planetary Science Letters*, v. 150, p. 55–64.
- Washburn, Z., Arrowsmith, J.R., Forman, S.L., Cowgill, E., Wang, X., Zhang, Y., and Chen, Z., 2001, Late Holocene earthquake history of the central Altyn Tagh fault, China: *Geology*, v. 29, p. 1051–1054.
- Willett, S.D., and Beaumont, C., 1994, Subduction of Asian lithospheric mantle beneath Tibet inferred from models of continental collision: *Nature*, v. 369, p. 642–645.
- Wittlinger, G., Tapponnier, P., Oupinet, G., Jiang, M., Shi, D., Herquel, G., and Masson, F., 1998, Tomographic evidence for localized lithospheric shear along the Altyn Tagh fault: *Science*, v. 282, p. 74–76.
- Worrall, D.M., Kruglyak, V., Kunst, F., and Kuznetsov, V., 1996, Tertiary tectonics of the Sea of Okhotsk, Russia: Far-field effects of the India-Eurasia collision: *Tectonics*, v. 15, p. 813–826.
- Xinjiang BGMR, 1981, Geologic map of the Xorkoli Sheet: Beijing, Geological Publishing House, scale 1: 200,000.
- Xinjiang BGMR, 1993, Regional geology of the Xinjiang Uygur Autonomous Region: Beijing, Geological Publishing House, 561 p.
- Xu, W., He, Y., and Yan, Y., 1989, Tectonic characteristics and hydrocarbons of the Hexi Corridor, in Zhu, X., ed., *Chinese sedimentary basins*: Amsterdam, Elsevier, p. 53–62.
- Yang, F., Tang, W., Wei, J., Fu, Z., and Liang, S., 1994, The northwest region of China: Beijing, Petroleum Industry Press, 253 p.
- Yang, H., Jiang, X., and Lin, S., 1995, Late Cretaceous–early Tertiary ostracod fauna from western Tarim Basin, south Xinjiang, China: Beijing, Chinese Science Publishing House, 173 p.
- Yang, J.S., Xu, Z.Q., Zhang, J.X., Chu, J.Y., Zhang, R.Y., and Liou, J.G., 2001, Tectonic significance of early Paleozoic high-pressure rocks in Altun-Qaidam-Qilian Mountains, northwest China, in Hendrix, M.S., and Davis, G.A., ed., *Paleozoic and Mesozoic tectonic evolution of central and eastern Asia: From continental assembly to intracontinental deformation*: Geological Society of America Memoir 194, p. 151–170.
- Ye, C.H., and Huang, R.J., 1990, The Tertiary stratigraphy of the Tarim Basin, in Zhou, X., and Chen, p. eds., *Stratigraphy of Tarim*: Beijing, Science Press, p. 308–363 (in Chinese).
- Yin, A., 2000, Mode of Cenozoic east-west extension in Tibet suggests a common origin of rifts in Asia during Indo-Asian collision: *Journal of Geophysical Research*, v. 105, p. 21,745–21,759.
- Yin, A., and Harrison, T.M., 2000, Geologic evolution of the Himalayan-Tibetan orogen: *Annual Review of Earth and Planetary Sciences*, v. 28, p. 211–280.
- Yin, A., and Kelty, T.K., 1991, Structural evolution of the Lewis thrust system, southern Glacier National Park: Implications for the regional tectonic development: *Geological Society of America Bulletin*, v. 103, p. 1073–1089.
- Yin, A., and Nie, S.Y., 1996, Phanerozoic palinspastic reconstruction of China and its neighboring regions, in Yin, A., and Harrison, T.M., eds., *Tectonic evolution of Asia*: Cambridge, Cambridge University Press, p. 442–485.
- Yin, A., Nie, S., Craig, P., Harrison, T.M., Ryerson, F.J., Qian, X., and Yang, G., 1998, Late Cenozoic tectonic evolution of the southern Chinese Tian Shan: *Tectonics*, v. 17, p. 1–27.
- Yin, A., Gehrels, G., Chen, X., and Wang, X., 1999, Evidence for 280 km of Cenozoic left slip motion along the eastern segment of the Altyn Tagh fault system, western China [abs.]: *Eos (Transactions, American Geophysical Union)*, v. 80, p. F1018.
- Yin, A., Gehrels, G., Chen, X., Wang, X., and Harrison, T.M., 2000, Normal-slip motion on the northern Altyn Tagh fault [abs.]: *Eos (Transactions, American Geophysical Union)*, v. 81, p. F1092.
- Yue, Y.J., and Liou, J.G., 1999, Two-stage evolution model for the Altyn Tagh fault, China: *Geology*, v. 27, p. 227–230.
- Yue, Y.J., Ritts, B.D., and Graham, S.A., 2001, Initiation and long-term slip history of the Altyn Tagh fault: *International Geology Review*, v. 43, p. 1087–1093.
- Zhai, S.P., and Cai, T.L., 1984, Tertiary System of Gansu, in Wang, Y.M., ed., *Gansu geology*: Gansu, China, People's Publishing House, p. 1–40.
- Zhang, Y.C., 1997, Prototype of analysis of petroliferous basins in China: Nanjing, Nanjing University Press, 434 p.
- Zhang, P.Z., Molnar, P., and Downs, W.R., 2001, Increased sedimentation rates and grain sizes 2–4 Myr ago due to the influence of climate change on erosion rates: *Nature*, v. 410, p. 891–897.
- Zhao, W., and Morgan, W.J., 1987, Injection of Indian crust into Tibetan lower crust: A two-dimensional finite element model study: *Tectonics*, v. 6, p. 489–504.
- Zheng, H.B., Powell, C.M., An, Z.S., Zhou, J., and Dong, G.R., 2000, Pliocene uplift of the northern Tibetan plateau: *Geology*, v. 28, p. 715–718.
- Zhong, S., 1989, Significance of calcareous nannofossil assemblage from Bashibulake Formation (Paleogene) in western Tarim Basin, Xinjiang: *Acta Palaeontologica Sinica*, v. 28, p. 109–116.
- Zhong, S., 1992, Calcareous nannofossils from the Upper Cretaceous and lower Tertiary in the western Tarim Basin, south Xinjiang, China: Beijing, Chinese Science Publishing House, 121 p.
- Zhou, D., and Graham, S.A., 1996, Extrusion of the Altyn Tagh wedge: A kinematic model for the Altyn Tagh fault and palinspastic reconstruction of northern China: *Geology*, v. 24, p. 427–430.

MANUSCRIPT RECEIVED BY THE SOCIETY 11 JUNE 2001
 REVISED MANUSCRIPT RECEIVED 10 APRIL 2002
 MANUSCRIPT ACCEPTED 30 APRIL 2002

Printed in the USA